Chapter 1

Introduction

Magnetic fields play important roles in the dynamics of star formation and, in particular, in the evolution of astrophysical discs. They are thought to drive the acceleration and collimation of jets and outflows frequently observed in star forming systems (Blandford & Payne 1982, Wardle & Konigl 1993, Li 1996, Contopoulos & Saunty 2001, see also review by Königl & Pudritz 2000). They can also effectively regulate the evolution of the 'accretion phase' of protostellar discs (e.g. Adams & Lin 1993), by providing mechanisms that remove angular momentum from the disc material, enabling most of it to be accreted (e.g. Weintraub, Sandell & Duncan 1989; Adams, Emerson & Fuller 1990; Beckwith et al. 1990). In the weakly ionised environment of such discs, the ionisation fraction of the gas is not enough to produce good magnetic coupling over their entire vertical and radial extention. Consequently, the gas close to the midplane is likely to form a magnetically inactive 'dead' zone (Gammie 1996, Wardle 1997), while the fluid near the surface is generally well coupled to the field, as a result of the ionisation contributed by cosmic rays and the x-rays emitted by the protostar. The ability of the magnetic field to effectively couple to the fluid and drive the magnetic processes mentioned above is, therefore, strongly dependent on the conductivity of the gas and its spatial dependency.

Most studies of low conductivity astrophysical systems, including not only protostellar, but also quiescent –and the outer regions of hot-state– dwarf novae discs (Gammie & Menou 1998; Menou 2000; Stone et al. 2000), adopt either the ambipolar diffusion ('plasma drift') or resistive approximations. Ambipolar diffusion is a good approximation in relatively low density regions, where collisions are not very frequent and charged particles can follow the magnetic field and slip with it through

the neutrals. This assumption has been used extensively to model the dynamics of molecular clouds and star formation regions (e.g. Mestel & Spitzer 1956, Shu et al. 1993). Conversely, the resistive ('Ohmic') approximation is valid when the gas density is high enough for charged species to be mainly tied to the neutrals, by collisions; rather than to the magnetic field, by magnetic stresses. This limit has been used to model the evolution of the magnetic field in protostellar discs (e.g. Hayashi 1981).

There is, however, an intermediate density range where the degree of magnetic coupling vary amongst charged species. In this regime, Hall currents are important. It has been shown that this regime dominates over vast regions in weakly ionised discs (Wardle & Ng 1999; Sano & Stone 2002a, 2002b, 2003) and, therefore, should not be ignored when modelling magnetic processes in these systems. Despite this, Hall conductivity has only recently been included in such studies (Wardle 1999, Balbus & Terquem 2001, Sano & Stone 2002a,b; 2003, Salmeron & Wardle 2003 and Desch 2004). Results indicate that when Hall conductivity is taken into account, the extent of the inner magnetically dead zone is reduced and the magnetic field is dynamically important over a wider range of fluid conditions.

In this thesis we explore the magnetic activity of low conductivity astrophysical discs, by modelling one important example of such activity: the linear growth and vertical structure of the magnetorotational instability (MRI; Balbus & Hawley 1991, 1998; Hawley & Balbus 1991). This instability has been identified as the most promising candidate to generate and sustain angular momentum transport radially outwards, so accretion can proceed. Our method includes the effects of the magnetic coupling, the conductivity regime of the fluid and the strength of the magnetic field, which is initially vertical. The conductivity is treated as a tensor and can be a function of location, so the effect of different conductivity regimes being dominant at different heights can be examined. Although the adopted formulation restricts the unstable modes that are modelled, as well as the geometrical configuration of the assumed initial magnetic field (section 2.3); it can, nonetheless, illustrate the far reaching effects of a weak magnetic field in the dynamics of low conductivity discs.

In the next sections we review in more detail the concepts associated with the 'angular momentum transport problem' in protostellar discs and how the MRI offers a simple, yet efficient, mechanism to solve this long-standing problem of accretion theories. We finalise this introduction by summarising our methodology and pre-

senting a brief outline of this work.

1.1 The angular momentum transport problem

The process of star formation, triggered by the collapse of protostellar cores, leads to the development of a central object –a protostar– which will eventually become the new star. A sizable fraction of the collapsing mass forms a disc of material that surrounds this object (e.g. Looney, Mundy & Welch 2003), and which has an average mass of ~ 0.04 times the mass of the central protostar (Natta et al. 2000). The material in the disc is then slowly accreted towards the centre in the 'accretion phase' of the star formation process. Observational evidence for the presence of discs around young stellar objects are compelling. They comprise imaging in the near infrared and optical wavebands (e.g. see review by McCaughrean et. al. 2000) as well as interferometric studies that have resolved the velocity profile and structure in the inner regions of the discs, up to $\sim$ a few tens of AU from the centre (e.g. Wilner & Lay 2000).

These 'protostellar discs' are differentially rotating, with a typical angular momentum profile that increases with radius ($dL/dR > 0$). As a result, accretion can only proceed if angular momentum is carried away to larger radii by a small fraction of disc material, enabling most of the disc to be accreted (e.g. Weintraub, Sandell & Duncan 1989; Adams, Emerson & Fuller 1990; Beckwith et al. 1990). Indeed, the efficiency and evolution of this phase of the star formation process is regulated by the rate at which angular momentum can be transferred outwards (e.g. Adams & Lin 1993).

The mechanism(s) responsible for generating and sustaining this transport are not well understood. Different options have been invoked by many authors over several decades, with various degrees of success. It is known, however, that the molecular viscosity of accretion discs is far too low to explain observed accretion rates (Pringle 1981; see also Frank, King & Raine 2002). Viscous diffusion is able to propagate disturbances in timescales $\sim l^2/\nu$, where l is the distance the disturbance travels as a result of the action of the (kinematic) viscosity ν. Taking $l \sim 10^{10}$ cm and $\nu = 10^5\,\mathrm{cm^2\,s^{-1}}$, this timescale is $\sim 3 \times 10^7$ years (Balbus 2003), far too long to explain the variability observed in some accreting systems. Consequently, some form of 'turbulent' viscosity is thought to be in action.

Most current models of accretion discs adopt, in some form, the α-prescription of Shakura & Sunyaev (1973). In this formulation, the radial-azimuthal component of the stress tensor is assumed to scale with the gas pressure, $w_{r\phi} = \alpha P$. The associated turbulent viscosity is parameterised as $\nu_t = \alpha c_s H$, where c_s is the sound speed and H, the scaleheight of the disc. However useful to support the modelling of accretion discs, this methodology does not offer any explanation for the nature of the accretion torque, whose origin remains unspecified. In fact, using this formulation, all the unknowns and uncertainties of the accretion stress are lumped into the single parameter α.

One of the most natural ways of generating turbulence is via hydrodynamical instabilities. Laboratory shear flows, for example, readily break into turbulence at sufficiently high Reynolds numbers. However, Keplerian discs satisfy the Rayleigh's hydrodynamical stability criterion (angular momentum increases with radius), so the generation and sustaining of hydrodynamic turbulence in these systems is, at best, unproven (e.g. see review by Balbus & Hawley 1998). Convective turbulence has also been considered as an option (Lin & Papaloizou 1980; Lin, Papaloizou & Kley 1993), but further studies appear to indicate that this mechanism transports angular momentum towards the central object (Cabot & Pollack 1992, Ryu & Goodman 1992, Cabot 1996, Stone & Balbus 1996). More generally, the sign of the radial flux generated by convective turbulence may depend on the ratio of the epicyclic frequency to wave frequency of the fluid (Balbus 2003): angular momentum is likely to be transported inwards by long-period, incompressible perturbations; and outwards by high frequency, compressible disturbances. Still, other authors have pointed out that hydrodynamic waves originated by the gravitational field of a companion star could possibly transport angular momentum (Vishniac & Diamond 1989, Rozyczka & Spruit 1993). This mechanism, however, requires an 'external' source to excite, and maintain, such density waves; and can not explain accretion in stars that do not belong to multiple systems.

It is likely that outflows, commonly observed in star forming systems, transport angular momentum away from the central object and thus, play also an important role in regulating accretion processes (e.g. see review by Königl & Pudritz 2000). The apparent correlation between outflow and accretion signatures (e.g. Cabrit et. al. 1990; Cabrit & André 1991; Hartigan, Edwards & Ghandour 1995), lend support to this interpretation. This inflow-outflow mechanism is far from being

well understood, but it is thought that it may be mediated by magnetic stresses (Blandford & Payne 1982, Wardle & Konigl 1993, Li 1996, Contopoulos & Saunty 2001, see also review by Königl & Pudritz 2000).

This takes us to an important point: It is believed that protostellar discs are magnetised. Evidence of this comes from different sources. On the one hand, there is strong evidence for an enhanced magnetic activity in young stellar objects (e.g. see review by Glassgold, Feigelson & Montmerle 2000). As these authors point out, it is likely that the strong magnetic field near the stellar surface, extends out to the circumstellar disc. On the other hand, the remnant magnetisation of primitive meteorites suggest that magnetic fields were important in the solar nebula as well (Levy & Sonnett 1978). This is important for the present topic, as the presence of even a very weak magnetic field, changes dramatically the stability properties of differentially rotating systems (Chandrasekhar 1961). In fact, it is now well accepted that the turbulent viscosity required for accretion is most likely originated by hydromagnetic stresses (Balbus & Hawley 1991, Hawley & Balbus 1991). The study of this 'MHD turbulence' in protostellar dics is further complicated by the low ionisation fraction of the disc, which makes essential to account for the departure from ideal-MHD fluid conditions. These topics are discussed in the next section.

1.2 Magnetorotational instability: mechanism and properties

The notion that magnetic stresses can play an important role in the generation of the 'turbulent' viscosity required for accretion was first flagged by Lynden-Bell (1969). Indeed, the existence of a magnetohydrodynamical (MHD) turbulence in magnetised fluids had been described even earlier by Velikhov (1959) and Chandrasekhar (1960, 1961) through their analysis of the stability properties of Couette flows. These flows are stable when the angular velocity (not the angular momentum, as in the unmagnetised discs) increases with radius (Chandrasekhar 1961). In Keplerian flows, this condition is not satisfied. In fact, as Balbus & Hawley (1991) first pointed out, in the presence of a magnetic field, differentially rotating discs can efficiently generate and sustain angular momentum transport away from the centre through the magnetorotational instability (MRI). This instability acts by converting the free energy

source contributed by the differential rotation of the disc into turbulent perturbations (e.g. Balbus 2003). This possibility has its origin in the additional degrees of freedom introduced in the fluid by magnetic fields, which allow fluid elements to exchange angular momentum non-locally via the distortion of the magnetic field lines that connect them (Christodoulou, Contopoulos & Kazanas 1996). A number of numerical simulations conducted to date have confirmed that the generated MHD-turbulence transports angular momentum outwards (e.g. Brandenburg et. al. 1995; Hawley, Gammie & Balbus 1995, 1996; Matsumoto & Tajima 1995).

The mechanism by which the magnetorotational instability works is surprisingly simple: We begin by imagining an initial, steady state disc configuration in which fluid elements are in orbital motion about the central object while joined by weak magnetic field lines. For simplicity, these lines are assumed to be vertical (fig. 1.1, top panel). In this circumstance, any small disturbance that displaces the elements to different (inner and outer) radii, will also generate magnetic tension, by stretching the magnetic field lines that connect them (see Fig. 1.1, bottom panel). In this configuration, the element in the inner orbit is rotating more rapidly than the other, so the tension in the line transfers some of its angular momentum to the element in the outer orbit. As a result, the inner element drops even closer towards the star, as its new equilibrium position must lie in an orbit associated with less angular momentum (i.e. at a smaller radius). Evidently, the opposite is true for the element displaced away from the star: the tension in the line increases its angular momentum, so it moves outwards. As the elements move away from each other, the tension in the field line increases and the process runs away. Perturbations, once initiated, will amplify. By this mechanism, some fluid elements lose angular momentum, and move inwards; while others gain it, and carry it away from the centre.

Under ideal-MHD conditions, MRI unstable modes exist in astrophysical discs that are differentially rotating, with the angular velocity profile decreasing outwards. Axisymmetric perturbations grow when the magnetic field is 'weak' (subthermal) and a poloidal component is present. These perturbations have a characteristic length scale $\lambda = v_A/\Omega$, where v_A is the alfvén speed and Ω is the angular (Keplerian) frequency of the disc. Their maximum growth rate is $\nu_{max} = q\Omega/2$, where $q \equiv \mathrm{dln}\Omega/\mathrm{dln}r = 1.5$ for a Keplerian rotation profile (Balbus & Hawley 1992a). Importantly, this growth rate is independent of the strength (or direction) of the

magnetic field, as long as the poloidal component exists. Moreover, when the magnetic field is purely toroidal, non-axisymetric modes can still grow, although they are most unstable under the influence of a poloidal field (Balbus & Hawley 1992b).

It is expected that non-ideal MHD effects are important in protostellar discs, outside the innermost regions ($R \lesssim 0.1$ AU), where thermal ionisation is not relevant (Hayashi 1981). The low ionisation fraction of the fluid, especially close to the midplane, can potentially affect the growth and structure of MRI unstable modes. Although even a very small ionisation fraction ($\sim 10^{-13}$) can generate sufficient magnetic coupling (e.g. Balbus 2003), actual values may be even smaller, particularly when chemistry occurring on grain surfaces is considered (Umebayashi & Nakano 1988). As a result, it is unlikely that the magnetic coupling of these discs is significant over their entire vertical and radial extents (Gammie 1996) and non-ideal MHD effects must be taken into account.

Several approximations have been adopted in order to model the MRI in low conductivity accretion discs. In relatively low density regions, the ambipolar diffusion approximation is generally adequate. It is valid when the electron-ion drift is small in relation to the ion-neutral drift, so the magnetic field is frozen into the ionised components of the fluid, with the charged species effectively behaving as a single fluid. The effect of ambipolar diffusion in the linear regime of the MRI has been studied by Blaes & Balbus (1994), who found that discs are locally unstable when the ion-neutral collision frequency is shorter than the epicyclic frequency. The effectiveness of the MRI as an angular momentum transport mechanism must be studied, however, in the non-linear regime. Such studies have been conducted by Brandenburg et. al. (1995), MacLow et. al. (1995) and Hawley & Stone (1998). This last work followed a two-fluid (ion-neutral) evolution, in order to explore the effect of lowering the magnetic coupling in the properties of MRI modes. Significant turbulence and angular momentum transport was found when the collision frequency is of the order of 100Ω. For lower frequencies, the MRI properties appear to be determined primarily by the evolution of the ions alone.

In relatively high density regions, all ionised species are more strongly tied to the neutrals, by collisions, than they are to the magnetic field by magnetic stresses. In these circumstances, the magnetic field lines can not be assumed to be frozen into any fluid component and Ohmic diffusion dominates. Linear studies in this limit have been conducted by Jin (1996), Balbus & Hawley (1998), Papaloizou & Terquem

(1997), Sano & Miyama (1999) and Sano et. al. (2000). When recombination processes on grain surfaces are taken into account, Ohmic dissipation appears to be able to stabilise a minimum-mass solar nebula disc within $\sim$ 20 AU from the central object (Sano et. al. 2000). The extent of this region diminishes as grain size increases and/or particles settle towards the midplane. The non-linear phase of the MRI in this regime has been modelled by Sano et. al. (1998, 2004), Fleming, Stone & Hawley (2000) and Stone & Fleming (2003). In this last study, the ionisation fraction is a function of height. The authors find that the MRI grows in the upper regions of the disc, where the magnetic Reynolds number, $Re_m \equiv c_s^2/\eta\Omega$, exceeds a critical value. Importantly, significant mixing may occur between the inner 'dead zone' and the active layers above, so angular momentum transport may take place in the dead zone, via non-axisymmetric density waves driven by the active layers (Stone & Fleming 2003).

Finally, there is an intermediate density range, in which some charged species (typically electrons) are tied to the magnetic field, while more massive particles (i.e. ions or grains) follow the neutrals. In these conditions, Hall currents are important. Hall diffusion has been shown to be relevant in the low ionisation environment typical of protostellar discs (Wardle & Ng 1999). MRI studies in this limit have been conducted in the linear (Wardle 1999, Balbus & Terquem 2001 and Salmeron & Wardle 2003) and non-linear regimes (Sano & Stone 2002a, b; 2003). In the non-linear phase, the Hall effect was found to enhance the saturation level of the Maxwell stress, although the critical magnetic Reynolds number did not change by much (Sano & Stone 2002b).

1.3 Methodology of this study

In this thesis, we investigate the linear growth and vertical structure of MRI perturbations in low-conductivity accretion discs. Different forms of diffusion of the magnetic field through the neutrals –ambipolar, Hall or resistive– are expected to dominate at different heights, as a result of the density stratification. Our formulation incorporates all three limits by treating the conductivity as a tensor (Cowling 1957, Norman & Heyvaertz 1985, Nakano & Umebayashi 1986, Wardle & Ng 1999). In general, the components of this tensor are the field-parallel conductivity ($\sigma_\parallel$), the Hall conductivity (σ_1) and the Pedersen conductivity (σ_2). They are a function of

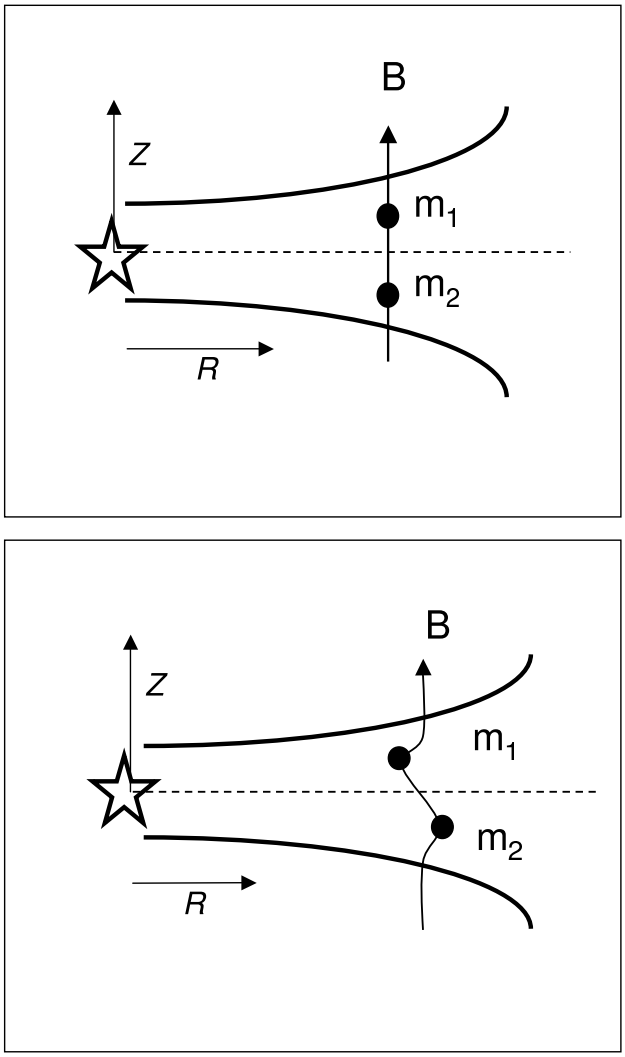

Figure 1.1 The mechanism by which the magnetorotational instability transfer angular momentum outwards is conceptually simple. Initially, two fluid elements are in the same orbit, joined by a (vertical) magnetic field line (see top panel). The tension in the line is negligible. If the elements are displaced to different orbits (bottom panel), the magnetic field line develops tension. This tension lowers the angular momentum of the element in the inner orbit, which is now rotating faster than the other. As a result, it drops even closer to the centre. The opposite is true for the other element: The line tension increases its angular momentum and forces it to move outwards. As the elements separate, the tension in the line increases and the process runs away.

height, as a result of the z dependence of the ionisation fraction. The present study is the first to incorporate all three conductivity components in a stratified disc. This is interesting because the effect of different regimes being locally dominant at different heights can be fully explored.

The methodology also includes the effects of the magnetic coupling and the strength of the magnetic field, which is initially vertical. Perturbations are restricted to have vertical wavevectors only ($k = k_z$). These are the fastest growing modes, from an initially vertical magnetic field, in both the Hall and Ohmic conductivity regimes (Balbus & Hawley 1991, Sano & Miyama 1999). However, as has been recently pointed out by Kunz & Balbus (2004), this is not necessarily true in the ambipolar diffusion limit; where the most unstable modes can have radial wavenumbers as well.

The appropriate governing equations of non-ideal MHD were written about a local Keplerian frame corotating with the disc at the angular frequency $\Omega = \sqrt{GM/r^3}$. These equations were linearised about an initial steady state where the fluid motion is exactly Keplerian. We note that $\sigma_\parallel$, the component of the conductivity tensor parallel to the field does not appear in the final, linearised system of ordinary differential equations (ODE), which signals that under the adopted approximations, the ambipolar diffusion and resistive limits behave identically. The obtained ODE system was integrated vertically from the midplane to the surface of the disc, using appropriate boundary conditions formulated at both ends. This can be treated as a two-point boundary value problem for coupled ODE; which is solved by 'shooting' from the midplane to the surface of the disc, while adjusting the appropriate variables until the solution converges. The adjustment is done via a multidimensional, globally convergent Newton-Raphson method.

1.4 Thesis outline

This investigation is presented as follows:

Firstly, in chapter 2 we conduct a parameter-space analysis of the properties of MRI perturbations in low conductivity discs. For simplicity, we assume that the components of the conductivity tensor are constant with height and examine how the structure and growth of the perturbations are affected when different conductivity regimes dominate over the entire cross-section of the disc. The following

configurations of the conductivity tensor are explored: the ambipolar diffusion (or resistive) limit, both Hall limits, and the cases where both effects are important. The effects of varying the strength of the field and the degree of coupling between ionised and neutral components of the fluid are also studied. We are able to determine the regions of parameter space that support MRI unstable modes in weakly ionised discs, as well as the subset of these for which the Hall effect modifies the structure and growth of unstable perturbations. We find that for weak coupling, perturbations obtained with the full conductivity tensor grow faster and act over a more extended cross-section of the disc than those obtained using the ambipolar diffusion approximation. Similarly, we explore the impact of the alignment of the magnetic field and the angular velocity vectors of the disc when Hall conductivity is important. Finally, in this chapter we derive an approximate criterion for when Hall diffusion drives the growth of the magnetorotational instability. This criterion is satisfied for a broad range of fluid conditions in protostellar discs.

In a real disc, the conductivities vary with height as a result of the z-dependency of the charged particle abundances and fluid density. In these conditions, different conductivity regimes are expected to dominate at different heights (Wardle 2003). Therefore, in chapter 3 we expand this study to include height-dependent conductivity components, calculated using a realistic ionisation profile. Dust grains are assumed to have settled towards the midplane of the disc, so electrons and ions are the sole charge carriers. We obtain solutions at representative radial locations from the central object ($R = 1$, 5 and 10 AU), for different choices of the initial magnetic field strength and configurations of the conductivity tensor. As the ionisation fraction of the disc is expected to be heavily dependent on whether cosmic rays are able to penetrate it, or are excluded by the winds emitted by the magnetically active protostar, we compare results obtained in both scenarios. In all cases, the ionisation rates contributed by x-rays and radioactive materials are included. Solutions are computed for the minimum-mass solar nebula model (Hayashi 1981), as well as for a more massive disc. Results indicate that the magnetic field is dynamically important for a large range of fluid conditions and field strengths in protostellar discs. One important instance of such activity is the generation of MRI unstable modes, which exist at 1 AU (minimum solar nebula disc incorporating cosmic ray ionisation) for $B \lesssim 8$ G. Moreover, when 200 mG $\lesssim B \lesssim 5$ G, these modes grow at about the ideal-MHD rate (0.75Ω). Hall diffusion largely determines the properties

of the perturbations for all studied radii.

In the solutions presented in chapters 2 and 3, dust grains has not been taken into account. This is a valid approximation in relatively late evolutionary stages of accretion, after dust grains have settled enough towards the midplane that they do not appreciably affect the dynamics of the gas at higher vertical locations. However, this settling is expected to be affected by MHD turbulence, which could potentially prevent dust particles from settling below a certain height (Dullemond & Dominik 2004 and references therein). On the other hand, dust grains lower the ionisation fraction of the gas, via recombination processes that occur on their surfaces, so their presence is likely to modify the efficiency of MHD turbulence itself. As a result, it is expected that the properties of MRI unstable modes will be changed by the presence of dust particles. As an illustration of this effect, in chapter 4 we compare the solutions presented in the previous chapter for $R = 10$ AU (and no grains), with results obtained at the same radius and with the same magnetic field strengths, but assuming 0.1μm dust grains are present and fully mixed with the gas. We found that unstable modes are supported in this case for $B \lesssim 10$ mG, down from $B \lesssim 250$ mG when grains were settled. Similarly, the central dead zone (which was practically nonexistent before, given the relatively high magnetic coupling at this radius) extends in this scenario to $z/H \lesssim 3$. Assuming that the maximum field strength that supports MRI perturbations is the equipartition field at this height (Wardle in prep.), we estimate that unstable modes exist at 1 AU for $B \lesssim 400$ mG.

The overall conclusions of this investigation are summarised in chapter 5. Broader implications for the study of astrophysical discs and directions for future work are discussed.

Finally, we acknowledge that chapters 2 and 3 contain some repetition, especially in the introduction and methodology sections. This has been unavoidable, as they are complete papers either published (chapter 2) or submitted for publication (chapter 3).

Chapter 2

The instability in parameter space

2.1 Introduction

The collapse of protostellar cores lead to the development of a central mass or protostar, surrounded by a disc of material, which is accreted towards the center. During this process angular momentum is transferred to a small percentage of disc material at large radii, enabling the collapse of most of the disc towards the central star (e.g. Weintraub, Sandell & Duncan 1989; Adams, Emerson & Fuller 1990; Beckwith et al. 1990). The evolution of this 'disc accretion' phase is dependent upon the rate of angular momentum transport in the disc (e.g. Adams & Lin 1993).

A variety of mechanisms have been invoked to explain this transport. As the molecular viscosity of accretion discs is too low to explain observed accretion rates (Pringle 1981), some form of turbulent viscosity must be present. The origin and characteristics of this turbulence remains an important problem in star formation theories. Convective turbulence has been considered as an option (Lin & Papaloizou 1980), but further studies suggest that this mechanism may transport angular momentum towards the central star instead of away from it (Cabot & Pollack 1992; Ryu & Goodman 1992; Stone & Balbus 1996). The gravitational field of a companion star may trigger hydrodynamic waves which can transport angular momentum (Vishniac & Diamond 1989; Rozyczka & Spruit 1993), but as a significant fraction of stars do not belong to binary systems, this mechanism is not general enough to explain accretion processes in all stars.

Balbus and Hawley have pointed out that the nature of this anomalous viscosity

can be hydromagnetic (Balbus & Hawley 1991; Hawley & Balbus 1991; Stone et al. 1996). This 'magnetorotational' instability (MRI) had been described initially by Velikov (1959) and Chandrasekhar (1961) through their analysis of magnetised Couette flows. It drives turbulent motions which transport angular momentum radially outwards, as fluid elements exchange angular momentum non-locally by means of the distortion of the magnetic field lines that connect them.

Under ideal MHD conditions, MRI perturbations grow in discs that are differentially rotating, with the angular velocity increasing outwards. Axisymmetric modes need a magnetic field with a weak, poloidal component. In this context, 'weak' means that the magnetic energy density of the field is less than the thermal energy density. These perturbations have a characteristic length scale $\lambda \sim v_A/\Omega$, where v_A is the Alfvén speed and Ω is the Keplerian angular frequency in the disc, and a maximum growth rate $\sim q\Omega/2$, with $q \equiv 1.5$ for Keplerian discs (Balbus & Hawley 1992a). This growth rate does not depend on the strength or direction of the magnetic field as long as a poloidal component is present. Non-axisymmetric perturbations are most unstable under the influence of a poloidal field, but also grow at a reduced rate if the field is purely toroidal (Balbus & Hawley 1992b). These perturbations are of interest for the analysis of field amplification mechanisms, as dynamo amplification can not occur through axisymmetric perturbations (Moffatt 1978). With no strong dissipation processes, no other conditions are required. Because of its robustness and the general conditions under which it develops, the magnetorotational instability is a promising source of turbulent viscosity in accretion discs.

Ideal MHD conditions are a good approximation to model astrophysical systems where the ionisation fraction of the gas is high enough to ensure neutral and ionised components of the fluid are well coupled. Active dwarf novae (except possibly in the outer regions) and black hole accretion discs are examples of such systems. However, in dense, cool environments such as those of protostellar discs, it is doubtful that magnetic coupling is significant over the entire radial and vertical dimensions of the discs (Gammie 1996; Wardle 1997). Similar conditions are thought to apply in quiescent and the outer regions of hot-state dwarf novae discs (Gammie & Menou 1998; Menou 2000; Stone et al. 2000). In these cases, low conductivity significantly affects the growth and structure of MRI perturbations. Different approximations have been adopted to account for the departure from ideal MHD in low conductivity astrophysical discs (see section 2.2.1).

Most models of the MRI in low conductivity discs have used the ambipolar diffusion (Blaes & Balbus 1994; MacLow et al. 1995; Hawley & Stone 1998) or resistive (Jin 1996; Balbus & Hawley 1998; Sano, Inutsuka & Miyama 1998) limits. Recently, it has been recognised the importance of the Hall conductivity terms in addition to resistivity for the analysis of low conductivity discs (Wardle 1999, hereafter W99, Balbus & Terquem 2001 and Sano & Stone 2002a,b; 2003).

The huge variation of fluid variables over the vertical and radial extension of astrophysical discs is a further complication. Vertical stratification is particularly relevant, as these objects are generally thin and changes in the plane of the disc are much more gradual than those in the direction perpendicular to it. Previous models of the MRI have not included density stratification and Hall conductivity simultaneously. It is expected that solutions will be strongly modified when both factors are present. This motivates the present study.

This chapter examines the structure and linear growth of the magnetorotational instability in vertically stratified, non self-gravitating accretion discs. We assume the disc is isothermal and geometrically thin, so variations in the fluid variables in the radial direction can be ignored. The initial magnetic field is vertical and the analysis is restricted to perturbations with wavevector perpendicular to the plane of the disc ($k = k_z$). These are the most unstable perturbations with the adopted field geometry, as magnetic pressure strongly supresses displacements with $k_r \neq 0$ (Balbus & Hawley 1991, Sano & Miyama 1999). The conductivity of the gas is treated as a tensor and assumed constant with height in this initial study, although the formulation is also valid for a z-dependent conductivity. This makes the present method a powerful tool for the analysis of more realistic discs (see section 2.6 - Discussion).

Section 2.2 presents the governing equations for a weakly ionised, magnetised disc in near-Keplerian motion around the central star and details the adopted disc model. Section 2.3 summarises the linearisation of the equations and presents the final linear system in dimensionless form. It also describes the three parameters that control the dynamics of the fluid. Section 2.4 discusses the boundary conditions used to integrate the equations from the midplane to the surface of the disc and the integration method. Section 2.5 presents the test cases used to characterise the conductivity regimes relevant for this work and compares our results with a previous local analysis. It also details key findings on the dependency of the structure and

growth rate of the perturbations with the conductivity regime, the strength of the magnetic field and its coupling with the neutral gas. These results are discussed in section 2.6. By way of example, this section also calculates the structure and growth rate of the MRI under fluid conditions where different conductivity regimes are dominant at different heights above the midplane. This reflects (qualitatively) the conditions expected to be found in real discs. Finally, the methodology and key findings in this chapter are summarised in section 2.7.

2.2 Formulation

2.2.1 Governing Equations

The equations of non-ideal MHD are written about a local Keplerian frame corotating with the disc at the angular frequency Ω associated with the particular radius of interest. Consequently, the velocity of the fluid can be expressed as a departure from exact Keplerian motion $\mathbf{v} = \mathbf{V} - \mathbf{v}_K$, where $\mathbf{V}$ is the velocity in the standard laboratory coordinate system (r, ϕ, z) anchored at the central mass M, and $\mathbf{v}_K = \sqrt{GM/r}\hat{\phi}$ is the Keplerian velocity at the radius r. Similarly, if $\partial/\partial t$ is the time derivative in the local Keplerian frame, then the time derivative in the laboratory frame can be expressed as $\partial/\partial t + \Omega\partial/\partial\phi$. We also assume that the fluid is weakly ionised, meaning that the abundances of charged species are so low that their inertia and thermal pressure, as well as the effect of ionisation and recombination processes in the neutral gas, are negligible. These assumptions effectively restrict the range of frequencies that can be studied with this formulation to be smaller than the collision frequency of any of the charged species with the neutrals. Accordingly, separate equations of motion for the charged species are not required and their effect on the neutrals is contained in a conductivity tensor (see section 2.2.2).

The governing equations are the continuity equation,

$$\frac{\partial \rho}{\partial t} + \nabla \cdot (\rho \mathbf{v}) = 0\,, \tag{2.1}$$

the equation of motion,

$$\frac{\partial \mathbf{v}}{\partial t} + (\mathbf{v}\cdot\nabla)\mathbf{v} - 2\Omega v_\phi \hat{\mathbf{r}} + \tfrac{1}{2}\Omega v_r \hat{\phi} - \frac{v_K^2}{r}\hat{\mathbf{r}} + \frac{c_s^2}{\rho}\nabla\rho + \nabla\Phi - \frac{\mathbf{J}\times\mathbf{B}}{c\rho} = 0\,, \tag{2.2}$$

and the induction equation,

$$\frac{\partial \mathbf{B}}{\partial t} = \nabla\times(\mathbf{v}\times\mathbf{B}) - c\nabla\times\mathbf{E}' - \tfrac{3}{2}\Omega\mathbf{B}_r\hat{\phi}\,. \tag{2.3}$$

In the equation of motion (2.2), Φ is the gravitational potential due to the central mass, given by

$$\Phi = -\frac{GM}{(r^2+z^2)^{\frac{1}{2}}}\,, \tag{2.4}$$

and v_K^2/r is the centripetal term generated by exact Keplerian motion. At the disc midplane this term balances the radial component of the gravitational potential. The terms $2\Omega v_\phi\hat{\mathbf{r}}$ and $\frac{1}{2}\Omega v_r\hat{\phi}$ are the coriolis terms associated with the use of a local Keplerian frame, $c_s = \sqrt{P/\rho}$ is the isothermal sound speed, $\Omega = v_K/r$ is the Keplerian frequency and c is the speed of light. Other symbols have their usual meanings.

In the induction equation (2.3), the term $c\nabla\times\mathbf{E}'$contains the effects of non-ideal MHD. $\mathbf{E}'$ is the electric field in the frame comoving with the neutrals and the term $\frac{3}{2}\Omega\mathbf{B}_r\hat{\phi}$ accounts for the generation of toroidal field from the radial component due to the differential rotation of the disc.

Additionally, the magnetic field must satisfy the constraint:

$$\nabla\cdot\mathbf{B} = 0\,, \tag{2.5}$$

and the current density must satisfy Ampere's law,

$$\mathbf{J} = \frac{c}{4\pi}\nabla\times\mathbf{B} \tag{2.6}$$

and Ohm's law,

$$\mathbf{J} = \sigma\cdot\mathbf{E}'\,. \tag{2.7}$$

Note that the conductivity, which depends on the abundance and drifts of the charged species through the neutral gas is treated as a tensor σ, as detailed in the following section. This formulation is compared to the drift velocity approach in section 2.2.3.

2.2.2 The conductivity tensor σ

The electric conductivity is a tensor whenever the gyrofrequency of the charged carriers is larger than the frequency of momentum exchange by collisions with the neutrals, or $|\beta| \gg 1$ (Cowling 1957, Norman & Hayvaerts 1985, Nakano & Umebayashi 1986). On the contrary, when collisions with the neutrals are dominant the conductivity is a scalar, the ordinary ohmic resistivity. To obtain expressions for the components of this tensor, we begin by writing down the equations of motion of the ionised species. As inertia and thermal pressure are neglected, the motion of the charged particles is given by the balance of the Lorentz force and the drag force from collisions with the neutrals,

$$Z_j e \left(\mathbf{E}' + \frac{\mathbf{v}_j}{c} \times \mathbf{B} \right) - \gamma_j m_j \mathbf{v}_j = 0 \,, \tag{2.8}$$

where each charged species j is characterised by its number density n_j, particle mass m_j, charge $Z_j e$ and drift velocity $\mathbf{v}_j$. In the above equation,

$$\gamma_j = \frac{< \sigma v >_j}{m_j + m} \,, \tag{2.9}$$

where m is the mean mass of the neutral particles and $< \sigma v >_j$ is the rate coefficient of momentum exchange by collisions with the neutrals. We will also make use of the Hall parameter,

$$\beta_j = \frac{Z_j e B}{m_j c} \frac{1}{\gamma_j \rho} \,, \tag{2.10}$$

given by the ratio of the gyrofrequency and the collision frequency of charged species j with the neutrals. It represents the relative importance of the Lorentz and drag terms in equation (2.8).

Following the treatment of Wardle & Ng (1999) and W99 we use the following expression for Ohm's law,

$$\mathbf{J} = \sigma \cdot \mathbf{E}' = \sigma_\parallel \mathbf{E}'_\parallel + \sigma_1 \hat{\mathbf{B}} \times \mathbf{E}'_\perp + \sigma_2 \mathbf{E}'_\perp \,, \tag{2.11}$$

obtained by inverting (2.8) to express $\mathbf{v}_j$ as a function of $\mathbf{E}'$ and $\mathbf{B}$ and then using $\mathbf{J} = e \sum_j n_j Z_j \mathbf{v}_j$ together with the charge neutrality assumption $\sum_j n_j Z_j = 0$. In equation (2.11), $\mathbf{E}'_\parallel$ and $\mathbf{E}'_\perp$ are the components of the electric field $\mathbf{E}'$, paral-

lel and perpendicular to the magnetic field, respectively. The components of the conductivity tensor σ are the conductivity parallel to the magnetic field,

$$\sigma_{\parallel} = \frac{ec}{B} \sum_j n_j Z_j \beta_j \,, \tag{2.12}$$

the Hall conductivity,

$$\sigma_1 = \frac{ec}{B} \sum_j \frac{n_j Z_j}{1+\beta_j^2} \,, \tag{2.13}$$

and the Pedersen conductivity,

$$\sigma_2 = \frac{ec}{B} \sum_j \frac{n_j Z_j \beta_j}{1+\beta_j^2} \,. \tag{2.14}$$

The relative values of the components of the conductivity tensor differentiate three conductivity regimes:

1. The *ambipolar diffusion* regime occurs when $\sigma_{\parallel} \gg \sigma_2 \gg |\sigma_1|$, or $|\beta| \gg 1$ for most charged species. This implies that most charged particles are strongly tied to the magnetic field by electromagnetic stresses. This regime is dominant at relatively low densities, where the magnetic field is frozen into the ionised component of the fluid and drifts with it through the neutrals. The linear behaviour of the MRI in this regime has been analysed by Blaes & Balbus (1994) and the non-linear growth by MacLow et al. (1995) and Hawley & Stone (1998).

2. The *resistive (Ohmic)* regime is obtained when most charged species are linked to the neutrals via collisions. This occurs when $\sigma_{\parallel} \approx \sigma_2 \gg |\sigma_1|$, implying $|\beta| \ll 1$. This regime is predominant closest to the midplane, where the high density makes the collision frequency of the charged particles with the neutrals high enough to prevent the former from drifting. This case has been studied under a linear approximation by Jin (1996), Balbus & Hawley (1998), Papaloizou & Terquem (1997), Sano & Miyama (1999) and Sano et. al. (2000). The non-linear regime has been studied by Sano et al. (1998); Fleming, Stone & Hawley (2000) and Stone & Fleming, (2003). This last work includes a z-dependent resistivity.

3. Finally, the *Hall* regime occurs when charged particles of one sign are tied to the magnetic field while those of the other sign follow the neutrals. In this case $|\sigma_1| \sim \sigma_2 < \sigma_\parallel$ and $|\beta| \approx 1$. It is important at intermediate densities, between the ones associated with the ambipolar and Ohmic difussion regimes. Recent studies have explored the MRI with Hall effects in the linear (W99, Balbus & Terquem 2001) and non-linear regimes (Sano & Stone 2002a,b; 2003).

2.2.3 Comparison with the multifluid approach

Another commonly used form of the induction equation is obtained by assuming that ions and electrons are the main charge carriers and drift through the neutrals (e.g Balbus & Terquem 2001, Sano & Stone 2002). Using this approach, the induction equation is

$$\begin{aligned}\frac{\partial \mathbf{B}}{\partial t} &= \nabla\times(\mathbf{v}_e\times\mathbf{B}) \\ &= \nabla\times\left[\mathbf{v}\times\mathbf{B} - \frac{4\pi\eta\mathbf{J}}{c} - \frac{\mathbf{J}\times\mathbf{B}}{en_e} + \frac{(\mathbf{J}\times\mathbf{B})\times\mathbf{B}}{c\gamma_i\rho\rho_i}\right]\end{aligned} \tag{2.15}$$

where $\mathbf{v}_e$ is the electron drift speed, $\eta = c^2/4\pi\sigma$ is the resistivity and subscripts e and i refer to electrons and ions, respectively. The four terms in the right hand side of equation (2.15) are, from left to right, the inductive, resistive, Hall and ambipolar diffusion terms. We now express equation (2.3) in terms of $\mathbf{J}$, $\mathbf{B}$ and the components of the conductivity tensor in order to show that, in the appropriate limit, it corresponds to equation (2.15), as expected. We begin by inverting equation (2.11) to find an expression for $\mathbf{E}'$,

$$\mathbf{E}' = \frac{\mathbf{J}}{\sigma_\parallel} + \frac{\sigma_1}{\sigma_\perp^2}\frac{\mathbf{J}\times\mathbf{B}}{B} - \left(\frac{\sigma_2}{\sigma_\perp^2} - \frac{1}{\sigma_\parallel}\right)\frac{(\mathbf{J}\times\mathbf{B})\times\mathbf{B}}{B^2} \tag{2.16}$$

where $\sigma_\perp = \sqrt{\sigma_1^2 + \sigma_2^2}$ is the total conductivity perpendicular to the magnetic field. Assuming that the only charged species are ions and electrons with Hall parameters β_i and β_e (< 0), respectively, and that charge neutrality is satisfied ($n_i = n_e$), we obtain the following expressions for the components of the conductivity tensor:

$$\sigma_\parallel = \frac{cen_e}{B}(\beta_i - \beta_e)\,, \tag{2.17}$$

$$\sigma_1 = \frac{cen_e}{B}\frac{(\beta_i+\beta_e)(\beta_e-\beta_i)}{(1+\beta_e^2)(1+\beta_i^2)}\,, \text{ and} \tag{2.18}$$

$$\sigma_2 = \frac{cen_e}{B}\frac{(1-\beta_i\beta_e)(\beta_i-\beta_e)}{(1+\beta_e^2)(1+\beta_i^2)}\,. \tag{2.19}$$

From (2.18) and (2.19), we find:

$$\sigma_\perp = \frac{cen_e}{B}\frac{(\beta_i-\beta_e)}{[(1+\beta_e^2)(1+\beta_i^2)]^{1/2}}\,. \tag{2.20}$$

Substituting these expressions into (2.16) gives

$$\mathbf{E}' = \frac{\beta_e}{\beta_i-\beta_e}\frac{\mathbf{J}}{\sigma} + \frac{\beta_e+\beta_i}{\beta_e-\beta_i}\frac{\mathbf{J}\times\mathbf{B}}{cen_e} - \frac{\beta_e}{\beta_e-\beta_i}\frac{(\mathbf{J}\times\mathbf{B})\times\mathbf{B}}{c^2\gamma_i\rho\rho_i} \tag{2.21}$$

where σ is the electrical conductivity due to electrons. Finally, simplifying (2.21) by using $|\beta_e| \gg \beta_i$ (as is the case) and substituting the resulting $\mathbf{E}'$ in equation (2.3) (without the coriolis term), yields the standard result, shown in (2.15).

Each of the last three terms in the right hand side of equation (2.15) dominate when the fluid is in a particular conductivity regime (section 2.2.2). These limits can also be recovered with the appropriate assumptions, through equations (2.16) and (2.21). To get the resistive regime, for example, we substitute $\sigma_1 = 0$ and $\sigma_\parallel = \sigma_2$ into equation (2.16). In this limit the conductivity is a scalar (the resistive approximation), so $\mathbf{E}' = \mathbf{J}/\sigma$ and the induction equation reduces to the familiar form,

$$\frac{\partial\mathbf{B}}{\partial t} = \nabla\times\left[\mathbf{v}\times\mathbf{B} - \frac{c^2}{4\pi\sigma}\nabla\times\mathbf{B}\right]\,. \tag{2.22}$$

On the other hand, to model the Hall limit, we regard the charged species to be either 'ions', which are strongly tied to the neutrals through collisions ($\beta_i \ll 1$), or 'electrons', for which the only important forces are electromagnetic stresses ($|\beta_e| \gg 1$) (see also discussion in W99). In this limit the Hall conductivity is

$$|\sigma_1| = \frac{cen_e}{B} \tag{2.23}$$

while the Pedersen conductivity is

$$\sigma_2 = |\sigma_1|\left(\beta_i - \frac{1}{\beta_e}\right) \ll \sigma_1\,. \tag{2.24}$$

As the ions are effectively locked with the neutrals, the current density will be given by the drift of the electrons through the neutral gas. Collisions are unimportant in their equation of motion, so they drift perpendicular to the plane of the electric and magnetic fields, in order to annul the Lorentz force acting upon them. In this limit $[(\mathbf{J}\times\mathbf{B})\times\mathbf{B}]/B^2 = -\mathbf{J}$ and

$$\mathbf{E}' = \frac{\mathbf{J}\times\mathbf{B}}{cen_e}\,, \tag{2.25}$$

consistent with the Hall term in equation (2.15).

Finally, the ambipolar diffusion approximation is recovered by assuming $\sigma_\parallel \gg \sigma_2$, $\sigma_1 = 0$ and $|\beta_e| \gg \beta_i \gg 1$. In this limit, the Pedersen conductivity is given by

$$\sigma_2 = \frac{ce}{B}\frac{n_i}{\beta_i}\,, \text{ and} \tag{2.26}$$

$$\mathbf{E}' = -\frac{(\mathbf{J}\times\mathbf{B})\times\mathbf{B}}{c^2\gamma_i\rho\rho_i}\,, \tag{2.27}$$

which originates the ambipolar diffusion term of (2.15).

Although the multifluid drift and conductivity tensor formulations are ultimately equivalent, which one is more convenient depends on the problem at hand. In particular, the presence of dust grains tends to make the treatment of different species especially complex. In protostellar discs, dust grains can be the more abundant charged species over extended regions. For example, assuming $0.1\,\mu$m grains, negatively charged grains dominate whenever $n_H \gtrsim 10^{11}$ cm^{-3}, while positive charged grains are the most abundant ions for $n_H \gtrsim 10^{14}$ cm^{-3} (Wardle & Ng 1999). Having separate equations of motion for different charged species would generally involve dividing the grain size distribution of interest into an appropriate number of discrete intervals and explicitly treating each one. Unless the number of such intervals is small it is easy to see that this method can become very cumbersome. In these circumstances, incorporating the contribution of each charged species into a conductivity tensor can be a valuable approach.

2.2.4 Disc Model

Our model incorporates the vertical structure of the disc, but neglects fluid variations in the radial direction. This is appropriate as astrophysical accretion discs are

generally thin and changes in the radial direction occur in a much bigger length scale than those in the vertical direction. Including the vertical structure means that perturbations of spatial dimensions comparable to the scale height of the disc, which are associated with a strong magnetic field ($v_A \sim c_s$), or low conductivity, can be explored.

The balance between the vertical component of the central gravitational force and the pressure gradient within the disc determines its equilibrium structure. The vertical density distribution of a (vertically isothermal) disc in hydrostatic equilibrium is given by

$$\frac{\rho(r,z)}{\rho_o(r)} = \exp\left(-\frac{z^2}{2H^2(r)}\right) . \tag{2.28}$$

In the above equation, $\rho_o(r)$ is the gas density at the midplane and $H(r) = c_s/\Omega$ is the scaleheight of the disc.

A self-consistent treatment of this problem, would involve adopting a particular dependency of ρ_o and H with r using a suitable model, such as the minimum solar nebula (Hayashi, Nakazawa & Nakagawa 1985) and calculating $\rho(r,z)$ by means of (2.28). This density, together with the adopted strength of the magnetic field $\mathbf{B}$ and the values of the conductivity tensor σ as a function of height would be used to evaluate the parameters that govern the fluid evolution (see section 2.3.3) and solve the fluid equations.

The realistic evaluation of the conductivity tensor is a complex undertaking, as it depends critically on the abundances of charged species (ions, electrons and charged dust grains) which, in turn, are a function of the ionisation balance in the disc. This balance is given by the equilibrium between ionisation processes by cosmic rays, radioactive elements and X-rays from the central star (e.g. Hayashi 1981; Glassgold, Najita & Igea 1997, Igea & Glassgold 1999; Fromang, Terquem & Balbus 2002) and recombinations taking place both in the gas phase and in grain surfaces (e.g. Nishi, Nakano & Umebayashi 1991). In low conductivity discs, the level of ionisation is insufficient to produce good coupling between the magnetic field and the neutral component of the fluid over their entire vertical structure. In protostellar discs, for example, it is expected that in the region outside ~ 0.1 AU from the central star, the coupling will be significant only in the surface layers, where X-rays and cosmic rays can penetrate and ionise the gas (Gammie 1996; Wardle 1997). In

these environments, the z-dependent attenuation of the ionisation rate typical of interstellar space $10^{-17}\mathrm{H}^{-1}$ s^{-1} has to be taken into account.

On the other hand, the contribution of dust grains to recombination processes is particularly complex, because they generally have a distribution of sizes and corresponding collision cross sections (Mathis, Rumpl & Nordsieck 1977; Umebayashi & Nakano 1990). Moreover, the dynamics of grain particles depends on the activity of the disc. In quiescent environments, they tend to settle towards the midplane and begin to agglomerate into bigger structures that could eventually become planets (e.g. Weidenschilling & Cuzzi 1993). This removes grains from regions at relatively high z and causes the ionisation level to increase by reducing recombination processes taking place in their surfaces. Simulations of the evolution of dust grain distributions in dense cores show that they grow icy mantles and coagulate efficiently (Ossenkopf 1993). By this process, the smallest particles grow quickly while the upper grain size limit is only slightly changed (Ossenkopf 1993). As a result, the surface area of dust grains can be significantly modified by grain evolution, which ultimately affects the ionisation balance in the disc.

In the present work, a simpler treatment has been adopted. In order to study the MRI under different conductivity regimes, the values of the components of the conductivity tensor have been selected so that they satisfy the conditions outlined in section 2.2.2 for each regime. For simplicity, these values are assumed to be constant, although the formulation allows them to be a function of height. We found that the parameters that control the evolution of the fluid are the ratio of the components of the conductivity tensor perpendicular to the magnetic field (σ_1/σ_2), the strength of the magnetic field and its degree of coupling with the neutral component of the fluid (see section 2.3.3). The midplane values of these parameters have been selected in order to simulate the fluid conditions we were interested in modelling. This approach will be discussed in section 2.5.1 where the chosen test cases are detailed.

With this approach we are able to study the dependency of the growth rate and structure (characterised by the height of maximum amplitude and the wavenumber of unstable modes) of the instability with the parameters of the fluid in a stratified disc. This is relevant, as the region where linear perturbations peak is also expected to be the region where non-linear perturbations grow fastest, until turbulence finally sets in and causes all wavenumbers to interact so that, eventually, the longest wavelengths carry the greatest angular momentum transport (e.g. Hawley & Balbus

1995).

2.3 Linearisation

We linearised the system of equations (2.1) - (2.3), (2.6) and (2.11) about an initial steady state where $\mathbf{J} = \mathbf{v} = \mathbf{E}' = 0$ and $\mathbf{B} = B\hat{z}$. In the initial state both $\mathbf{E}'$ and $\mathbf{J}$ vanish, so the changes in the conductivity tensor due to the perturbations do not appear in the linearised equations. As a result, it is not necessary to explore how the perturbations affect the conductivity and only the values in the initial steady state are required.

2.3.1 Linearised Equations

We assume the wavevector of the perturbations is perpendicular to the plane of the disc ($k = k_z$). Perturbations with a vertical wavenumber, initiated from a vertically aligned equilibrium magnetic field, exhibit the fastest growth rate for a given set of parameters because magnetic pressure strongly suppresses displacements with $k_r \neq 0$ (Balbus & Hawley 1991; Sano & Miyama 1999). Taking perturbations of the form $\mathbf{q} = \mathbf{q}_0 + \delta\mathbf{q}(z)e^{i\omega t}$ about the initial state, linearising and neglecting terms of order H/r or smaller, we find that the equations decouple into two subsystems. One of them corresponds to sound waves propagating in the vertical direction and the other describes MHD perturbations in the plane of the disc, with vanishing z component.

With these simplifying assumptions, the final linear system of equations that describes the MHD perturbations within the disc is,

$$i\omega\rho\delta\mathbf{v}_r - 2\rho\Omega\delta\mathbf{v}_\phi - \frac{B_0}{c}\delta\mathbf{J}_\phi = 0\,, \tag{2.29}$$

$$i\omega\rho\delta\mathbf{v}_\phi + \tfrac{1}{2}\rho\Omega\delta\mathbf{v}_r + \frac{B_0}{c}\delta\mathbf{J}_r = 0\,, \tag{2.30}$$

$$i\omega\delta\mathbf{B}_r - c\frac{\partial\delta\mathbf{E}_\phi}{\partial z} = 0\,, \tag{2.31}$$

$$i\omega\delta\mathbf{B}_\phi + c\frac{\partial\delta\mathbf{E}_r}{\partial z} + \tfrac{3}{2}\Omega\delta\mathbf{B}_r = 0\,, \tag{2.32}$$

$$\delta \mathbf{J}_r = -\frac{c}{4\pi}\frac{\partial \delta \mathbf{B}_\phi}{\partial z}\,, \tag{2.33}$$

$$\delta \mathbf{J}_\phi = \frac{c}{4\pi}\frac{\partial \delta \mathbf{B}_r}{\partial z}\,, \tag{2.34}$$

$$\delta \mathbf{J}_r = \sigma_2 \delta \mathbf{E}'_r - \sigma_1 \delta \mathbf{E}'_\phi\,, \tag{2.35}$$

$$\delta \mathbf{J}_\phi = \sigma_1 \delta \mathbf{E}'_r + \sigma_2 \delta \mathbf{E}'_\phi\,, \tag{2.36}$$

where $\delta \mathbf{E}_\phi$ and $\delta \mathbf{E}_r$ are the perturbations of the electric field in the laboratory frame, given by

$$\delta \mathbf{E}_\phi = \delta \mathbf{E}'_\phi + \frac{B_0}{c}\delta \mathbf{v}_r\,, \text{ and} \tag{2.37}$$

$$\delta \mathbf{E}_r = \delta \mathbf{E}'_r - \frac{B_0}{c}\delta \mathbf{v}_\phi\,. \tag{2.38}$$

We note that $\sigma_\parallel$, the component of the conductivity tensor parallel to the magnetic field, does not appear in the final linearised equations. Because the ambipolar diffusion and resistive conductivity regimes are differentiated by the value of $\sigma_\parallel$ (section 2.2.2), this means that during the linear stage of the MRI, under the adopted approximations, these regimes are identical.

2.3.2 Equations in dimensionless form

Equations (2.29) to (2.38) can be expressed in dimensionless form, normalising the variables as follows:

$$z^* = \frac{z}{H} \qquad \rho^* = \frac{\rho(r,z)}{\rho_0(r)} \qquad \delta \mathbf{B}^* = \frac{\delta \mathbf{B}}{B_0}$$

$$\delta \mathbf{v}^* = \frac{\delta \mathbf{v}}{c_s} \qquad \delta \mathbf{E}^* = \frac{c\delta \mathbf{E}}{c_s B_0} \qquad \delta \mathbf{E}'^* = \frac{c\delta \mathbf{E}'}{c_s B_0}$$

$$\delta \mathbf{J}^* = \frac{c\delta \mathbf{J}}{c_s B_0 \sigma_{\perp_0}} \qquad \sigma^* = \frac{\sigma}{\sigma_{\perp_0}} \qquad \sigma^*_\perp = \frac{\sigma_\perp}{\sigma_{\perp_0}}$$

Subscript 'o' is used to denote variables at the midplane of the disc. Effecting these changes and dropping the asterisks to keep the notation simple, we finally express the dimensionless system of equations in matrix form as:

$$\frac{d}{dz}\begin{pmatrix} B_r \\ B_\phi \\ E_r \\ E_\phi \end{pmatrix} = \begin{pmatrix} 0 & 0 & C_1A_1 & C_1A_2 \\ 0 & 0 & -C_1A_2 & C_1A_3 \\ -\frac{3}{2} & -\nu & 0 & 0 \\ \nu & 0 & 0 & 0 \end{pmatrix} \begin{pmatrix} B_r \\ B_\phi \\ E_r \\ E_\phi \end{pmatrix} \tag{2.39}$$

$$\delta\mathbf{J} = \sigma_\perp C_2 \begin{pmatrix} A_2 & -A_3 \\ A_1 & A_2 \end{pmatrix} \delta\mathbf{E} \tag{2.40}$$

$$\delta\mathbf{v} = \frac{\chi_o}{\rho}\frac{1}{1+\nu^2} \begin{pmatrix} -2 & \nu \\ -\nu & -\frac{1}{2} \end{pmatrix} \delta\mathbf{J} \tag{2.41}$$

$$\delta\mathbf{E}' = \frac{1}{{\sigma_\perp}^2} \begin{pmatrix} \sigma_2 & \sigma_1 \\ -\sigma_1 & -\sigma_2 \end{pmatrix} \delta\mathbf{J} \tag{2.42}$$

where

$$\nu = \frac{i\omega}{\Omega}\,, \tag{2.43}$$

$$C_1 = \chi_o\sigma_\perp \left(\frac{v_A}{c_s}\right)^{-2} C_2\,, \tag{2.44}$$

$$C_2 = \left[1 + \frac{\chi_o\sigma_\perp}{\rho}\frac{1}{1+\nu^2}\left(\frac{5}{2}\frac{\sigma_1}{\sigma_\perp} + 2\nu\frac{\sigma_2}{\sigma_\perp} + \frac{\chi_o\sigma_\perp}{\rho}\right)\right]^{-1}\,, \tag{2.45}$$

$$A_1 = \frac{\sigma_1}{\sigma_\perp} + 2\frac{\chi_o\sigma_\perp}{\rho}\frac{1}{1+\nu^2}\,, \tag{2.46}$$

$$A_2 = \frac{\sigma_2}{\sigma_\perp} + \nu\frac{\chi_o\sigma_\perp}{\rho}\frac{1}{1+\nu^2}\,, \text{ and} \tag{2.47}$$

$$A_3 = \frac{\sigma_1}{\sigma_\perp} + \frac{1}{2}\frac{\chi_o\sigma_\perp}{\rho}\frac{1}{1+\nu^2}\,. \tag{2.48}$$

In the above expressions,

$$v_A = \frac{B_o}{\sqrt{4\pi\rho_o}} \tag{2.49}$$

is the Alfvén speed at the midplane of the disc, and

$$\chi_o = \frac{\omega_{co}}{\Omega} = \frac{1}{\Omega}\frac{B_o^2\sigma_{\perp o}}{\rho_o c^2} \tag{2.50}$$

is a parameter that characterises the midplane coupling between the magnetic field and the disc (see section 2.3.3). To understand the information contained in this parameter it is useful to recall that the effect of finite conductivity is different for perturbations of different wavelengths. Finite conductivity is important when the term $c\nabla\times\mathbf{E}'$ in the induction equation (2.3) is of order $\nabla\times(\mathbf{v}\times\mathbf{B})$. Adopting a length scale $L \sim 1/k \sim v_A/\omega$ and $\sigma \sim \sigma_\perp$, it is found that these two terms are comparable when $kv_A \sim (c^2/4\pi)k^2/\sigma_\perp$, in other words, non-ideal effects will strongly modify wavemodes at, or above, the critical frequency,

$$\omega_c = \frac{B^2\sigma_\perp}{\rho c^2}\,. \tag{2.51}$$

It can be shown (W99) that in the limit $|\beta_j| \to \infty$, ω_c reduces to $\sum_j \gamma_j\rho_j$, the collision frequency of the neutrals with any of the charged species. Generally, ω_c is smaller than this value and much smaller than $\gamma_j\rho$, the collision frequency of charged species j with the neutrals. In dense clouds, $\omega_c \sim \gamma_G\rho_G$, which is the smallest $\gamma_j\rho_j$, the collision frequency of neutrals with grains. As $\rho_G \sim 0.01\rho$, the treatment of this study, restricted to $\omega < \gamma_j\rho$ by neglecting the inertia of the charged species, remains valid for $\omega \sim 100\omega_c$. For perturbations with lower frequencies (longer wavelength) than ω_c, ideal MHD (the flux-freezing approximation) is valid.

2.3.3 Parameters

As these equations reveal, three important parameters control the evolution of the fluid:

1. v_A/c_s, the ratio of the Alfvén speed to the isothermal sound speed of the gas at the midplane. It is a measure of the strength of the magnetic field. In ideal MHD unstable modes grow when the magnetic field is subthermal ($v_A/c_s < 1$). When $v_A \sim c_s$ the minimum wavelength of the instability is of the order of the scaleheight of the disc and the growth rate decreases rapidly.

2. χ_o, a parameter that characterises the strength of the coupling between the magnetic field and the disc at the midplane (see equation 2.50). It is given by the ratio of the critical frequency above which flux-freezing conditions break down and the dynamical frequency of the disc at the midplane. If $\chi_o = \omega_{co}/\Omega < 1$ the disc is poorly coupled to the disc at the frequencies of interest for dynamical analysis. As the growth rate of the most unstable modes are of order Ω in ideal MHD conditions, these are also the interesting frequencies for the study of this instability.

3. σ_1/σ_2, the ratio of the conductivity terms perpendicular to the magnetic field. It is an indication of the conductivity regime of the fluid, as discussed in section 2.2.2.

Note that the density of the disc decreases with z, so the local values of χ and v_A/c_s increase with height. The parameters of the model are defined as the corresponding values at the midplane.

It is common practice to characterise the magnetic coupling of a weakly ionised fluid by its electron density n_e. Before finishing this section, we discuss how χ relates to this fluid parameter. We begin by writing the magnetic Reynolds number as (e.g. Balbus & Terquem 2001),

$$\mathrm{Re_M} = \frac{v_A H}{\eta} = \frac{B^2 \sigma_\parallel}{\rho c^2} \frac{\sqrt{4\pi\rho}}{B} \frac{c_s}{\Omega} = \frac{\sigma_\parallel}{\sigma_\perp} \frac{\chi}{v_A/c_s}\,, \tag{2.52}$$

where we have used $\eta = c^2/4\pi\sigma_\parallel$. If ions and electrons are the only charged species, then

$$\chi = \frac{v_A}{c_s} \frac{\mathrm{Re_M}}{(1+\beta_e^2)^{1/2}(1+\beta_i^2)^{1/2}}\,. \tag{2.53}$$

In the resistive regime, $|\beta| \ll 1$ for both charged species and (2.53) shows that the criterion for non-Hall MRI perturbations to grow (W99), $\chi > v_A/c_s$, is equivalent to $\mathrm{Re_M} > 1$.

We can now obtain an expression for χ in terms of the electron fraction $x_e = n_e/n_H$ at the midplane,

$$\chi = \frac{1}{\Omega}\frac{B^2\sigma_\perp}{\rho c^2} = \frac{en_eB}{c\Omega\rho}\frac{\beta_i - \beta_e}{(1+\beta_e^2)^{1/2}(1+\beta_i^2)^{1/2}} \approx \frac{n_e < \sigma v > m_e}{(m_e+m_n)\Omega}\frac{\beta_e^2}{(1+\beta_e^2)^{1/2}}, \quad (2.54)$$

where we used expression (2.20) for $\sigma_\perp$ and assumed $\beta_i \ll |\beta_e|$. In the above equation

$$< \sigma v > \approx 1 \times 10^{-15}\left(\frac{128kT}{9\pi m_e}\right)^{1/2} \mathrm{cm}^{-2} \quad (2.55)$$

is the momentum-transfer rate coefficient for electron-neutral scattering. Note that the dependence of χ on magnetic field strength now enters only through the electron Hall parameter β_e. Following Fromang, Terquem & Balbus (2003) we assume that grains have settled out and the electron (and ion) number density is determined by the recombination of metal ions given by,

$$n_e \approx \left(\frac{\zeta n_{\mathrm{H}}}{\alpha}\right)^{1/2}, \quad (2.56)$$

where $\alpha \approx 3\times10^{-11}T^{-1/2}\,\mathrm{cm}^3\,\mathrm{s}^{-1}$ is the radiative recombination rate for metal ions. The ionisation rate ζ is assumed to be due to cosmic rays at a rate $10^{-17}\exp(-\Sigma/96)$ $\mathrm{g\,cm^{-2}\,s^{-1}\,H^{-1}}$ where Σ is the disc surface density. This dominates x-ray ionisation for the column densities we shall consider here. Results are shown in Table 3.1 for a nominal 1 solar mass star and $B = 10\,\mathrm{mG}$.

For this strength of the magnetic field, $|\beta_e| \ll 1$ at 1 AU and χ scales as B^2 (up to about 200 mG) at this radius. On the other hand, β_e is greater than 1 at 5 and 10 AU, so χ will scale linearly with B (see equation 2.54). In particular for $B = 100$ mG at 1 AU, $\chi \approx 0.00088$, consistent with the detailed calculations in Wardle (2003).

2.4 Boundary Conditions

To solve equations (2.39) to (2.42) it is necessary first to integrate the system of ordinary differential equations (ODE) in (2.39). This problem can be treated as

Table 2.1 Comparison of the magnetic coupling parameter χ_o and the ionisation fraction x_e at the midplane for different radial positions r_o, with $B = 10$ mG and assuming grains have settled out (Fromang, Terquem & Balbus 2002). Also shown are the assumed temperature T_o and calculated values of n_H, v_A/c_s, ζ, β_e and β_i.

r_o (AU)	T_o (K)	n_H (cm^{-3})	v_A/c_s	ζ (s^{-1}H^{-1})	$\lvert\beta_e\rvert$	β_i	x_e	χ_o
1	280	6×10^{14}	0.00076	5.76×10^{-22}	0.035	7.68×10^{-5}	7.32×10^{-13}	8.9×10^{-6}
5	130	7×10^{12}	0.010	4.81×10^{-18}	4.44	6.58×10^{-3}	5.11×10^{-10}	1.9
10	90	1×10^{12}	0.033	9.76×10^{-18}	37.31	0.046	1.76×10^{-9}	19

a two-point boundary value problem for coupled ODE. Five boundary conditions must be formulated, prescribed either at the midplane or at the surface of the disc.

At the midplane: A set of boundary conditions can be arrived at by asuming fluid variables have either 'odd' or 'even' symmetry about the midplane. 'Odd' symmetry means the variable is an odd function of z and vanishes at $z = 0$. Conversely, when 'even' symmetry is applied, the variable is assumed to be an even function of z and its gradient is zero at the midplane. In this study we applied the odd - even symmetry criteria to the perturbations in the magnetic field, $\delta\mathbf{B}(z) = \pm\delta\mathbf{B}(-z)$, where the upper (lower) sign corresponds to even (odd) symmetry conditions. This contrasts with Lovelace, Wang & Sulkanen (1987), who applied the symmetry criteria to the flux function $\Psi(r, z) = rA_\phi$ with A_ϕ the toroidal component of the vector potential and obtained $\delta\mathbf{B}_{r,\phi}(r, z) = \mp\delta\mathbf{B}_{r,\phi}(r, -z)$ as their symmetry criteria. The symmetry of a particular fluid variable is assigned arbitrarily, subject to the constraint that fluid equations are satisfied. This means that two sets of boundary conditions are equally valid, obtained by reversing the assumed symmetry of the fluid variables. Perturbations obtained with a particular set of boundary conditions are displaced a quarter of a wavelength from those found with the other one. The growth rates of these solutions lie at intermediate points of the curve ν vs k obtained from the local analysis (W99), as expected. Evidently, no generality is lost by focusing in one of these two possible sets of solutions. We compare the growth rate versus number of nodes of perturbations obtained with 'odd' and 'even' symmetry in section 2.5.2 (Comparison with local analysis). For the rest of the analysis presented in this study we chose to assign odd symmetry to δB_r and δB_ϕ, so they vanish at $z = 0$. This gives us two boundary conditions at the midplane. As the equations are linear, their overall scaling is arbitrary, so a third boundary condition can be obtained by setting one of the fluid variables to any convenient value. To that effect, we assigned a value of 1 to $\delta E'_r$. Summarising, three boundary conditions are applied at the midplane:

$$\delta B_r = \delta B_\phi = 0, \text{ and}$$

$$\delta E'_r = 1\,.$$

At the surface: At sufficiently high z above the midplane, ideal MHD conditions hold. This assumption is appropriate in this case because the local coupling parameter χ is inversely proportional to the density and so it is stronger at higher z regions where the density is smaller. When $\chi > 10$ the growth rate and characteristic wavenumber of unstable modes differ little from the ideal limit (W99), so even though for simplicity we have assumed the conductivity tensor to be spatially constant, we can assume that flux-freezing conditions hold at the surface and the local dispersion relation is $kv_A = \Omega$ (Balbus & Hawley 1991). As the Alfvén speed increases with $\rho^{1/2}$, the wavelengths of magnetic field perturbations increase with z and given the dependency of ρ with z (see equation 2.28), must tend to infinity as $z \to \infty$. The displacements in the plane of the disc of an infinitely stretched perturbation should effectively vanish, so δB_r and δB_ϕ should be zero at infinity. This gives us the remaining two boundary conditions required to integrate the system of equations (2.39). Consistently with them, both $\delta\mathbf{E}'$ and $\delta\mathbf{J}$ vanish as well.

Interestingly, this solution is consistent with $\delta\mathbf{E}$ and $\delta\mathbf{v}$ being non-zero at infinity. The only requirement is that the gradient of the velocity in the vertical direction $\partial\delta\mathbf{v}/\partial z$ be zero when $z \to \infty$, to prevent any horizontal stretching of the magnetic field. It may seem puzzling at first that $\delta\mathbf{v}$ is non-vanishing at infinity. This can be understood taking into account that these perturbations travel to infinity in a finite time t_∞ given by,

$$t_\infty = \int_0^\infty \frac{dz}{v_{Al}} = \frac{H}{v_A}\int_0^\infty exp\left(-\frac{z^2}{4}\right)dz = \sqrt{\pi}\frac{H}{v_A}\,, \tag{2.57}$$

where z is the vertical coordinate in units of the scaleheight H and v_{Al} is the local value of the Alfvén speed. Because of this finite travel time to infinity, the fluid can retain a finite velocity when $z \to \infty$. Furthermore, through equations (2.37) and (2.38) it is clear that $\delta\mathbf{E}$, the perturbations in the electric field as seen from the laboratory frame, are finite at infinity as well.

These boundary conditions are strictly valid at infinity, but will also hold at a boundary located sufficiently high above the midplane. We chose to locate

Table 2.2 Comparison of maximum growth rate ν_{max} and number of nodes N of the fastest growing modes for all conductivity regimes and two different locations of the boundary. In all cases $v_A/c_s = 0.1$ and $\chi_o = 10$.

	$z/H = 5$		$z/H = 7$	
Conductivity Regime	ν_{max}	N	ν_{max}	N
Ambipolar Diffusion	0.7303865	5	0.7303869	5
Hall limit ($\sigma_1 B_z > 0$)	0.7498761	5	0.7498761	5
Hall limit ($\sigma_1 B_z < 0$)	0.7461857	5	0.7461854	5
Comparable conductivities	0.7345455	5	0.7345459	5
Opposite conductivities	0.7340035	5	0.7340039	5

the boundary at $z/H = 5$ after confirming that increasing this height does not significantly affect either the structure or the growth rate of unstable modes. This can be appreciated in Table 2.2, which compares the maximum growth rate ν_{max} and number of nodes N (proxy for wavenumber) of the perturbations in all conductivity regimes for two different locations of the boundary. Summarising, the boundary conditions adopted at the surface are:

$$\delta B_r = \delta B_\phi = 0\,,$$

at $z/H = 5$.

This system of equations is solved as a two-point boundary value problem for coupled ODE by 'shooting' from the midplane to the surface of the disc and simultaneously adjusting the growth rate ν and $\delta E'_\phi$ until the solution converges.

2.5 Results

2.5.1 Test Models

We solved the system of equations (2.39) for different conductivity regimes, coupling between fluid components and initial magnetic field strengths. As discussed in section 2.3.1, under the linear approximation and disc model adopted in this thesis, the ambipolar diffusion and resistive conductivity regimes are identical, so even though throughout this work we have labelled the case when $\sigma_1 = 0$ as the 'ambipolar

diffusion' limit, it should be kept in mind that this condition describes the resistive regime as well. Two different Hall limits exist, as the growth rate of the MRI depends on the orientation of the initial magnetic field with respect to the disc angular velocity vector $\mathbf{\Omega}$ (W99). The case when $\mathbf{B}_o$ is parallel (antiparallel) to $\mathbf{\Omega}$ is characterised by $\sigma_1 B_z > 0$ ($\sigma_1 B_z < 0$).

We calculated the growth rate and vertical structure of all unstable perturbations for different conductivity regimes with $v_A/c_s = 0.1$. The degree of coupling between the magnetic field and the neutral component of the fluid was characterised by either $\chi_o = 10$ (good coupling) or $\chi_o = 2$ or 1 (poor coupling). The choice of χ_o for the low coupling analysis is dependent on the conductivity regime of the fluid. We took $\chi_o = 1$ for all regimes, except the Hall ($\sigma_1 B_z < 0$) limit, where $\chi_o = 2$ was adopted as our code fails to converge for $\chi < 2$. In this regime, the local analysis shows that when $0.5 < \chi < 2$ all wavenumbers grow (W99). We believe that this complex structure of the perturbations at ever increasing k prevents our code from converging when $\chi_o < 2$.

We also examined the dependency of the structure of the fastest growing modes, their growth rate and the height of maximum amplitude, with the coupling χ_o and the strength of the magnetic field for all conductivity regimes. To study the effect of the magnetic coupling, the value of v_A/c_s was fixed at 0.1. The impact of the strength of the field was explored for good and poor coupling conditions.

Finally, we studied the dependency of the growth rate of the most unstable perturbations with the coupling χ_o for $v_A/c_s = 0.1$ and 0.01 and with the magnetic field strength for $\chi_o = 10$, 2 and 0.1.

The relative values of σ_1 and σ_2 used to characterise each conductivity regime, together with the values of v_A/c_s and χ_o used to explore the structure of the perturbations are summarised in Table 2.3.

2.5.2 Comparison with local analysis

The linear growth of the MRI as a function of wavenumber in a local analysis shows that ν vs k generally takes the form of inverted quadratics (W99). The local wavenumber of the perturbations change with z, so we use the number of nodes of δB_r over the entire thickness of the disc, from $z = -5$ to $z = +5$, as a proxy for the wavenumber k to compare our results with those of W99. Results are shown in

Table 2.3 Relative values of the components of the conductivity tensor perpendicular to the magnetic field σ_1 and σ_2 and fiducial values of the coupling parameters χ_o (good coupling, poor coupling limits) and v_A/c_s adopted to explore the structure of the perturbations for all conductivity regimes.

Conductivity Regime	σ	χ_o	v_A/c_s
Ambipolar Diffusion	$\sigma_1 = 0$	10, 1	0.1
Hall Limit $\sigma_1 B_z > 0$	$\sigma_2 = 0$, $\sigma_1 > 0$	10, 1	0.1
Hall Limit $\sigma_1 B_z < 0$	$\sigma_2 = 0$, $\sigma_1 < 0$	10, 2	0.1
Comparable conductivities	$\sigma_1 = \sigma_2$	10, 1	0.1
Opposite conductivities	$\sigma_1 = -\sigma_2$	10, 1	0.1

Fig. 2.1 for the ambipolar diffusion and Hall ($\sigma_1 B_z > 0$) limits for good and poor coupling. In both regimes the reduction of the wavenumber of the fastest growing perturbation with χ_o is obtained, as expected from the local analysis. Reducing χ_o also diminishes the growth rate of the instability in the ambipolar diffusion limit, but ν remains unchanged for the Hall regime, as expected from the local results.

These results confirm our expectation that applying boundary conditions and integrating the fluid equations in the vertical direction would restrict the unstable frequencies from the continuous curve ν vs k obtained in the local analysis to a discrete subset of global unstable modes supported by the fluid.

Also shown as crosses in Fig. 2.1 are the growth rates obtained with 'even' boundary conditions applied to δB_r and δB_ϕ at the midplane (see section 2.4), for the ambipolar diffusion limit with $\chi_o = 10$. As expected, the perturbations are displaced a quarter of a wavelength (one node) from those obtained with 'odd' boundary conditions.

2.5.3 Structure of the Perturbations

Fig. 2.2 shows the perturbations in all fluid variables as a function of height, from the midplane ($z/H = 0$) to the surface of the disc ($z/H = 5$), for the ambipolar diffusion regime and good coupling ($\chi_o = 10$). They are obtained through equations (2.40) - (2.42) once the ODE system (2.39) has been integrated. Note the non-zero values of $\delta\mathbf{v}$ and $\delta\mathbf{E}$ at the surface, as discussed in section 2.4. From this point onwards, discussion will be focussed in the perturbations of the magnetic field only.

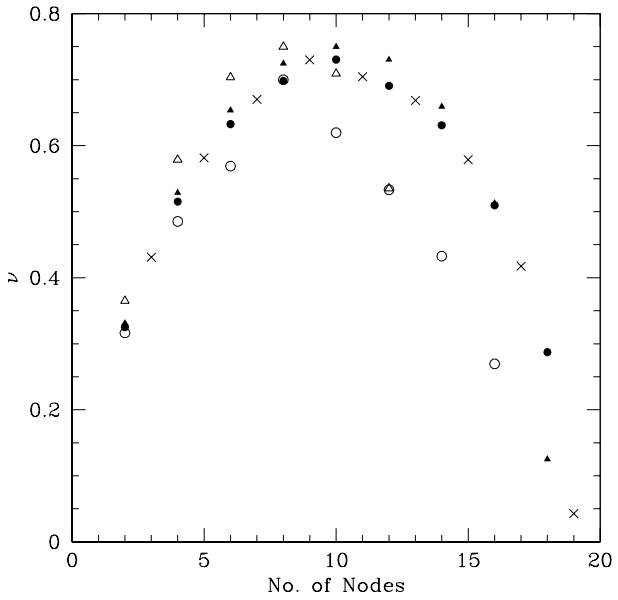

Figure 2.1 Growth rate versus number of nodes (proxy for wavenumber) of the MRI for different conductivity regimes and coupling at the midplane χ_o. Circles show the ambipolar diffusion limit ($\sigma_1 = 0$) and triangles the Hall limit ($\sigma_2 = 0$, $\sigma_1 B_z > 0$). Filled symbols correspond to the good coupling case $\chi_o = 10$ and open ones to the poor coupling case $\chi_o = 1$. Crosses show the ambipolar diffusion limit with 'even' boundary conditions applied to δB_r and δB_ϕ. Note that results in this case are displaced a quarter of a wavelength (one node) from those obtained with 'odd' boundary conditions. In all cases $v_A/c_s = 0.1$.

Unless otherwise stated, the radial component of the field δB_r is plotted with a solid line and the azimuthal component δB_ϕ with a dashed line. As the overall scale of our linear equations is arbitrary, plots depicting the structure of the perturbations either do not show the scale of the vertical axis (corresponding to the amplitude of the perturbations) or show a conveniently normalised scale, for reference purposes.

Effect of the Conductivity Regime

Fig. 2.3 compares the structure of all unstable perturbations for the ambipolar diffusion and Hall ($\sigma_1 B_z > 0$) regimes under good coupling ($\chi_o = 10$). The modes are ordered by the number of nodes. We find that at small ν, the structure of the perturbations in both cases is very similar, but significant differences arise when the growth rate is close to maximum. Then, ambipolar diffusion perturbations peak

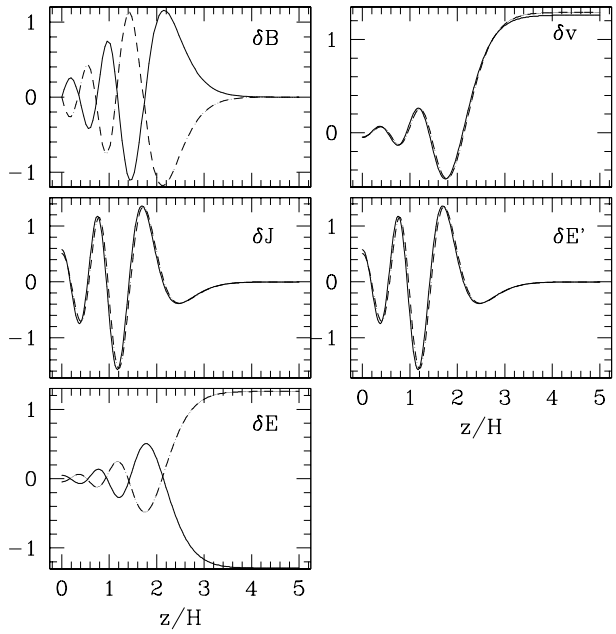

Figure 2.2 Structure of the perturbations in all fluid variables as a function of height for the most unstable mode in the ambipolar diffusion limit, for good coupling ($\chi_o = 10$) and $v_A/c_s = 0.1$. The growth rate is $\nu = 0.7304$. Note the non-zero values of $\delta\mathbf{v}$ and $\delta\mathbf{E}'$ at the surface, due to the finite travel time to infinity of the perturbations.

at the node closest to the surface, while Hall ($\sigma_1 B_z > 0$) ones peak closest to the midplane. This behaviour is linked to the change in the local coupling χ with z and its effect in the structure of the perturbations for different conductivity regimes. It will be discussed further in the next section. At this good coupling level, there are no appreciable differences in the structure or growth rate of perturbations between both Hall limits results, as expected from the local analysis (W99). When both conductivity components are present ($\sigma_1 = \pm\sigma_2$ cases), the structure of the perturbations is similar to the ambipolar diffusion limit. This property is also dependent on the value of the local coupling χ and will be analysed in the next section. We found 9 to 10 unstable perturbations in all cases.

Under low coupling conditions, $\chi_o = 2$ or 1 depending on the conductivity regime (see Table 2.3), fewer unstable modes grow for both the ambipolar diffusion, Hall ($\sigma_1 B_z > 0$) and the comparable conductivities ($\sigma_1 = \sigma_2$) regimes. Six to eight unstable perturbations are found in these cases. As expected from the local analysis (W99), the range of wavenumbers for which unstable modes exist is reduced as

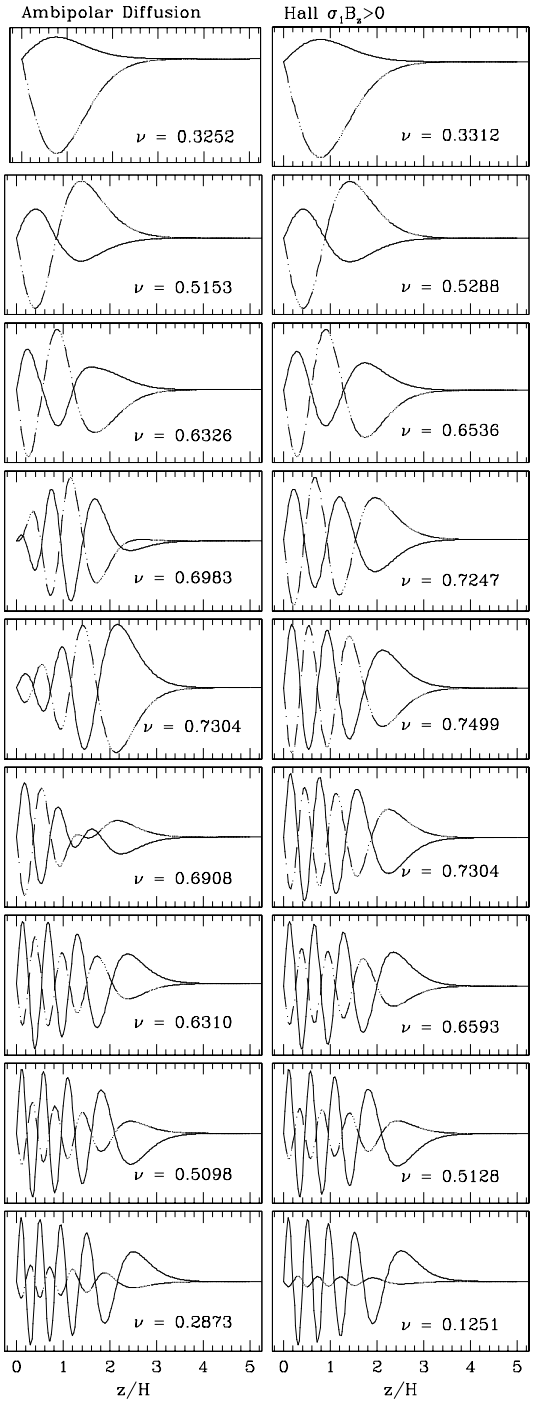

Figure 2.3 Structure and growth rate of all unstable modes of the MRI for the ambipolar diffusion ($\sigma_1 = 0$) and Hall ($\sigma_2 = 0$, $\sigma_1 B_z > 0$) cases. In all plots $\chi_o = 10$ and $v_A/c_s = 0.1$. For this good coupling, there are no differences between both Hall limits. When both conductivity components are present ($\sigma_1 = \pm\sigma_2$ cases), results resemble the ambipolar diffusion limit shown.

compared with the good coupling cases.

Results are quite different for the two remaining conductivity regimes (Hall $\sigma_1 B_z < 0$ and $\sigma_1 = -\sigma_2$). More unstable modes are found in these cases; 12 in the opposite conductivities case ($\sigma_1 = -\sigma_2$) and a total of 27 for the Hall ($\sigma_1 B_z < 0$) limit. In this last case in particular, despite the low coupling of ionised and neutral components of the fluid, unstable modes have a very complex structure (high wavenumber). Fig. 2.4 shows the structure of two such modes at the low growth rate, high wavenumber region of the ν - k space. Note that unstable modes are so closely spaced that increasing the number of nodes by a few only maginally changes their wavenumber and has little effect on their growth rate. This complexity is expected from the form of the dispersion relation at low coupling from the local analysis (W99). Non-linear simulations (Sano & Stone 2002a, b) confirm that the many growing modes in this regime strongly interact with each other and the instability develops into MHD turbulence. This turbulence is a transient phase that eventually dies away in two-dimensional simulations (Sano & Stone 2002a) but it is sustained in full three-dimensional models (Sano & Stone 2002b). In both cases the non-emergence of the typical two-channel flow obtained in other regimes is noted by the authors.

Finally, some of the perturbations show a structure resembling an interference pattern (see Fig. 2.5). They were obtained specifically in regimes where ambipolar diffusion is present, for good and poor coupling, but not in any of the Hall limits. This pattern can be explained recalling that local results show that two unstable modes exist with the same growth rate and different wavenumber. Despite this, just one global mode is found for each ν in this analysis. Again, the application of boundary conditions and integration along the vertical direction restricts global unstable modes from those possible under a local analysis. The interference pattern suggests that global modes are a superposition of two WKB modes with (nearly) the same growth rate and which are not global solutions themselves. The interference of Fig. 2.5 was successfully replicated through the superposition of two local modes with $\nu = 0.7004$ using the analytical expresions in W99 for the ambipolar diffusion limit.

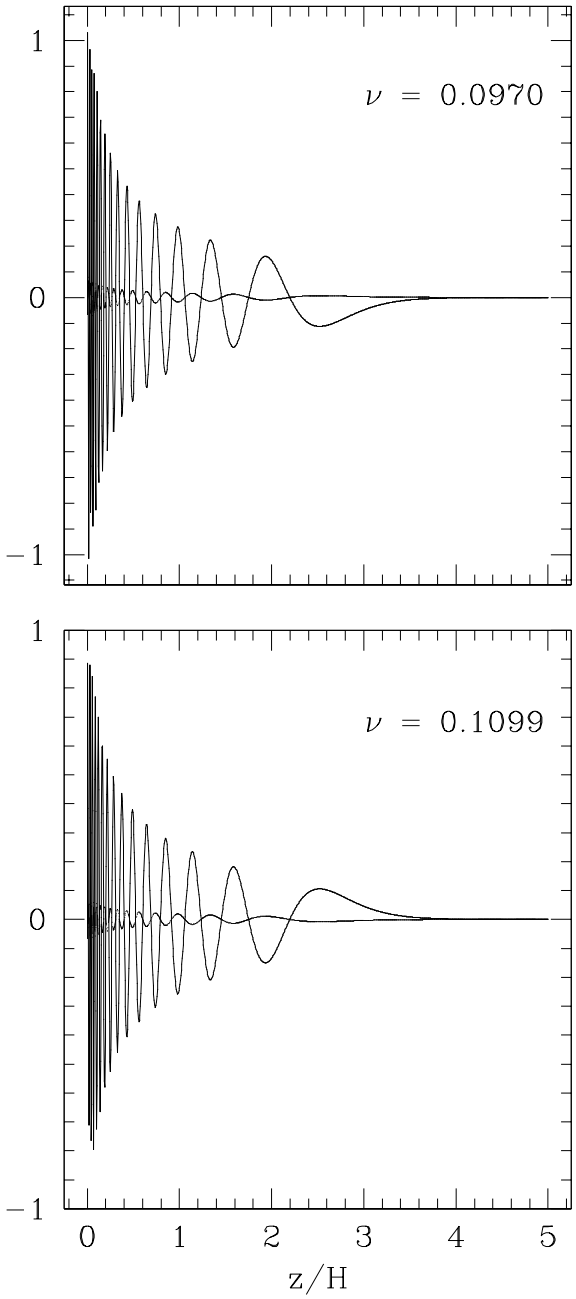

Figure 2.4 Structure of two unstable modes in the Hall ($\sigma_1 B_z < 0$) limit for poor coupling ($\chi_o = 2$) and $v_A/c_s = 0.1$. Note the complex structure of the perturbations (high wavenumber). Unstable modes are so closely spaced that increasing the number of nodes only marginally changes their wavenumber and growth rate.

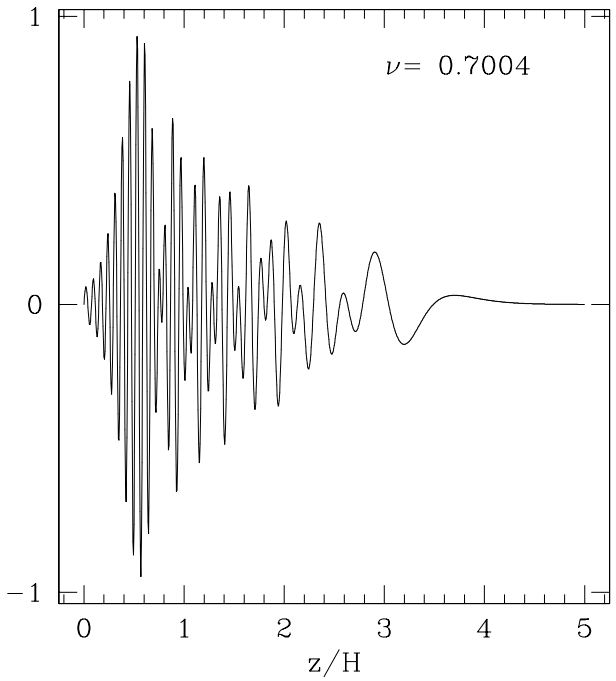

Figure 2.5 Structure of an unstable mode in the ambipolar diffusion limit ($\sigma_1 = 0$) for good coupling ($\chi_o = 10$) and $v_A/c_s = 0.01$. Note the interference pattern of the perturbation, which suggests that this global mode is a superposition of two WKB modes of similar growth rates.

Effect of the coupling parameter χ_o

Fig. 2.6 compares the structure and growth rate of the most unstable modes of the MRI for all conductivity regimes as a function of the coupling parameter χ_o. In all cases $v_A/c_s = 0.1$. We notice that reducing the coupling χ_o causes the wavenumber (i.e. the number of nodes) of unstable modes to diminish in all conductivity regimes except the Hall $\sigma_1 B_z < 0$ limit (rightmost column of Fig. 2.6), for which this dependency is inverted. The growth rate is also reduced at a rate that depends on the conductivity regime of the fluid. These results are expected from the findings of the local analysis (W99).

It is evident from Fig. 2.6 that at very high magnetic coupling ($\chi_o \approx 100$), the fluid is close to ideal MHD conditions and results obtained in all conductivity regimes are alike. When the coupling is reduced to $\chi_o \approx 10$, we begin to appreciate differences between them. In particular, the amplitude of the perturbations when ambipolar diffusion is present peaks close to the surface while in both Hall limits the

maximum amplitude is closest to the midplane. This is more clearly appreciated in Fig. 2.7, which plots the height of maximum amplitude of the fastest growing modes as a function of the coupling parameter χ_o and the conductivity regime of the fluid for $v_A/c_s = 0.1$. This figure shows that pure Hall regimes ($\sigma_1 B_z > 0$ and $\sigma_1 B_z < 0$) peak closer to the midplane, for all χ_o studied, than the cases when ambipolar diffusion is present. This behaviour can be explained by the dependency of the local growth of the instability with χ for different conductivity regimes. The maximum growth rate of ambipolar diffusion perturbations increases with the local χ (W99), which in turn is a function of height. As a result, at higher z, the local growth of the instability increases, driving the amplitude of global perturbations to increase. Hall ($\sigma_1 B_z > 0$) perturbations, on the contrary, have the same ν_{max} for all χ, so the instability is not driven from any particular vertical location, which explains the flatness of their envelope. This also explains why in Fig. 2.3 the differences between these regimes are apparent at close to maximum growth: The increment in the local growth rate with the coupling χ is less marked for slow growing perturbations. This is also appreciated in the local analysis by the form of the dispersion relation for different χ in the ambipolar diffusion regime (W99).

It is also clear from Fig. 2.7 that perturbations in the ambipolar diffusion and Hall ($\sigma_1 B_z > 0$) limits peak at higher z when χ_o is reduced. This dependency is driven by the reduction of the wavenumber of most unstable perturbations with the coupling in these regimes (W99, see also Fig. 2.6). On the contrary, in the Hall ($\sigma_1 B_z < 0$) limit, the wavenumber of the fastest growing mode increases as χ_o is reduced and the perturbations peak closer to the midplane with weaker χ_o.

Finally, looking at the first three columns of Fig. 2.6 it is evident that the structure of unstable modes in the $\sigma_1 = \pm\sigma_2$ conductivity regimes are remarkably similar to the ambipolar diffusion limit shown in the leftmost column of the figure for $\chi_o \gtrsim v_A/c_s = 0.1$. When the coupling is weaker than this value, the structure of unstable modes in these regimes is no longer alike. To explain this we recall that the minimum degree of coupling for unstable modes to grow, determined by the requirement that a wavelength fit in the disc scaleheight, is given by $\chi \gtrsim v_A/c_s$ in the ambipolar diffusion limit, and $\chi \gtrsim {v_A}^2/{c_s}^2$ in the Hall case (W99). For $\chi_o \lesssim 0.1$ then, the growth rate of ambipolar diffusion ($\sigma_1 = 0$) perturbations is expected to drop markedly and the envelope of the perturbations will be mainly determined by the Hall effect. This transition in both $\sigma_1 = \pm\sigma_2$ cases, is clearly seen in Fig. 2.7.

In both cases, for $\chi_o \gtrsim 0.1$ the perturbations resemble the ambipolar diffusion limit ($\sigma_1 = 0$). In the $\sigma_1 = \sigma_2$ regime, when $\chi_o < v_A/c_s$ the perturbations resemble those in the Hall ($\sigma_1 B_z > 0$) limit (compare lowest panels in the second and fourth columns of Fig. 2.6), consistent with the notion that ambipolar diffusion effects are no longer important in this region of parameter space. This implies a constant ν_{max} for weaker χ_o, so the perturbations tend to peak closer to the midplane. On the contrary, in the $\sigma_1 = -\sigma_2$ case, ν_{max} continues to diminish with χ once $\chi < v_A/c_s$ (W99). In this case, the range of growing modes is always finite (as opposed to the Hall $\sigma_1 B_z < 0$ limit) and there is a fastest growing mode for every χ. As a result, the instability is driven at intermediate z (as in the ambipolar diffusion limit) and accordingly, the perturbations peak at higher z with decreasing χ_o. The height of maximum amplitude increases faster as χ_o is reduced in this regime than in the ambipolar diffusion limit. This occurs because ν_{max} for a given local χ is greater in this case (W99, see also section 2.5.4) so global perturbations are amplified even further.

Effect of the Magnetic Field Strength

In ideal MHD, the weaker the magnetic field the higher the minimum wavenumber of the perturbations (Balbus & Hawley 1991). The results of this study are consistent with this finding. With $v_A/c_s \sim 0.005$ the perturbations grow with very high wavenumbers in all conductivity regimes. This can be appreciated in Fig. 2.8 and 2.9 for the ambipolar diffusion and Hall ($\sigma_1 B_z > 0$) limits, respectively, for good coupling ($\chi_o = 10$). At this χ_o, solutions for both Hall limits are similar. Also, $\sigma_1 = \pm\sigma_2$ regimes are similar to the ambipolar diffusion limit, as expected. Note the interference pattern of perturbations in lower panels of Fig. 2.8.

We also studied the dependency of the height of maximum amplitude with the strength of the magnetic field (Fig. 2.10) for good ($\chi_o = 10$) and poor coupling ($\chi_o = 2$). In the former case, when ambipolar diffusion is present, with and without the Hall effect and regardless of the sign of $\sigma_1 B_z$, the location of maximum amplitude of the fastest growing perturbations as a function of v_A/c_s is similar, which is expected as $\chi_o > v_A/c_s$ (see Fig. 2.10, panels *a*, *b* and *c*). We obtained unstable modes for v_A/c_s up to 1. As v_A/c_s is reduced from this value, the perturbations peak at higher z until $v_A/c_s \sim 0.04$. However, the location of maximum amplitude begins to

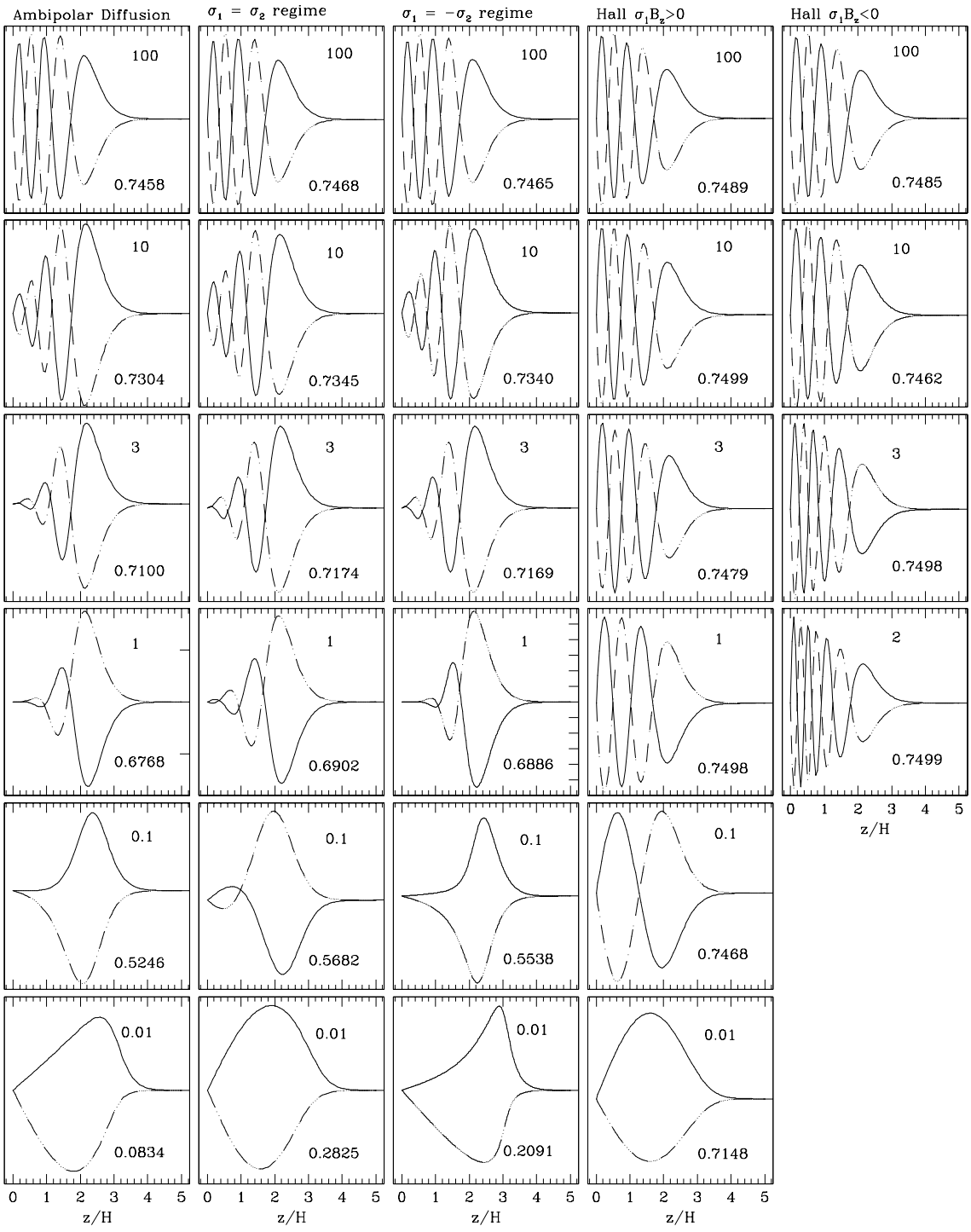

Figure 2.6 Structure and growth rate of the most unstable modes of the MRI for all conductivity regimes and different values of χ_o. In all cases $v_A/c_s = 0.1$. The value of the coupling parameter χ_o is indicated at the top right corner of each panel. The growth rate (ν) of the perturbations is shown in the lower right corner. Note that the Hall $\sigma_1 B_z < 0$ regime is explored for $\chi_o \geq 2$ as in this region of parameter space the range of wavenumbers for which local unstable modes exist becomes infinite (W99).

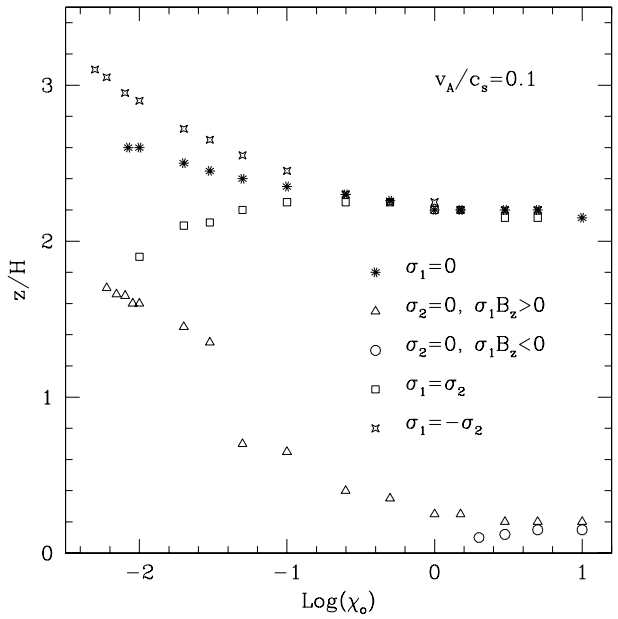

Figure 2.7 Height of maximum amplitude of the most unstable perturbations as a function of χ_o for all conductivity regimes. In all cases $v_A/c_s = 0.1$

diminish as the field is further reduced, which could be caused by the interference pattern, and very high wavenumber, of the perturbations (see also Fig. 2.8). The height of maximum amplitude peaks at $z \sim 2.8$.

In both Hall limits the height of maximum amplitude increases with the strength of the magnetic field until $v_A/c_s \sim 0.3$ and then remains unaffected with further increments of v_A/c_s (panels d and e of Fig. 2.10). This occurs because as the strength of the magnetic field increases, the wavenumber of the perturbations diminish, which pushes the maximum amplitude to higher z. For $v_A/c_s \sim 0.3$ the perturbations have only one node, so any further increase in the magnetic field strength have little effect in the location of the maximum amplitude.

In the low coupling case results are very similar to the $\chi_o = 10$ cases. We note that in regimes where ambipolar diffusion is present (left hand side panels of Fig. 2.10), perturbations tend to peak at a lower z/H than in the good coupling cases when $v_A/c_s \lesssim 0.1$. In the Hall ($\sigma_1 B_z < 0$) regime, there are unstable modes for 'suprathermal' field strengths (v_A/c_s up to 2.9). This will be further analysed in section 2.5.4, dealing with the dependency of the growth rate of this instability with the strength of the magnetic field. In this case, the height of maximum amplitude peaks at $v_A/c_s \approx 0.5$ and then gradually diminishes as the field is incremented

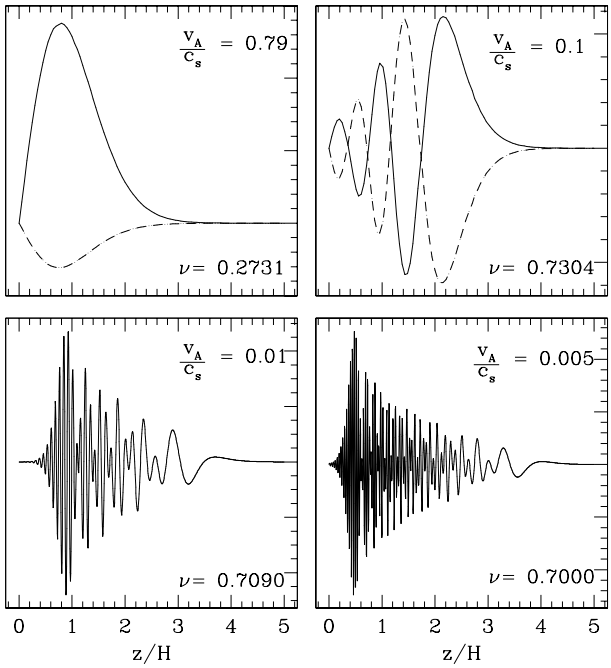

Figure 2.8 Structure as a function of height and growth rate of the MRI for different choices of v_A/c_s under the ambipolar diffusion limit ($\sigma_1 = 0$) and good coupling $\chi_o = 10$. The value of v_A/c_s is indicated at the top right corner of each panel. The growth rate is shown in the lower right corner.

beyond this value.

2.5.4 The perturbations in parameter space

Effect of the coupling

Fig. 2.11 shows the growth rate of the most unstable modes as a function of the coupling χ_o for all conductivity regimes with $v_A/c_s = 0.1$ (top panel) and 0.01 (bottom panel). The Hall ($\sigma_1 B_z < 0$) limit could not be modelled for $\chi_o < 2$ because in this region of parameter space the range of wavenumbers for which unstable modes grow becomes infinite (see section 2.5.1). We find that at the good coupling limit the instability grows at a rate similar to its ideal value of 0.75Ω for all conductivity regimes. As the coupling diminishes, the growth rate is reduced at a rate that depends on the conductivity regime of the fluid. In the Hall ($\sigma_1 B_z > 0$) case the growth rate remains unaffected until $\chi_o \sim 0.01$, and then diminishes drastically to 0.1Ω when $\chi_o \sim 0.005$. The ambipolar diffusion limit has a much more gradual

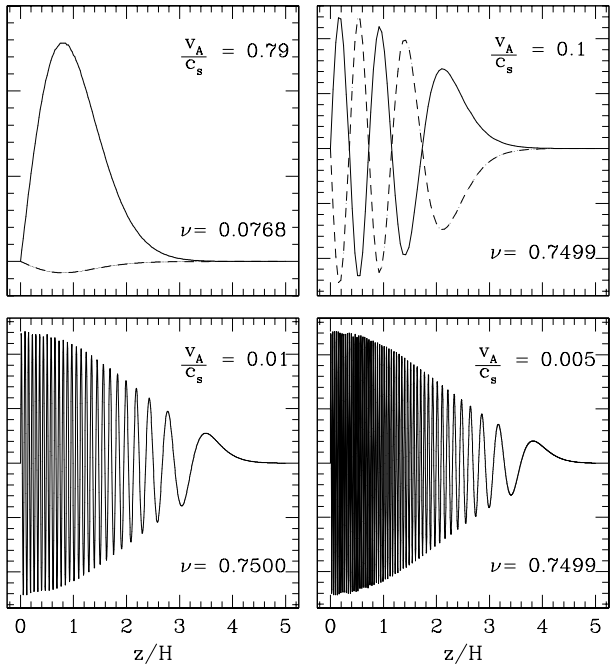

Figure 2.9 As for Fig. 2.8, but for the Hall limit $\sigma_1 B_z > 0$. The Hall limit when $\sigma_1 B_z < 0$ (not shown) exhibits the same dependency with v_A/c_s for this χ_o.

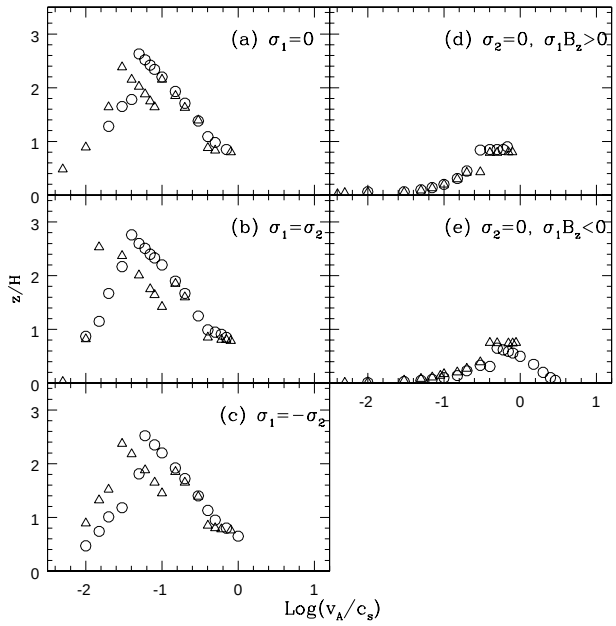

Figure 2.10 Height of maximum amplitude of the perturbations as a function of v_A/c_s, for all conductivity regimes. Triangles correspond to good coupling ($\chi_o = 10$) and circles to poor coupling ($\chi_o = 2$).

reduction of ν_{max} with χ_o. In this case, the growth rate departs significantly from the ideal value for $\chi_o \sim 0.1$ and then drops rapidly, reaching $\sim 0.007\Omega$ for $\chi_o \sim 0.008$. This is in agreement with findings by W99 that unstable modes grow when $\chi \gtrsim v_A/c_s$ in the ambipolar diffusion limit, and $\chi \gtrsim {v_A}^2/{c_s}^2$ in the Hall case (see also section 2.5.3). When χ is less than these values, perturbations are strongly damped.

When $v_A/c_s \sim 0.01$ (bottom panel of Fig. 2.11), the growth of Hall ($\sigma_1 B_z > 0$) perturbations is constant at about the ideal rate 0.75Ω until $\chi_o \sim 10^{-4}$. Below this, it plummets to zero as expected. On the contrary, in the ambipolar diffusion and $\sigma_1 = \pm\sigma_2$ regimes, ν_{max} begins to diminish much sooner. It is also noticed that, in the ambipolar diffusion and $\sigma_1 = \sigma_2$ cases, the growth rate increases again after reaching a minimum for $\chi_o \sim 0.05$. This is caused by the high wavenumber of the perturbations due to the weakness of the magnetic field. In these conditions global effects (stratification) are less important and the maximum growth rate diminishes with the coupling as per local results (W99). As the wavenumbers of the perturbations decrease when χ_o is reduced, for sufficiently low χ_o (~ 0.05), k is low enough for global effects to be important again and modify the growth rate of unstable perturbations. With the local χ increasing with height above the midplane, stratification will tend to increase the growth of global modes at low χ_o.

Effect of the magnetic field strength

The dependency of the maximum growth rate with the strength of the magnetic field for all conductivity regimes is shown in Fig. 2.12 for $\chi_o = 10$, 2 and 0.1. In the good coupling case (top panel), increasing the strength of the magnetic field has little effect in the growth rate of the most unstable modes of all conductivity regimes until $v_A/c_s \sim 1$, where it drastically drops to zero. These results are similar to the ideal MHD case, which predicts that at this strength of the magnetic field the wavelength of most unstable modes become $\sim$ H, the scaleheight of the disc, and the perturbations are strongly damped.

In the $\chi_o = 2$ case shown in the middle panel, we found unstable modes in the Hall limit ($\sigma_1 B_z < 0$) for v_A/c_s up to 2.9. We know from the local analysis (W99) that once the local $\chi \leq 2$, unstable modes exist for every kv_A/Ω in this conductivity regime. As a result, even for suprathermal fields ($v_A/c_s > 1$), there are still unstable modes with $kH \lesssim 1$ growing within the disc.

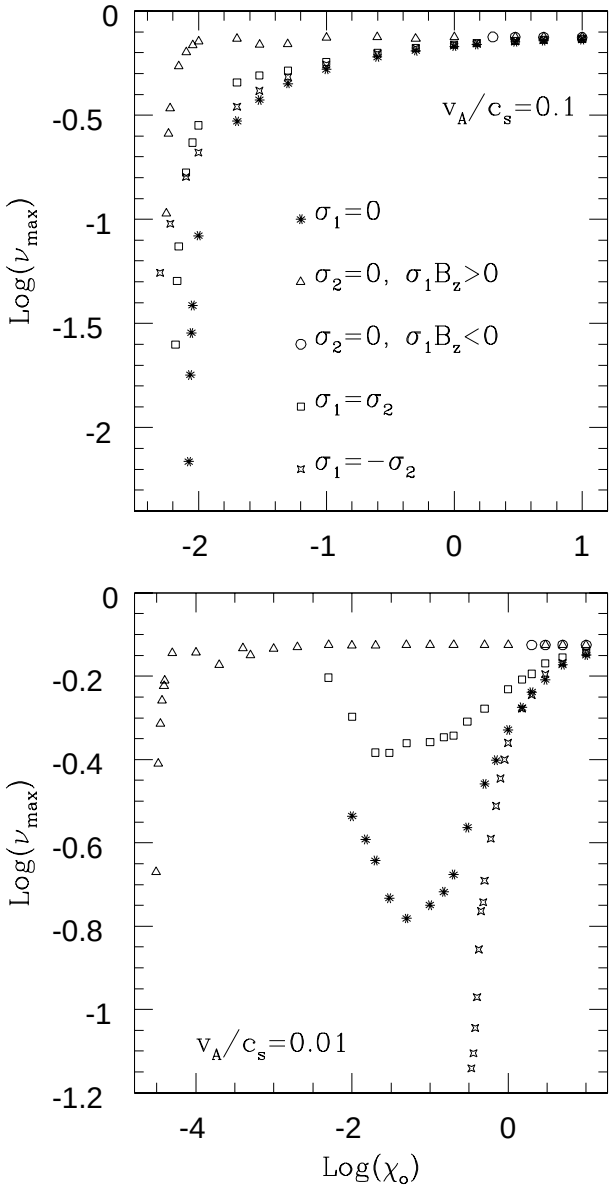

Figure 2.11 Growth rate of the fastest growing modes of the MRI as a function of χ_o for different conductivity regimes. $v_A/c_s = 0.1$ (top panel) and 0.01 (bottom panel).

Results for $\chi_o = 0.1$ (bottom panel) show clearly how ν_{max} plummets when $v_A/c_s \gtrsim \chi$ (ambipolar diffusion limit) or ${v_A}^2/{c_s}^2 \gtrsim \chi$ (Hall limit), as expected.

Finally, turning our attention to the dependency of the growth rate of the instability with the field strength at low v_A/c_s, we appreciate in all panels of Fig. 2.12 that ν_{max} initially increases as v_A/c_s is reduced, until it reaches a maximum. Further reductions in v_A/c_s cause the growth rate to diminish monotonically. Comparing these results with the findings of the local analysis (W99), we can show that the growth rates of global unstable modes at weak magnetic field strengths tend to the local values for the relevant coupling χ_o. This can be explained simply by the increase in wavenumber of unstable modes as v_A/c_s is reduced, which causes global effects (driven by stratification) to be less important. As a result, the growth of global modes does not differ significantly from the local values at the same coupling.

2.6 Discussion

The solutions presented in the previous sections illustrate the growth and structure of the MRI when different components of the conductivity tensor are dominant throughout the entire cross-section of the disc. Density stratification causes the local growth of unstable modes, and the amplitude of global perturbations, to be a function of height. The envelopes of short-wavelength solutions are shaped by this competition between different growth rates acting at different vertical locations. Moreover, when χ is weak at the midplane, long wavelength perturbations are important and vertical stratification is crucial in determining the growth of global MRI solutions. The results presented in this contribution confirm these expectations.

When the Hall and Pedersen components are comparable, the Hall effect alters the structure and growth of unstable perturbations for $\chi_o < v_A/c_s$. In this region of parameter space, ambipolar diffusion perturbations have negligible growth, but unstable modes that include Hall conductivity still grow at $\nu = 0.2 - 0.3$. Hall $\sigma_1 B_z > 0$ perturbations grow faster than $\sigma_1 B_z < 0$ ones. Furthermore, under a weak magnetic field ($v_A/c_s \lesssim 0.01$), the Hall effect significantly increases the growth rate of unstable modes at low coupling. When it dominates, unstable modes grow at close to the ideal rate for $\chi_o \sim 10^{-4}$.

The height above the midplane where the most unstable perturbations peak is dependent on the conductivity regime of the fluid. Consequently, the vertical location

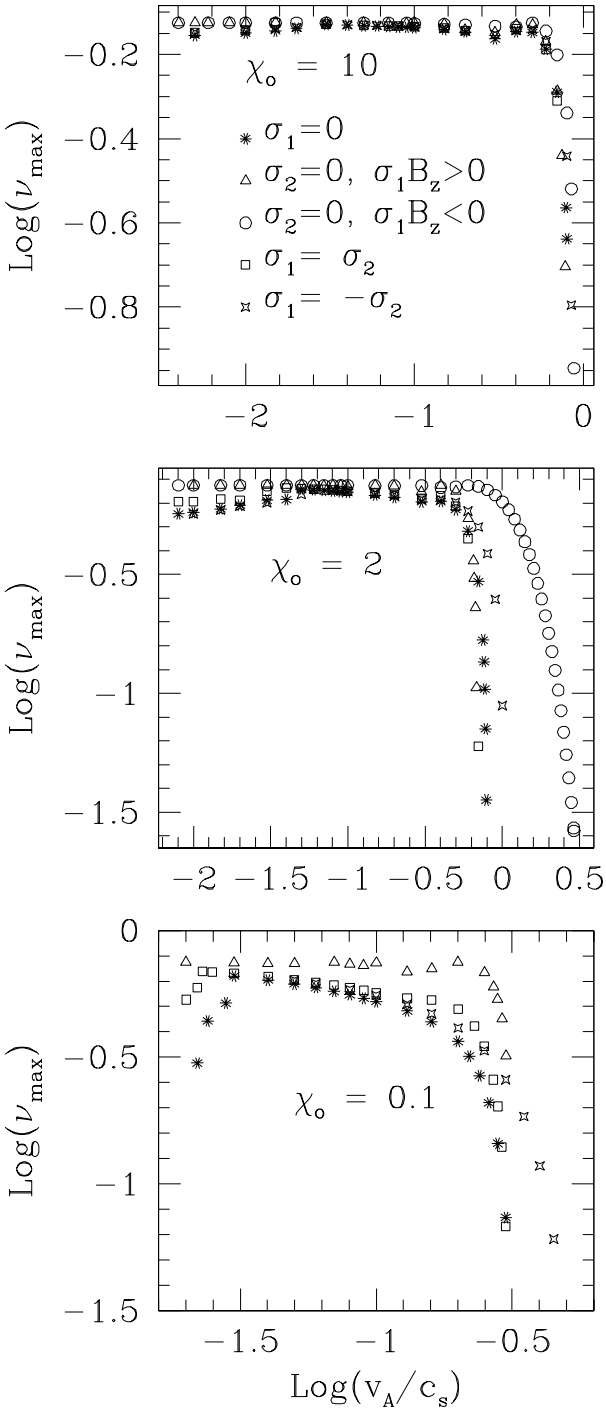

Figure 2.12 Growth rate of the fastest growing modes of the MRI as a function of v_A/c_s for different conductivity regimes. From top to bottom the coupling χ_o is 10, 2 and 0.1.

of the active zones within the disc, in which the MRI produces angular momentum transport and disc material is being accreted, is dependent on the configuration of the conductivity tensor. Perturbations including ambipolar diffusion peak consistently higher than those in both Hall limits. Also, for $\chi_o < v_A/c_s$, $\sigma_1 = \pm\sigma_2$ modes peak at different heights, signalling that the Hall effect is dependent on the orientation of the magnetic field with respect to the disc angular velocity vector $\mathbf{\Omega}$. In this region of parameter space, when $\sigma_1 B_z < 0$, modes peak at a higher z than when $\sigma_1 B_z > 0$. The Hall effect does not significantly modify the dependency of the height of maximum amplitude of unstable modes with the strength of the magnetic field for good coupling. In this region of parameter space ambipolar diffusion dominates and causes the perturbations to peak at higher z when v_A/c_s is reduced.

When $\sigma_1 B_z < 0$, Hall perturbations can have a very complex structure (high wavenumber), even at low coupling, and many modes are found to grow. In the non-linear stage, the interaction between these modes causes the MRI to develop into MHD turbulence with non-emergence of the typical two-channel flow obtained in other conductivity regimes (Sano & Stone 2002a, 2002b).

When does Hall diffusion determine the behaviour of the instability? Naively one might propose $|\sigma_1| \gtrsim \sigma_2$ as a criterion, but this ignores the level of coupling between the magnetic field and the gas. For example if $\chi \gtrsim 10$, ideal MHD almost holds and there is little dependence of growth rate and structure on the diffusion regime (see Fig. 2.3). A useful criterion can be derived using the results of the local analysis in W99 and comparing the maximum growth rates with and without Hall diffusion in the weak-coupling limit. In the absence of Hall diffusion (i.e. $\sigma_1 = 0$), the maximum growth rate for $\chi \lesssim 1$ is $3\chi/4$. When Hall diffusion is present and $\chi \lesssim |\sigma_1|/\sigma_\perp$, the maximum growth rate is either $\frac{3}{4}|\sigma_1|/(\sigma_\perp + \sigma_2)$ if $\sigma_1 B_z > 0$ or the instability is suppressed if $\sigma_1 B_z < 0$. In either case, Hall diffusion dominates the behaviour of the instability when

$$\chi \lesssim \chi_{\rm crit} = \frac{|\sigma_1|}{\sigma_\perp}\,. \tag{2.58}$$

Thus even when $|\sigma_1| \ll \sigma_2$, the structure and growth rate of the magnetorotational instability are dominated by Hall diffusion if $\chi < |\sigma_1|/\sigma_\perp$. This is easily satisfied, for example, for the nominal conditions at the disc midplane 1 AU from the central protostar (see Table 3.1), where $|\sigma_1|/\sigma_\perp \approx |\beta_e| = 0.035$ (using eqs. 2.18 and 2.20

with $|\beta_e| \gg 1$) and $\chi = 9 \times 10^{-6}$. At 5 AU, $\chi \approx 2$ and $\sigma_1 \gg \sigma_2$, so Hall diffusion dominates here also. Although these results depend on the assumed magnetic field strength, the conditions under which $\chi < \chi_{\rm crit}$ are so broad that we can conclude that Hall diffusion determines the growth rate and structure of the instability over a large range of radii.

Despite this, Hall diffusion has generally been neglected in studies of accretion discs in favour of the ambipolar diffusion or resistive limits. Here we illustrate the severity of this approximation by comparing the structure and growth rate of the unstable perturbations for a model with $\sigma_1 = \sigma_2$ to those for 'simplified' pure ambipolar/resistive diffusion and Hall ($\sigma_1 B_z > 0$) models obtained by setting σ_2 or σ_1 to zero respectively and reducing the coupling parameter χ_o by a factor of $\sqrt{2}$ to reflect its dependence on $({\sigma_1}^2 + {\sigma_2}^2)^{1/2}$ (see eq. 2.50). The full model has $v_A/c_s = 0.01$ and $\chi_o = 0.01414$, whereas the the corresponding ambipolar diffusion and Hall limits have $\chi_o = v_A/c_s = 0.01$ and the appropriate values of σ_1 and σ_2 as per Table 2.3.

The comparison is presented in Fig. 2.13. The structure and growth rate of pure ambipolar diffusion and Hall ($\sigma_1 B_z > 0$) perturbations are as expected for $\chi_o \approx v_A/c_s$, with the ambipolar diffusion decaying towards the midplane and the envelope of the pure-Hall solutions being fairly constant. In both the ambipolar diffusion and the $\sigma_1 = \sigma_2$ cases we obtain a magnetic 'dead zone' near the midplane where no perturbations grow (Gammie 1996, Wardle 1997). Comparing the top panel of Fig. 2.13 with the middle and bottom ones it is clear that the Hall effect modifies both the structure and growth of unstable modes. In particular, the extent of the dead zone is reduced and the growth rate is increased. According to these results, both the depth of the active zones within the disc and the rate of angular momentum transport by unstable modes can be significantly modified by the Hall effect.

Although our solutions incorporate the effect of density stratification on the coupling parameter and the Alfven speed, we have assumed that the components of the conductivity tensor do not vary with height. While this simplification permitted us to compare the behaviour of the instability in different regimes, the conductivities in a real disc will reflect the height-dependence of charged particle abundances and their Hall parameters (see §2.2.1). Different regimes are expected to dominate at different heights (Wardle 2003).

Nonetheless, it is clear from the simplified comparison presented here that Hall diffusion is an essential part of accretion in low-conductivity discs, and that it determines the extent of the magnetically-inactive 'dead zone' (Gammie 1996, Wardle 1997). Further, Hall diffusion will modify any angular momentum transport within the dead zone that occurs via non-axisymmetric density waves driven by the active surface layers (Stone & Fleming 2003) because it will dominate the marginally magnetically-active regions of the disc just above the dead zone. Hall diffusion may therefore affect the ability of dust grains to settle towards the midplane and begin to assemble into planetesimals (e.g. Weidenschilling & Cuzzi 1993).

2.7 Summary

In this chapter we have examined the structure and linear growth of the magnetorotational instability (MRI) in weakly ionised, stratified accretion discs, assuming an initially vertical magnetic field. This work is relevant for the study of low-conductivity accretion systems, such as protostellar and quiescent dwarf novae discs, where non-ideal MHD effects are important (Gammie & Menou 1998; Menou 2000; Stone et al. 2000). The formulation allows for a height-dependent conductivity but in this initial study we assumed the components of the conductivity tensor were constant with height. The analysis was restricted to perturbations with a vertical wavevector ($k = k_z$), which are the most unstable modes when initiated from a vertically aligned magnetic field (Balbus & Hawley 1991; Sano & Miyama 1999). In this case, the field-parallel component of the conductivity tensor plays no role and the ambipolar diffusion and resistive limits are identical. The linearised system of ODE was integrated from the midplane to the surface of the disc under appropriate boundary conditions and global unstable modes were obtained. The parameters that control the evolution of the fluid are: (*i*) The coupling between ionised and neutral components of the fluid evaluated at the midplane (χ_o), which relates the frequency at which non-ideal effects are important with the dynamical (Keplerian) frequency of the disc; (*ii*) the magnetic field strength characterised by the ratio v_A/c_s at the midplane; and (*iii*) the ratio of the components of the conductivity tensor perpendicular to the magnetic field σ_1/σ_2.

In order to explore the growth and structure of unstable modes when different conductivity regimes dominate over the entire cross-section of the disc, we exam-

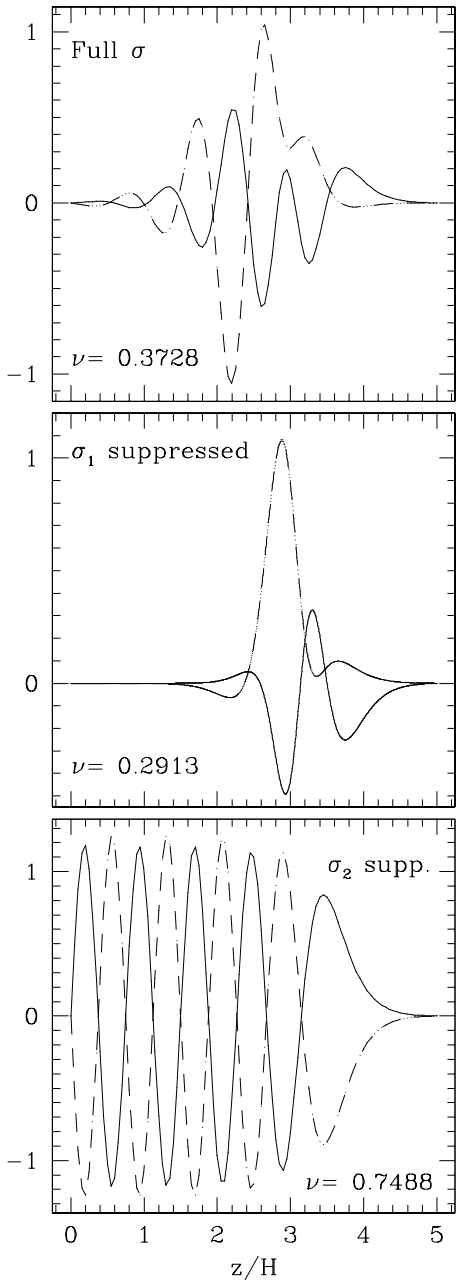

Figure 2.13 Comparison of the structure and growth rate of the MRI for different configurations of the conductivity tensor for $v_A/c_s = 0.01$. Top panel shows the case where both ambipolar diffusion and Hall ($\sigma_1 B_z > 0$) conductivity terms are important. In this configuration the Hall regime is dominant close to the midplane and ambipolar diffusion dominates near the surface. Middle and bottom panels show the instability under the ambipolar diffusion and Hall approximations, respectively.

ined the following configurations of the conductivity tensor: $\sigma_1 = 0$ (the ambipolar diffusion or resistive limits), $\sigma_2 = 0$ (both Hall limits $\sigma_1 B_z > 0$ and $\sigma_1 B_z < 0$), and the cases where both effects are important ($\sigma_1 = \pm\sigma_2$).

The main results of this study are highlighted below:

1. Global modes are a discrete subset from the continuous curve of possible ν vs. k combinations obtained with a local analysis (W99). These unstable modes can be expressed as a superposition of two WKB modes with similar growth rate, which explains the interference patterns found in some of the perturbations.

2. Ambipolar diffusion perturbations peak consistently higher above the midplane than solutions where Hall conductivity dominates.

3. For good coupling ($\chi_o > v_A/c_s$), the structure and growth of the perturbations are mainly determined by ambipolar diffusion. For a weaker coupling, Hall conductivity significantly modifies unstable modes. In this case, $\sigma_1 = \sigma_2$ perturbations resemble the Hall $\sigma_1 B_z > 0$ limit and peak closer to the midplane while $\sigma_1 = -\sigma_2$ modes have their maximum amplitude closer to the surface.

4. Hall limit ($\sigma_1 B_z < 0$) perturbations can have a complex structure (high wavenumber) even for poor coupling ($\chi_o = 2$). There are also many unstable modes, which supports findings that in this case the MRI evolves into MHD turbulence with non-emergence of the two-channel flow obtained in other regimes (Sano & Stone 2002a, 2002b).

5. As the coupling parameter χ_o is reduced, departure from ideal growth $\nu \sim 0.75$ occurs at a rate that depends on the conductivity regime. Hall limit perturbations grow at close to the ideal limit for $\chi_o > {v_A}^2/{c_s}^2$. In the ambipolar diffusion approximation the growth rate decreases when $\chi_o \lesssim v_A/c_s$. These results are in agreement with predictions from W99.

6. The weaker the magnetic field the higher the perturbations peak in all regimes where ambipolar diffusion is present. On the contrary, both Hall limits peak closer to the surface with weaker v_A/c_s.

7. Unstable modes grow when v_A/c_s is increased until a critical value $v_A/c_{s_{crit}}$ is reached. At the critical v_A/c_s the growth rate abruptly drops to zero. At good coupling $v_A/c_{s_{crit}} \sim 1$ for all conductivity regimes. At the poor coupling

limit ($\chi_o = 2$), results are different only for the Hall regime ($\sigma_1 B_z < 0$). In this case we obtain unstable modes for $v_A/c_s \sim 2.9$.

8. At very weak magnetic fields ($v_A/c_s \lesssim 0.01$), global effects are less important, due to the high wavenumber of the perturbations. In this region of parameter space the growth rates of MRI perturbations tend to the corresponding local values for the relevant fluid parameters.

9. Hall difussion determines the growth of the MRI when $\chi \lesssim |\sigma_1|/\sigma_\perp$. This condition is satisfied over a large range of radii in protostellar discs.

10. When the Hall regime dominates near the midplane and ambipolar diffusion is dominant closer to the surface, a larger section of the disc is unstable to MRI perturbations and unstable modes grow faster than those obtained using the ambipolar diffusion approximation

Chapter 3

The instability in protoplanetary discs

3.1 Introduction

The magnetorotational instability (MRI; Balbus & Hawley 1991, 1998; Hawley & Balbus 1991) generates and sustains angular momentum transport in differentially rotating astrophysical discs. It does so by converting the free energy source contributed by differential rotation into turbulent motions (e.g. Balbus 2003), which transport angular momentum via Maxwell stresses.

Most MRI models in non-ideal MHD conditions adopt either the ambipolar diffusion (Blaes & Balbus 1994, MacLow et al. 1995 and Hawley & Stone 1998) or resistive approximations (Jin 1996, Balbus & Hawley 1998, Papaloizou & Terquem 1997, Sano & Miyama 1999; Sano, Inutsuka & Miyama 1998, Sano et. al. 2000, Fleming, Stone & Hawley 2000 and Stone & Fleming 2003). The inclusion of Hall diffusion is a relatively recent development (Wardle 1999 (W99 hereafter), Balbus & Terquem 2001, Sano & Stone 2002a,b; 2003, Salmeron & Wardle 2003 (SW03 hereafter) and Desch 2004). When the Hall effect dominates over ambipolar diffusion, fluid dynamics is dependent on the alignment of the magnetic field with the angular velocity vector of the disc (Wardle & Ng 1999), and wave modes supported by the fluid are intrinsically modified. For example, left and right-circularly polarised Alfven waves travel at different speeds and damp at different rates in this regime (Pilipp et al. 1987, Wardle & Ng 1999). Both the structure and growth rate

of MRI perturbations can be substantially modified by Hall conductivity, especially when the coupling between ionised and neutral components of the fluid is low (W99, SW03).

In a previous paper we presented a linear analysis of the vertical structure and growth of the MRI in weakly ionised, stratified accretion discs (SW03). In that study the components of the conductivity tensor were assumed to be constant with height. The obtained solutions illustrate the properties of the MRI when different conductivity regimes are dominant over the entire cross-section of the disc. We found that when the magnetic coupling is weak, modes computed with a non-zero Hall conductivity grow faster and act over a more extended cross-section than those obtained using the ambipolar diffusion approximation. The height above the midplane where the fastest growing modes peak depends on the conductivity regime of the fluid. When ambipolar diffusion is important, perturbations peak at a higher z than when the fluid is in the Hall limit. Furthermore, when the coupling is weak, perturbations computed with a full conductivity tensor peak at different heights depending on the orientation of the magnetic field with respect to the angular velocity vector of the disc. This is a consequence of the dependency of the Hall effect on the sign of $(\mathbf{k}\cdot\mathbf{\Omega})(\mathbf{k}\cdot\mathbf{B})$ (Balbus & Terquem 2001), which reduces to $\mathbf{\Omega}\cdot\mathbf{B}$ for vertical fields and wavenumbers (W99). Finally, we showed that in the Hall regime perturbations can have a very complex structure (high wavenumber), particularly when the magnetic field is weak. In these conditions, many modes were found to grow, even with a very weak magnetic coupling. These results suggest that significant accretion can occur in regions closer to the midplane of astrophysical discs, despite the low magnetic coupling, due to the large column density of the fluid. This idea contrasts with the commonly accepted view that accretion is important primarily in the surface regions, where the coupling between ionised and neutral components of the fluid is much stronger, but the column density is significantly smaller.

In a real disc, the components of the conductivity tensor vary with height (e.g. Wardle 2003) as a result of changes in the abundances of charged particles, fluid density and magnetic field strength. This, in turn, is a consequence of changes in the ionisation balance within the disc, which reflects the equilibrium between ionisation and recombination processes. The former are primarily non-thermal, triggered by cosmic rays, x-rays emitted by the central protostar and radioactive materials. The later can, in general, occur both in the gas phase and on grain surfaces (e.g. Oppen-

heimer & Dalgarno 1974, Spitzer 1978, Umebayashi & Nakano 1980, Nishi, Nakano & Umebayashi 1991, Sano et. al. 2000). As a result, different conductivity regimes are expected to dominate at different heights (Wardle 2003). In this paper we revisit the linear growth and structure of MRI perturbations using a height-dependent conductivity tensor. We assume that the disc is thin and isothermal and adopt a fiducial disc model based in the minimum-mass solar nebula (Hayashi 1981, Hayashi, Nakazawa & Nakagawa 1985). Further, we assume that ions and electrons are the main charge carriers, which is a valid approximation in late stages of accretion, after dust grains have settled towards the midplane of the disc. As an indication of the timescales for this settling to occur, Nakagawa, Nakazawa & Hayashi (1981) show that the mass fraction of ~ 1 - $10\,\mu$m grains well mixed with the gas phase, (i.e. not settled), drops from $\sim 10^{-1}$ to 10^{-4} in t $\sim 2 \times 10^3$ to 1×10^5 years. Furthermore, although the timescale for dust settling all the way to the equator may exceed the lifetime of the disc, grains can settle within a few pressure scaleheights about the midplane in a much shorter timescale (Dullemond & Dominik 2004).

This paper is structured as follows: Section 3.2 summarises the formulation, including the governing equations, fiducial disc model and ionisation balance. Section 3.3 describes the linearisation, parameters of the problem and boundary conditions. Results are presented in sections 3.4 and 3.5. We summarise in section 3.4 the test models used in this study and present the ionisation rates as a function of z at representative radial locations from the central protostar ($R = 1$, 5 and 10 AU). The importance of different conductivity regimes at different heights is also described for a range of magnetic field strengths. Then, in section 3.5, the structure and growth rate of MRI perturbations at the radii of interest are analysed, including a comparison with results obtained using different configurations of the conductivity tensor, sources of ionisation and disc structure. We find that the MRI is active over a wide range of fluid conditions and magnetic field strengths. For example, for the fiducial model at $R = 1$ AU, and including cosmic ray ionisation, unstable modes are found for $B \lesssim 8$ G. When 200 mG $\lesssim B \lesssim 5$ G, these perturbations grow at about the ideal-MHD rate ~ 0.75 times the dynamical (Keplerian) frequency of the disc. Results are discussed in section 3.6 and the paper's formulation and key findings are summarised in section 3.7.

3.2 Formulation

3.2.1 Governing Equations

Following W99 and references therein, we formulate the conservation equations about a local Keplerian frame corotating with the disc at the Keplerian frequency $\Omega = \sqrt{GM/r^3}$. Time derivatives in this frame, $\partial/\partial t$, correspond to $\partial/\partial t + \Omega\partial/\partial\phi$ in the standard laboratory system (r, ϕ, z) anchored at the central mass M. The fluid velocity is expressed as a departure from Keplerian motion $\mathbf{v} = \mathbf{V} - \mathbf{v}_K$, where $\mathbf{V}$ is the velocity in the laboratory frame and $\mathbf{v}_K = \sqrt{GM/r}\ \hat{\phi}$ is the Keplerian velocity at the radius r. The fluid is assumed to be weakly ionised, so the effect of ionisation and recombination processes on the neutral gas, as well as the ionised species' inertia and thermal pressure, are negligible. Under this approximation, separate equations of motion for the ionised species are not required and their effect on the neutrals is treated via a conductivity tensor (W99 and references therein), which is a function of location (r,z).

The governing equations are the continuity equation,

$$\frac{\partial \rho}{\partial t} + \nabla \cdot (\rho \mathbf{v}) = 0\,, \tag{3.1}$$

the equation of motion,

$$\frac{\partial \mathbf{v}}{\partial t} + (\mathbf{v}\cdot\nabla)\mathbf{v} - 2\Omega v_\phi \hat{\mathbf{r}} + \tfrac{1}{2}\Omega v_r \hat{\phi} - \frac{v_K^2}{r}\hat{\mathbf{r}} + \frac{c_s^2}{\rho}\nabla\rho + \nabla\Phi - \frac{\mathbf{J}\times\mathbf{B}}{c\rho} = 0\,, \tag{3.2}$$

and the induction equation,

$$\frac{\partial \mathbf{B}}{\partial t} = \nabla\times(\mathbf{v}\times\mathbf{B}) - c\nabla\times\mathbf{E}' - \tfrac{3}{2}\Omega \mathbf{B}_r \hat{\phi}\,. \tag{3.3}$$

In the equation of motion (3.2), Φ is the gravitational potential of the central object, given by

$$\Phi = -\frac{GM}{(r^2+z^2)^{\frac{1}{2}}}\,, \tag{3.4}$$

and v_K^2/r is the centripetal term generated by exact Keplerian motion. Similarly, $2\Omega v_\phi \hat{\mathbf{r}}$ and $\frac{1}{2}\Omega v_r \hat{\phi}$ are the coriolis terms associated with the use of a local Keplerian frame, $c_s = \sqrt{P/\rho}$ is the isothermal sound speed, $\Omega = v_K/r$ is the Keplerian frequency and c is the speed of light. Other symbols have their usual meanings.

In the induction equation (3.3), $\mathbf{E}'$ is the electric field in the frame comoving with the neutrals and the term $\frac{3}{2}\Omega \mathbf{B}_r \hat{\phi}$ accounts for the generation of toroidal field from the radial component due to the differential rotation of the disc.

Additionally, the magnetic field must satisfy the constraint:

$$\nabla \cdot \mathbf{B} = 0\,, \tag{3.5}$$

and the current density must satisfy Ampere's law,

$$\mathbf{J} = \frac{c}{4\pi} \nabla \times \mathbf{B} \tag{3.6}$$

and Ohm's law,

$$\mathbf{J} = \sigma \cdot \mathbf{E}' = \sigma_\parallel \mathbf{E}'_\parallel + \sigma_1 \hat{\mathbf{B}} \times \mathbf{E}'_\perp + \sigma_2 \mathbf{E}'_\perp\,. \tag{3.7}$$

Note that we have introduced the conductivity tensor σ in equation (3.7). We refer the reader to W99 and references therein for derivations and additional details of this formulation. Assuming that the only charged species are ions and electrons, and that charge neutrality is satisfied ($n_i = n_e$), the components of the conductivity tensor can be expressed as (SW03), the conductivity parallel to the magnetic field,

$$\sigma_\parallel = \frac{cen_e}{B}(\beta_i - \beta_e)\,, \tag{3.8}$$

the Hall conductivity,

$$\sigma_1 = \frac{cen_e}{B} \frac{(\beta_i + \beta_e)(\beta_e - \beta_i)}{(1+\beta_e^2)(1+\beta_i^2)}\,, \tag{3.9}$$

and the Pedersen conductivity,

$$\sigma_2 = \frac{cen_e}{B} \frac{(1 - \beta_i\beta_e)(\beta_i - \beta_e)}{(1+\beta_e^2)(1+\beta_i^2)}\,. \tag{3.10}$$

From (3.9) and (3.10), we find:

$$\sigma_\perp = \frac{cen_e}{B} \frac{(\beta_i - \beta_e)}{[(1+\beta_e^2)(1+\beta_i^2)]^{1/2}}\,. \tag{3.11}$$

where $\sigma_\perp = \sqrt{\sigma_1^2 + \sigma_2^2}$ is the total conductivity perpendicular to the magnetic field.

In equations (3.8) to (3.11),

$$\beta_j = \frac{Z_j e B}{m_j c} \frac{1}{\gamma_j \rho} \tag{3.12}$$

is the Hall parameter, given by the ratio of the gyrofrequency and the collision frequency of charged species j with the neutrals. It represents the relative importance of the Lorentz and drag terms in the charged species' motion. In equation (3.12),

$$\gamma_j = \frac{< \sigma v >_j}{m_j + m}\,, \tag{3.13}$$

where m is the mean mass of the neutral particles and $< \sigma v >_j$ is the rate coefficient of momentum exchange by collisions with the neutrals. The ion-neutral momentum rate coefficient is given by,

$$< \sigma v >_i = 1.6 \times 10^{-9}\,\mathrm{cm^3\,s^{-1}}\,, \tag{3.14}$$

an expression that ignores differences in the values of elastic cross-sections of H, H_2 and H_e (Draine, Roberge & Dalgarno 1983). Similarly, the rate coefficient of momentum exchange of electrons with the neutrals is (Draine et al. 1983):

$$< \sigma v >_e \approx 1 \times 10^{-15}\,\mathrm{cm^2} \left(\frac{128 k T}{9\pi m_e}\right)^{1/2}\,, \tag{3.15}$$

and the mean ion mass $m_i = 30 m_H$.

The relative magnitudes of the components of the conductivity tensor differentiate three conductivity regimes: When $\sigma_\parallel \gg \sigma_2 \gg |\sigma_1|$ for most charged species, ambipolar diffusion dominates and the magnetic field is effectively frozen into the ionised components of the fluid. Electron-ion drift is small compared with ion-neutral drift and the ionised species act as a single fluid. MRI studies in this regime include Blaes & Balbus (1994), MacLow et al. (1995) and Hawley & Stone (1998). Conversely, when $\sigma_\parallel \approx \sigma_2 \gg |\sigma_1|$, the conductivity is a scalar, giving rise to the familiar ohmic diffusion, and the magnetic field is no longer frozen into any fluid component. Examples of studies of the MRI in this regime are Jin (1996), Balbus & Hawley (1998), Papaloizou & Terquem (1997), Sano & Miyama (1999), Sano et. al. (1998, 2000, 2004), Fleming, Stone & Hawley (2000) and Stone & Fleming, (2003). Ambipolar diffusion dominates in low density regions, where magnetic stresses are

more important than collisions with the neutrals and the ionised species are mainly tied to the magnetic field rather than to the neutral particles. On the contrary, in relatively high density environments, the ionised species are primarily linked to the neutrals via collisions and Ohmic diffusion dominates. There is, however, an intermediate density range characterised by a varying degree of coupling amongst charged species. In these circumstances, there is a component of the conductivity tensor that is perpendicular both to the electric and magnetic fields. It is this term that gives rise to Hall currents. It has been shown that this regime can be important in the weakly ionised environment of accretion discs. For example, using an MRN grain model (Mathis, Rumpl & Nordsieck 1977) with a power law distribution of grain sizes between 50 and 2500 Angstrom, Wardle & Ng (1999) showed that Hall conductivity is important for $10^7 \lesssim n_H \lesssim 10^{11}\,\mathrm{cm}^{-3}$. MRI studies including Hall diffusion have been conducted by W99, Balbus & Terquem (2001), Sano & Stone (2002a,b; 2003), SW03 and Desch (2004).

The ionisation balance within the disc (section 3.2.3) determines the abundances of charged species (ions and electrons). These, in turn, determine the configuration of the conductivity tensor. In protostellar discs, outside of the central 0.1 AU, ionisation sources are non-thermal (Hayashi 1981) and the ionisation fraction is not enough to produce good magnetic coupling over the entire cross-section of the disc. In these conditions, the region around the midplane is likely to be a magnetically "dead zone" (Gammie 1996).

3.2.2 Disc Model

Our model incorporates the vertical structure of the disc, but neglects fluid gradients in the radial direction. This is an appropriate approximation, as astrophysical accretion discs are generally thin and changes in the radial direction occur on a much bigger length scale than those in the vertical direction. Including the vertical structure means that perturbations of spatial dimensions comparable to the scale height of the disc, which are associated with either a strong magnetic field ($v_A \sim c_s$) or low conductivity, can be explored.

We adopted, as our fiducial model, a disc based in the minimum-mass solar nebula (Hayashi 1981, Hayashi et. al. 1985). In this model, the surface density $\Sigma(r)$, sound speed $c_s(r)$, midplane density $\rho_o(r)$, scaleheight $H(r)$ and temperature

$T(r)$ are:

$$\Sigma(r) = \Sigma_o \left(\frac{r}{1AU}\right)^{-\frac{3}{2}} , \tag{3.16}$$

$$c_s(r) = c_{so} \left(\frac{r}{1AU}\right)^{-\frac{1}{4}} \left(\frac{L_\star}{L_\odot}\right)^{\frac{1}{8}} \left(\frac{2.34}{\mu}\right)^{\frac{1}{2}} , \tag{3.17}$$

$$\rho_0(r) = \rho_o \left(\frac{r}{1AU}\right)^{-\frac{11}{4}} \left(\frac{L_\star}{L_\odot}\right)^{-\frac{1}{8}} \left(\frac{M_\star}{M_\odot}\right)^{\frac{1}{2}} \left(\frac{2.34}{\mu}\right)^{\frac{1}{2}} , \tag{3.18}$$

$$H(r) = H_0 \left(\frac{r}{1AU}\right)^{1.25} , \tag{3.19}$$

and,

$$T(r) = T_o \left(\frac{r}{1AU}\right)^{-1/2} \left(\frac{L_\star}{L_\odot}\right)^{1/4} . \tag{3.20}$$

In the previous expressions,

$$\Sigma_o = 1.7 \times 10^3 \,\mathrm{g\,cm^{-2}} , \tag{3.21}$$

$$c_{so} = 9.9 \times 10^4 \,\mathrm{cm\ s^{-1}} , \tag{3.22}$$

$$\rho_o = 1.4 \times 10^{-9} \,\mathrm{g\ cm^{-3}} , \tag{3.23}$$

$$H_0 = 5.0 \times 10^{11} \,\mathrm{cm} , \tag{3.24}$$

and,

$$T_o = 280 \,\mathrm{K} . \tag{3.25}$$

In equations (3.16) to (3.20), $M_\star$ and $L_\star$ are the stellar mass and luminosity, respectively, and μ is the mean molecular mass of the gas. This model describes the minimum mass distribution of the solar nebula, estimated assuming an efficient planet formation with no significant migration. With these assumptions, the current mass distribution and composition of the planets is a good indication of that of dust in the original nebula. This model has been used extensively, but there are

theoretical grounds to expect that a typical protostellar disc may be more massive, with a different large scale structure, shaped ultimately by the action of MHD turbulence (e.g. Balbus & Papaloizou 1999). Furthermore, disc masses of up to $0.1M_{\odot}$, associated with surface density distributions following a power-law of index p between 0 and 1, have been derived for T Tauri stars in Taurus (Kitamura et. al. 2002). It can be shown that the disc surface density may be roughly up to an order of magnitude higher than the one specified by the minimum-mass solar nebula model before self gravity becomes important. To account for the possibility of discs being more massive than the minimum-mass solar nebula model, we also studied the properties of MRI unstable modes using a disc structure with an increased surface density $\Sigma_o^{'} = 10\Sigma_o$ and mass density $\rho_o^{'} = 10\rho_o$. The Toomre parameter (Toomre 1964) $Q \sim 6$ in this case, so the assumption of a non self-gravitating disc is still valid. For simplicity, we assume that the temperature T_o is unchanged, so H_o and c_{so} are the same as in the fiducial model.

As the disc is gravitationally stable, the gravitational force in the vertical direction comes from the central protostar. Under these conditions, the balance between the vertical component of the central gravitational force and the pressure gradient within the disc determines its equilibrium structure. The vertical density distribution in hydrostatic equilibrium is given by

$$\frac{\rho(r,z)}{\rho_o(r)} = \exp\left[-\frac{z^2}{2H^2(r)}\right] . \tag{3.26}$$

Assuming a neutral gas composed of molecular hydrogen and helium such that $n_{He} = 0.2n_{H_2}$, the neutral gas mass and number densities are, respectively,

$$\rho = \Sigma n_i m_i = 1.4 m_H n_H \tag{3.27}$$

and

$$n = 1.2 n_{H_2} , \tag{3.28}$$

which gives,

$$n_H(r,z) = \frac{\rho(r,z)}{1.4 m_H} \tag{3.29}$$

and $\mu = \rho/n = 2.34$. For simplicity, we take $L_{\star}/L_{\odot} = M_{\star}/M_{\odot} = 1$ in all our models.

3.2.3 Ionisation balance

The ionisation balance within the disc is given by the equilibrium between ionisation and recombination processes. In general, recombination can take place both in the gas phase and on grain surfaces (e.g. Oppenheimer & Dalgarno 1974, Spitzer 1978, Umebayashi & Nakano 1980, Nishi, Nakano & Umebayashi 1991, Sano et. al. 2000), but here we have assumed that grains have settled, so we are including only gas-phase recombination rates. Except in the innermost sections of the disc ($R \lesssim 0.1$ AU), where thermal effects are important (Hayashi 1981), ionisation processes in protostellar discs are mainly non-thermal. Ionising agents are typically cosmic rays, x-rays emitted by the magnetically active protostar, and the decay of radioactive materials present within the disc. Some authors (e.g. Fromang, Terquem & Balbus 2002) have argued that the low energy particles important for cosmic-ray ionisation are likely to be excluded by the protostar's winds. Given the uncertainties involved, and the expectation that cosmic rays (if present), may be more important than x-rays near the midplane (especially for $R \approx 1$ AU, where the surface density is larger than the attenuation length of x-rays), we explore both options in this study. The treatment of ionisation and recombination processes is detailed below.

Cosmic ray ionisation

The cosmic ray ionisation rate, $\zeta_{CR}(r,z)$, is given by,

$$\zeta_{CR}(r,z) = \frac{\zeta_{CR}}{2}\left[\exp\left(-\frac{\Sigma(r,z)}{\lambda_{CR}}\right) + \exp\left(-\frac{\Sigma(r)-\Sigma(r,z)}{\lambda_{CR}}\right)\right], \tag{3.30}$$

where $\zeta_{CR} = 10^{-17}\,\mathrm{s}^{-1}$ is the ionisation rate due to cosmic rays in the interstellar medium and $\lambda_{CR} = 96$ gr cm^{-2} is the attenuation length, a measure of how deep cosmic rays can penetrate the disc (Umebayashi & Nakano 1981). When the surface density is larger than $\sim 2\lambda_{CR}$, most cosmic rays do not reach the midplane. Also,

$$\Sigma(r,z) = \int_z^\infty \rho(r,z)dz\,, \tag{3.31}$$

is the vertical column density from the location of interest to infinity. The two terms in brackets in equation (3.30) measure the ionisation rate at the position (r, z) by

cosmic rays penetrating the disc from above, and below, respectively.

X-ray ionisation

There is strong evidence for an enhanced magnetic activity in young stellar objects (i.e. see review by Glassgold, Feigelson & Montmerle 2000). Typical soft x-ray luminosities (0.2 - 2 kev) of these objects are in the range of 10^{28} - 10^{30}erg s^{-1}, about 10^2 - 10^3 times more energetic than solar levels (Glassgold et. al. 2000). Models of the penetration of stellar x-rays into a protostellar disc by Igea & Glassgold (1999), show that even discounting the low energy photons that are attenuated by stellar winds, the ionisation rate due to hard x-rays close to the central object is many orders of magnitude larger than that of cosmic rays, especially above $z/H \sim 2$. These authors investigated the ionisation rate by x-rays from a central protostar modelled as a x-ray source of total luminosity $L_x \sim 10^{29}$erg s^{-1} and temperature kT_x in the range of 3 - 8 kev. The transport of x-rays through the disc was followed using a Monte Carlo procedure which included both absorption and scattering by disc material. The incorporation of scattering is important, as x-rays can be scattered not only out of the disc, but also towards the midplane, enhancing the ionisation level deeper within the disc. Results indicate that, at each radius, the x-ray ionisation rate is a function of the vertical column density into the disc $N_\perp(r,z)$, irrespective of its structural details.

To calculate the x-ray ionisation rate $\zeta_X(r,z)$ in the upper half of the disc we added the contribution of x-rays arriving from both sides. We used the values of $\zeta_X(r,z)$ (s^{-1}) as a function of the vertical column density, $N_\perp$ (cm^{-2}), plotted in Fig. 3 of Igea & Glassgold (1999), for $R = 1$, 5 and 10 AU and $kT_x = 5$ Kev. The vertical column density, appropriate for x-rays arriving from the top is

$$N_\perp(r,z) = \int_z^\infty n_H(r,z)dz\,, \tag{3.32}$$

with n_H given by equation (3.29). Similarly, the ionisation contributed by x-rays arriving at $(r, z > 0)$ from the other hemisphere of the disc is obtained substituting $N_\perp$ above by $2N_\perp(r,0) - N_\perp(r,z)$, although this contribution is usually negligible.

Radioactivity

The ionisation rate ζ_R contributed by the decay of radioactive materials (primarily ^{40}K) have also been considered in previous work (i.e. Consolmagno & Jokipii 1978, Sano et al. 2000). This rate can be calculated as (Consolmagno & Jokipii 1978):

$$\zeta_R = \frac{\gamma n_r E}{\Delta\varepsilon}\,, \tag{3.33}$$

where γ (s^{-1}) is the decay rate of the radioactive isotopes, n_r their number density relative to hydrogen, and E (eV) the energy of the produced radiation. Similarly, $\Delta\varepsilon = 37$ eV is the average energy for the production of an ion pair in H_2 gas (Consolmagno & Jokippi 1978 and references therein, Shull & Van Steenburg 1985, Voit 1991). In the present study we have adopted,

$$\zeta_R = 6.9 \times 10^{-23}[\delta_2 + (1-\delta_2) f_g]\ \mathrm{s}^{-1} \tag{3.34}$$

(Umebayashi & Nakano 1981, 1990). Here, $\delta_2 \approx 0.02$ is the fraction of heavy metal atoms in the gas phase, estimated via measurements of interstellar absorption lines in diffuse clouds (Morton 1974). It is, of course, possible that δ_2 in discs could be even smaller than this value. On the other hand, f_g is a parameter that takes into account the degree of sedimentation of dust grains in protostellar discs with respect to interstellar values (Hayashi 1981, Sano et. al. 2000).

Although the ionisation effect contributed by this agent is very small compared with that of x-rays and cosmic rays, we included it because it may well be the only mechanism active in regions close to the midplane (particularly for $R \lesssim 5$ AU) in the scenario where cosmic rays are excluded from the disc. In this case, it is important to explore the sensitivity of MRI perturbations to changes in the level of depletion of dust grains (f_g).

We have assumed here that the ionised component of the fluid is made of ions and electrons only, a case that corresponds to late evolutionary stages of protostellar discs, after dust grains have settled towards the midplane. Accordingly, we assume $f_g = 0$ in all our models, except when specifically exploring the role of radioactivity in a disc where cosmic rays are assumed to be excluded from it.

Recombination rate

Gas-phase recombination occurs through dissociative recombination of electrons with molecular ions and, at a slower rate, via radiative recombination with metal ions. It has been pointed out by previous authors that the ionisation balance may be especially sensitive to the presence of metal atoms within the disc. For some disc configurations, a number density of metals as small as 10^{-7} times the cosmic abundance may be enough to make the whole cross-section of the disc turbulent, eliminating the central magnetic dead zone (Fromang et. al. 2002). This is so because metal atoms generally take the charges of molecular ions, but recombine with electrons (via radiative processes) at a much slower rate.

If n_m^+ and n_M^+ are the number densities of molecular and metal ions, respectively, the rate equations for n_e and n_m^+ can be expressed as (e.g. Fromang et. al. 2002):

$$\frac{dn_e}{dt} = \zeta n_H - \beta n_e n_m^+ - \beta_r n_e n_M^+ \tag{3.35}$$

and

$$\frac{dn_m^+}{dt} = \zeta n_H - \beta n_e n_m^+ - \beta_t n_M n_m^+ \,, \tag{3.36}$$

where ζ is the total ionisation rate, calculated as summarised in the previous sections, and $n_{\rm H}$ is the hydrogen number density from equation (3.29). From (3.35) and (3.36) it follows that, in equilibrium,

$$\beta_r n_e n_M^+ = \beta_t n_m^+ n_M \,. \tag{3.37}$$

In the previous expressions, β is the dissociative recombination rate coefficient for molecular ions, β_r is the radiative recombination rate coefficient for metal ions and β_t is the rate coefficient of charge transfer from molecular ions to metal atoms. If it is assumed that all metals are locked into dust grains, which have in turn sedimented towards the midplane of the disc (i.e. $n_M \approx 0$), equations (3.35) and (3.36), together with charge neutrality, $n_e = n_M^+ + n_m^+$, and appropriate values for the rate coefficients,

$$\beta_r = 3 \times 10^{-11} T^{-1/2} \,{\rm cm}^3\,{\rm s}^{-1} \,, \tag{3.38}$$

$$\beta = 3 \times 10^{-6} T^{-1/2} \, \mathrm{cm}^3 \, \mathrm{s}^{-1} \, , \tag{3.39}$$

$$\beta_t = 3 \times 10^{-9} \mathrm{cm}^3 \, \mathrm{s}^{-1} \, , \tag{3.40}$$

(see Fromang et al 2002 and references therein), lead to

$$n_e \approx \sqrt{\frac{\zeta n_H}{\beta}} \, . \tag{3.41}$$

However, as these authors point out also, dust grains not only absorb metal atoms, but also release them as a result of the action of x-rays. Because of this effect, the abundance of metal atoms in a disc could be quite insensitive to the spatial distribution of dust grains. This, in turn, means that dust settling does not necessarily lead to a severe reduction in the number density of metal atoms in the gas phase. If these dominate, the corresponding n_e is

$$n_e \approx \sqrt{\frac{\zeta n_H}{\beta_r}} \, . \tag{3.42}$$

The transition from one regime to the other is taken here to occur when x_M is such that $\beta_r n_e n_M^+ > \beta n_e n_m^+$. When this condition is satisfied, electrons are more likely to recombine radiatively with metal ions than they are to recombine dissociatively with molecular ions (see equation 3.35). Using (3.37), this leads to:

$$x_M > \frac{\beta}{\beta_t} x_e = 10^3 T^{-1/2} x_e \, . \tag{3.43}$$

Note that this minimum x_M for radiative recombination to dominate is more stringent (by 5 orders of magnitude) than the expression given by Fromang et. al. (2002). These authors identified the transition with $x_M \approx x_m^+$ and obtained $x_M > 10^{-2} T^{-1/2} x_e$ for metals to be dominant. However, given that $\beta_r \ll \beta$, when this condition is satisfied electrons will still be more likely to recombine with molecular ions. As a result, in this study we have adopted expression (3.43) as the minimum x_M for radiative recombination to dominate. The electron number density n_e and, hence, the magnetic coupling χ (see section 3.3.2) in the limit where dissociative recombination dominates (equation (3.41)) are $\sqrt{\beta_r/\beta} \sim 300$ times lower than the one obtained in the metal-dominated limit (equation (3.42)). However, the former

recombination mechanism dominates when $\beta_r n_e n_M^+ < \beta n_e n_m^+$, which gives a maximum x_M given by expression (3.43) with the appropriate x_e for this limit (equation (3.41)). This metal abundance is, similarly, a factor of ~ 300 lower than the minimum abundance for radiative dominance. As a result, the transition between these two regimes is not instantaneous: it occurs over a range of x_M. The full reduction in n_e –and χ– is only realised when x_M is a factor of ~ 300 below the critical value of equation (3.43). For the fiducial model this occurs 1.5 scaleheights above the location indicated by this expression. Finally, if X-rays are able to liberate metal atoms from dust grains and the metal abundance becomes fairly independent of the dust spatial distribution (Fromang et. al. 2002), then the actual x_M can be up to a factor of $1/\delta_2$ larger than the value adopted in this work (see section 3.4.2). If this is the case, the transition (from radiative to dissociative recombination regimes) will take place even higher above the midplane.

From the previous discussion, it is clear that the evolutionary stage –and activity– of the disc are important factors in the ionisation balance, as they influence the degree of sedimentation of dust grains. As the disc evolves, dust grains tend to occupy a thin layer around the midplane, becoming removed –in any dynamical sense– from the gas at higher vertical locations. This causes the ionisation fraction of the gas to increase, by eliminating recombination pathways on dust surfaces. In the present work, we have used equation (3.42) to calculate the electron (and ion) number density. The minimum values of x_M for this approximation to be valid (equation (3.43)) have also been computed and compared with an estimate of metal abundances in the gas phase (see section 3.4.2). Results indicate that, for the range of parameters adopted here, the abundance of metal atoms is such that radiative recombination is indeed dominant, except in the upper regions of the disc, so the use of equation (3.42) to calculate the electron fraction is justified.

3.3 METHODOLOGY

3.3.1 Linearisation

Full details of the methodology are described in SW03. For the sake of clarity, and completeness, we summarise here the most important steps and point at some differences with the previous formulation. The system of equations (3.1) to (3.3),

(3.6) and (3.7) was linearised about an initial steady state where fluid motion is exactly Keplerian and the magnetic field is vertical, so $\mathbf{J} = \mathbf{v} = \mathbf{E}' = 0$ and $\mathbf{B} = B\hat{z}$. In the initial state both $\mathbf{E}'$ and $\mathbf{J}$ vanish, so the changes in the conductivity tensor due to the perturbations do not appear in the linearised equations. As a result, it is not necessary to explore how the perturbations affect the conductivity of the fluid and only the values in the initial steady state are required.

We assume that the wavevector of the perturbations is perpendicular to the plane of the disc ($k = k_z$). These perturbations, initiated from a vertical magnetic field, are the fastest growing modes when the fluid is in either the Hall or resistive conductivity regimes, as in these cases magnetic pressure suppresses displacements with a non-zero radial wavenumber (Balbus & Hawley 1991, Sano & Miyama 1999). However, as pointed out by Kunz & Balbus (2004) and Desch (2004), this is not necessarily the case for perturbations in the ambipolar diffusion limit. The results of these studies indicate that in this regime, the fastest growing modes may exhibit both radial and vertical wavenumbers.

Taking perturbations of the form $\mathbf{q} = \mathbf{q}_0 + \delta\mathbf{q}(z)e^{i\omega t}$ about the initial state, linearising and neglecting terms of order H/r or smaller, we find that the final linear system of equations that describes the MHD perturbations within the disc is,

$$i\omega\rho\delta v_r - 2\rho\Omega\delta v_\phi - \frac{B_0}{c}\delta J_\phi = 0\,, \tag{3.44}$$

$$i\omega\rho\delta v_\phi + \tfrac{1}{2}\rho\Omega\delta v_r + \frac{B_0}{c}\delta J_r = 0\,, \tag{3.45}$$

$$i\omega\delta B_r - c\frac{d\delta E_\phi}{dz} = 0\,, \tag{3.46}$$

$$i\omega\delta B_\phi + c\frac{d\delta E_r}{dz} + \tfrac{3}{2}\Omega\delta B_r = 0\,, \tag{3.47}$$

$$\delta J_r = -\frac{c}{4\pi}\frac{d\delta B_\phi}{dz}\,, \tag{3.48}$$

$$\delta J_\phi = \frac{c}{4\pi}\frac{d\delta B_r}{dz}\,, \tag{3.49}$$

$$\delta J_r = \sigma_2\delta E'_r - \sigma_1\delta E'_\phi\,, \tag{3.50}$$

$$\delta J_\phi = \sigma_1 \delta E'_r + \sigma_2 \delta E'_\phi \,, \tag{3.51}$$

where δE_ϕ and δE_r are the perturbations of the electric field in the laboratory frame,

$$\delta E_\phi = \delta E'_\phi + \frac{B_0}{c}\delta v_r \,, \text{ and} \tag{3.52}$$

$$\delta E_r = \delta E'_r - \frac{B_0}{c}\delta v_\phi \,. \tag{3.53}$$

Note that $\sigma_\parallel$, the component of the conductivity tensor parallel to the magnetic field, does not appear in the linearised equations. This, in turn, implies that in the linear phase of the MRI and under the adopted approximations, the ambipolar diffusion and resistive conductivity regimes behave identically (see section 3.2.1).

We express equations (3.44) to (3.53) in dimensionless form by normalising the variables as follows:

$$z^* = \frac{z}{H} \qquad \rho^* = \frac{\rho(r,z)}{\rho_0(r)} \qquad \delta\mathbf{B}^* = \frac{\delta\mathbf{B}}{B_0}$$

$$\delta\mathbf{v}^* = \frac{\delta\mathbf{v}}{c_s} \qquad \delta\mathbf{E}^* = \frac{c\delta\mathbf{E}}{c_s B_0} \qquad \delta\mathbf{E}'^* = \frac{c\delta\mathbf{E}'}{c_s B_0}$$

$$\delta\mathbf{J}^* = \frac{c\delta\mathbf{J}}{c_s B_0 \sigma_\perp} \qquad \sigma^* = \frac{\sigma}{\sigma_\perp}$$

Here, subscript 'o' denotes variables at the midplane of the disc. Note that we have used the local $\sigma_\perp$ instead of $\sigma_{\perp_0}$, used in SW03, to normalise σ and $\delta\mathbf{J}$. This is more useful when dealing with a height-dependent conductivity. In the following dimensionless system, we have dropped the asterisks and expressed the final equations in matrix form:

$$\frac{d}{dz}\begin{pmatrix} B_r \\ B_\phi \\ E_r \\ E_\phi \end{pmatrix} = \begin{pmatrix} 0 & 0 & C_1 A_1 & C_1 A_2 \\ 0 & 0 & -C_1 A_2 & C_1 A_3 \\ -\frac{3}{2} & -\nu & 0 & 0 \\ \nu & 0 & 0 & 0 \end{pmatrix} \begin{pmatrix} B_r \\ B_\phi \\ E_r \\ E_\phi \end{pmatrix} \tag{3.54}$$

$$\delta\mathbf{J} = C_2 \begin{pmatrix} A_2 & -A_3 \\ A_1 & A_2 \end{pmatrix} \delta\mathbf{E} \tag{3.55}$$

$$\delta\mathbf{v} = \chi \frac{1}{1+\nu^2} \begin{pmatrix} -2 & \nu \\ -\nu & -\frac{1}{2} \end{pmatrix} \delta\mathbf{J} \tag{3.56}$$

$$\delta\mathbf{E}' = \frac{1}{\sigma_\perp} \begin{pmatrix} \sigma_2 & \sigma_1 \\ -\sigma_1 & \sigma_2 \end{pmatrix} \delta\mathbf{J} \tag{3.57}$$

where

$$\nu = \frac{i\omega}{\Omega}\,, \tag{3.58}$$

$$C_1 = \chi \left(\frac{v_A}{c_s}\right)^{-2} C_2\,, \tag{3.59}$$

$$C_2 = \left[1 + \chi \frac{1}{1+\nu^2}\left(\frac{5}{2}\frac{\sigma_1}{\sigma_\perp} + 2\nu\frac{\sigma_2}{\sigma_\perp} + \chi\right)\right]^{-1}\,, \tag{3.60}$$

$$A_1 = \frac{\sigma_1}{\sigma_\perp} + 2\chi\frac{1}{1+\nu^2}\,, \tag{3.61}$$

$$A_2 = \frac{\sigma_2}{\sigma_\perp} + \nu\chi\frac{1}{1+\nu^2}\,, \text{ and} \tag{3.62}$$

$$A_3 = \frac{\sigma_1}{\sigma_\perp} + \frac{1}{2}\chi\frac{1}{1+\nu^2}\,. \tag{3.63}$$

In the above expressions,

$$v_A = \frac{B_o}{\sqrt{4\pi\rho}} \tag{3.64}$$

is the local Alfvén speed in the disc, and

$$\chi \equiv \frac{\omega_c}{\Omega} \equiv \frac{1}{\Omega}\frac{B_o^2\sigma_\perp}{\rho c^2} \tag{3.65}$$

controls the local coupling between the magnetic field and the disc (W99, SW03, see also section 3.3.2). Non-ideal effects strongly modify wavemodes at, or above, the critical frequency ω_c.

3.3.2 Parameters

The following parameters control the dynamics and evolution of the fluid:

1. v_A/c_s, the ratio of the local Alfvén speed to the isothermal sound speed of the gas. It is a measure of the strength of the magnetic field. In ideal-MHD conditions, unstable modes grow when the magnetic field is subthermal ($v_A/c_s < 1$). Under this approximation, when $v_A \sim c_s$ the minimum wavelength of the instability is of the order of the scale height of the disc and the growth rate decreases rapidly. This is also the case under the assumption that ambipolar or ohmic diffusion dominates over the entire cross-section of the disc (SW03). However, when the fluid is in the Hall regime, with the magnetic field counter-aligned with the angular velocity vector of the disc ($\mathbf{\Omega} \cdot \mathbf{B} < 0$), MRI unstable modes may exist for stronger fields, up to $v_A/c_s \sim 3$ (SW03).

2. χ, a parameter that characterises the strength of the local coupling between the magnetic field and the disc (equation (3.65)). It is given by the ratio of the critical frequency above which flux-freezing conditions break down and the dynamical (Keplerian) frequency of the disc. If $\chi \equiv \omega_c/\Omega < 1$, the disc is poorly coupled to the disc at the frequencies of interest for dynamical analysis, which are also the interesting frequencies for the study of the MRI.

3. σ_1/σ_2, the ratio of the conductivity terms perpendicular to the magnetic field. It is an indication of the conductivity regime of the fluid, as discussed in section 3.2.1.

We calculated the values of the three parameters above at different locations (r, z) within the disc using equations (3.9), (3.10), (3.17), (3.64) and (3.65). The strength of the magnetic field is a free parameter: we consider field strengths in excess of 1 mG.

3.3.3 Boundary Conditions

To solve equations (3.54) to (3.57) it is necessary first to integrate the system of ordinary differential equations (ODE) in (3.54). This can be treated as a two-point boundary value problem for coupled ODE. Five boundary conditions must be formulated, prescribed either at the midplane or at the surface of the disc.

At the midplane: We chose to assign odd symmetry to δB_r and δB_ϕ, so they vanish at $z = 0$. This gives us two boundary conditions at the midplane. Also, as the equations are linear, their overall scaling is arbitrary, and a third boundary condition can be obtained by setting one of the fluid variables to any convenient value. To that effect, we assigned a value of 1 to $\delta E'_r$. The three boundary conditions applied at the midplane are, then:

$$\delta B_r = \delta B_\phi = 0, \text{ and}$$

$$\delta E'_r = 1\,.$$

At the surface: χ is inversely proportional to the density (equation 3.65), so if the conductivity is assumed to be constant with height, it increases monotonically with z. This was the case in SW03, where we used this argument to propose that at sufficiently high z above the midplane, ideal MHD conditions held. This, in turn, implies that the wavelengths of magnetic field perturbations, given the adopted dependency of ρ with z (equation (3.26)), must tend to infinity when $z \to \infty$. As a result, the amplitude of such modes should vanish at infinity as well. Here, however, the conductivities vary with z, so this argument needs revisiting. In section 3.4.3 we analyse the dependency of χ with height for different radial positions and a range of magnetic field strengths. Here, we just highlight that at the surface of the disc ($z/H = 6$, see below), the magnetic coupling is still strong. For example, for the fiducial model at $R = 1$ AU, $\chi \sim 20$. It decreases to ~ 4.5 for $R = 5$ AU and to ~ 2.5 for $R = 10$ AU. This is still above the limit (~ 1) for strong coupling (W99).

When $\chi > 10$ the growth rate and characteristic wavenumber of local unstable modes differ little from the ideal limit (W99), so the same line of reasoning

of SW03 can be used to argue that in this case δB_r and δB_ϕ should be zero at the boundary as well. Although χ at the surface when $R \gtrsim 5$ AU is below 10, it is considered that the magnetic coupling there is still sufficiently strong for the ideal-MHD approximation to be essentially valid as well. This is also confirmed by the way in which magnetic field perturbations tend to zero at the boundary at these radii (see results in sections 3.4 and 3.5). Consistently with this, both $\delta\mathbf{E}'$ and $\delta\mathbf{J}$ vanish at the surface as well. This gives us the remaining two boundary conditions required to integrate the system of equations (3.54). Gammie & Balbus (1994) obtained similar boundary conditions for their 'hot halo model', where the disc is terminated in a hot, perfectly conducting halo at a height z_h above the midplane. These authors showed that the perturbed magnetic field in this halo is approximately force-free, so $(\nabla\times\delta\mathbf{B})\times\mathbf{B}_o \approx 0$, and $\nabla\times\delta\mathbf{B} = a\mathbf{B}_o$. In the last expression, 'a' is a function that is constant along the unperturbed field lines. For vanishing stress at infinity –the condition we are adopting here–, $a \equiv 0$, which recovers the conditions $\delta B_r = \delta B_\phi = 0$ at the surface of the disc.

We chose to locate the boundary at $z/H = 6$, after confirming that increasing this height does not significantly affect either the structure or the growth rate of unstable modes. Summarising, the boundary conditions adopted at the surface are:

$$\delta B_r = \delta B_\phi = 0$$

at $z/H = 6$.

This system of equations is solved by 'shooting' from the midplane to the surface of the disc while simultaneously adjusting the growth rate ν and $\delta E'_\phi$ at the midplane. The adjustment is done via a multidimensional, globally convergent Newton-Raphson method, until the solution converges. The procedure involves supplying initial –guessed– values for these two variables to start the iteration. In order to avoid missing an unstable mode –in particular, the fastest growing mode– we succesively tried guessed values of ν_{max} in the range of 0.1 to 1.0, in intervals of 0.01. Given that $\nu_{max} < 0.75$ (BH91) we are confident that the most unstable mode is not missed, even though it can not be guaranteed that all modes are always found.

3.4 DISC CONDUCTIVITY

3.4.1 Test Models

Our fiducial model is based on the solar nebula disc (Hayashi 1981; Hayashi, Nakazawa & Nakagawa 1985; see section 3.2.2). The structure and growth rate of MRI unstable modes are calculated at representative radial positions (R = 1, 5 and 10 AU) from the central protostar. Two scenarios are explored: Cosmic rays either penetrate the disc, although attenuated as appropriate (as given by eq. (3.30)), or they are excluded from it by the winds produced by the central object. Unless stated otherwise, results presented using this model include cosmic ray ionisation. We also consider a disc model with an increased mass and surface density, as described in section 3.2.2. For simplicity, other disc parameters remain unchanged and in this case, all calculations incorporate the ionisation rate provided by cosmic rays.

We also compare solutions obtained using different configurations of the conductivity tensor. By comparing the structure and growth rate of unstable modes found using the commonly adopted ambipolar diffusion – or resistive – ($\sigma_1 = 0$) approximations with those obtained with a full conductivity tensor ($\sigma_1 B_z > 0$, $\sigma_2 \neq 0$), as well as the less common Hall limit ($\sigma_2 = 0$, $\sigma_1 B_z > 0$), we can appreciate how, and in which regions of parameter space, Hall conductivity alters the properties of the instability. This is explored for the fiducial model at 1 AU only.

The properties of the MRI in the Hall limit are dependent on the alignment of the magnetic field and angular velocity vectors of the disc (W99). The case when these vectors are parallel (antiparallel) is characterised by $\sigma_1 B_z > 0$ ($\sigma_1 B_z < 0$). In the Hall ($\sigma_1 B_z < 0$) limit, our code fails to converge whenever the combination of parameters is such that $\chi < 2$ anywhere in the domain of integration. This is not surprising as, in this regime, when $0.5 < \chi < 2$ all wavenumbers are unstable (W99). As a result, we explored the effect of the alignment of $\mathbf{B}$ and $\mathbf{\Omega}$ by comparing solutions obtained with a full conductivity tensor but incorporating $\sigma_1 B_z$ terms of opposite sign. Even with this approach, solutions including a $\sigma_1 B_z < 0$ term could not be computed at all for R = 1 AU, given that the midplane coupling at this radius is extremely low ($\sim 10^{-10}$ to 10^{-2} for B between 1 mG and 1 G). Therefore, we present this analysis at 5 and 10 AU only. Solutions incorporating a negative Hall conductivity could be obtained for $B \gtrsim 8$ mG at 5 AU and $B \gtrsim 1.5$ mG at 10

AU, where the magnetic coupling at the midplane is $\gtrsim 2$.

Unless stated otherwise, results discussed in the following sections incorporate a $\sigma_1 B_z > 0$ Hall term contribution.

3.4.2 Ionisation Rates

Fig. 3.1 shows the ionisation rate contributed by cosmic rays, x-rays and radioactive materials as a function of height for the fiducial model. Results are presented at the radial locations of interest: 1, 5 and 10 AU. Note that x-rays penetrate up to $z/H \sim 1.7$ and $z/H \sim 0.3$ for $R = 1$ and 5 AU, respectively. They reach the midplane for $R = 10$ AU. The x-ray ionisation rate is heavily attenuated below ~ 1.5 to 2 scaleheights from the surface, depending on the radius.

At 1 and 5 AU, the regions where x-rays are not able to penetrate are ionised only by the action of cosmic rays (if present) and radioactive decay. Moreover, cosmic rays constitute the most efficient ionising agent for $z/H \lesssim 2.2$ at all studied radii. As a result, if they are excluded from the disc by the protostar's winds (i.e. Fromang et al. 2002), the magnetic coupling of the gas in these sections of the disc is expected to be severely reduced. In order to explore the properties of MRI perturbations under this assumption, we compare results computed including and excluding this source of ionisation for the fiducial model (sections 3.5.1 and 3.5.1 respectively).

Igea & Glassgold (1999) have pointed out that in protostellar discs, the x-ray ionisation rate can be 10^3 - 10^5 times that of interstellar cosmic rays. Their calculations show that x-rays dominate over cosmic rays until the vertical column density, $N_\perp$, is 10^{25}, 5×10^{23} and $2 \times 10^{23}\,\mathrm{cm}^{-2}$ for $R = 1$, 5 and 10 AU, respectively. Once $N_\perp$ exceeds $\sim 10^{25}\,\mathrm{cm}^{-2}$, x-ray ionisation dies out because there are no remaining incident photons available. The ionisation rates adopted in this study (Fig. 3.1) are in agreement with these findings.

We have used eq. (3.42) to calculate the electron number density (section 3.2.3). This expression is valid when metal atoms dominate and electrons recombine primarily via radiative processes. Here, we justify this choice. Fig. 3.2 compares the minimum abundance of metals, (eq. (3.43)), for this approximation to be valid with an estimate of total metal abundances in the gas phase. Minimum abundances (relative to hydrogen) are shown for the radial locations of interest for the fiducial

model. The total gas-phase metal abundance is taken as $8.4 \times 10^{-5}\delta_2$ (Umebayashi & Nakano 1990). From Fig. 3.2 it is clear that the abundance of gas-phase metal atoms is expected to exceed the minimum for radiative recombination processes to be dominant at all radii of interest here, except in the upper sections of the dics (i.e. $z/H \lesssim 3.5$ at 1 AU). Given that the fastest growing MRI modes are strongly damped in these regions (see Fig. 3.9), and that the full impact on n_e (and χ) when dissociative recombination dominates is not achieved until x_M is a factor of ~ 300 below the critical value of equation (3.43), (see section 3.2.3), we conclude that equation (3.42) is still a valid approximation to calculate the electron number density in this study.

3.4.3 Magnetic coupling and conductivity regimes as a function of height

It is interesting to explore which conductivity terms (section 3.2.1) are dominant at different heights at the representative radial locations we are considering. This information will be used in the analysis of the structure and growth of MRI unstable modes in the next section. We recall that Hall diffusion is locally dominant when (SW03),

$$\chi < \chi_{crit} \equiv \frac{|\sigma_1|}{\sigma_\perp}\,. \tag{3.66}$$

When χ is higher than this, but still $\lesssim 10$, ambipolar diffusion dominates. In regions where χ is stronger, ideal-MHD conditions hold (W99). We remind the reader than in the present formulation, the ambipolar and Ohmic conductivity regimes behave identically. This is the case because $\sigma_\parallel$ (the conductivity component that distinguishes between them), does not appear in the final, linearised system of equations (see section 3.3.1). This should be kept in mind when analysing the results, as even though the case where $\sigma_1 = 0$ has been referred to as the 'ambipolar diffusion' limit ($\sigma_\parallel \gg \sigma_2$), it is also consistent with the 'resistive' regime ($\sigma_\parallel \sim \sigma_2$).

We are interested in comparing χ and χ_{crit} as a function of height for different disc models, radial locations and choices of the magnetic field strength. An example of the typical dependency of these variables with z is shown in Fig. 3.3 for the fiducial model at $R = 1$ AU for $B = 10$ mG. Note that the conductivity term parallel to the field increases monotonically with z and is independent of B (see eqs.

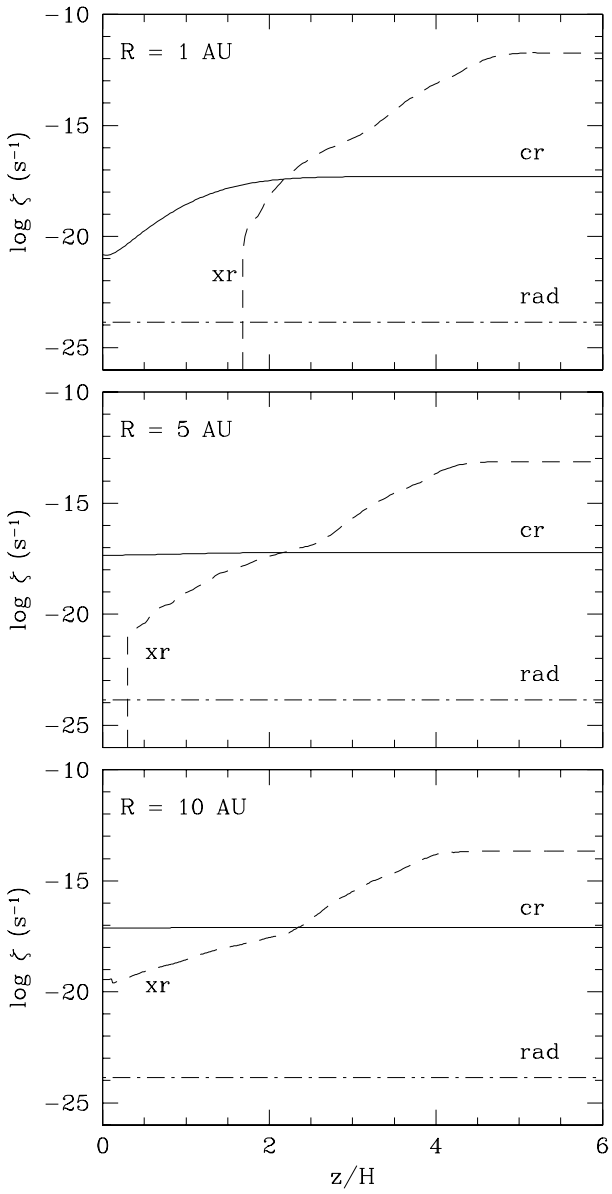

Figure 3.1 Ionisation rate (s^{-1}) contributed by cosmic rays (curve labeled 'cr'), x-rays (xr) and radioactive materials (rad) as a function of height, for the fiducial model (minimum mass solar nebula disc). Results are shown for $R = 1$, 5 and 10 AU. Note that at 1 AU, cosmic ray ionisation is attenuated with respect to the interstellar rate for $z/H \lesssim 2$. Also, x-rays are excluded from the disc for $z/H \lesssim 1.7$ (at 1 AU) and $z/H \lesssim 0.3$ (at 5 AU). For $R = 10$ AU, they reach the midplane, although their ionisation rate is heavily attenuated. Cosmic rays (if present) are the most efficient ionising agent for $z/H \lesssim 2.2$ in all cases.

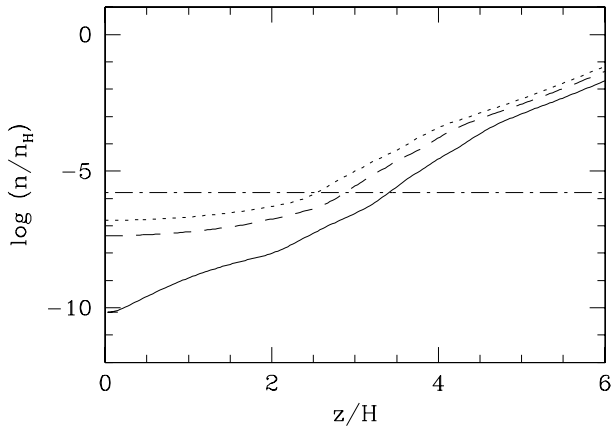

Figure 3.2 Comparison of the minimum abundance of metal atoms in the gas phase, $x_M = n_M/n_H$, for the radiative recombination rate of metal ions (β_r) to be the dominant recombination mechanism, and an estimate of the total gas-phase metal abundance, as a function of height. Minimum abundances are shown for the fiducial model at 1 AU (solid line), 5 AU (dashed line) and 10 AU (dotted line). The estimated total gas-phase metal abundance (dot-dashed line) is from Umebayashi & Nakano (1990). This abundance exceeds the minimum required for all radii and vertical locations of interest in this study, except in the upper sections of the disc. This is not expected to significantly affect the results presented in this study, given that the fastest growing MRI modes are strongly damped in these regions.

(3.8) and (3.12)). In this case, $|\sigma_1|$ is nearly two orders of magnitude smaller than σ_2 at the midplane. As a result, near the midplane $\sigma_\parallel \sim \sigma_2 \gg |\sigma_1|$, and the fluid is in the resistive regime (section 3.2.1). This is consistent with findings by Wardle (in preparation), that Ohmic conductivity is important at this radius for relatively weak fields ($B \lesssim 100$ mG) when the density is sufficiently high (e.g. $n_H \gtrsim 10^{12}\,\mathrm{cm}^{-3}$ for $B = 1$ mG). Both components of the conductivity tensor perpendicular to the field increase with height initially, reflecting the enhanced ionisation fraction at higher z. There is then a central section of the disc where $|\sigma_1| \gg \sigma_2$ (the fluid is in the Hall regime) and finally, both terms drop abruptly closer to the surface as a consequence of the fall in fluid density. Note that the Hall conductivity term decreases much more sharply than the ambipolar diffusion component. As a result, the ambipolar diffusion term is typically several orders of magnitude greater than the Hall term in the surface regions of the disc. To reiterate this concept, we repeat here that even in

regions where $|\sigma_1| \ll \sigma_2$, the growth and structure of the MRI in the linear regime are still dominated by Hall diffusion if $\chi \lesssim |\sigma_1|/\sigma_\perp$ (SW03).

The previous results are in agreement with the notion that $|\sigma_1| > \sigma_2$ at intermediate heights, where $|\beta_e| \gg 1$ while $\beta_i \ll 1$. At higher z, typically $|\beta_e| \gg \beta_i \gg 1$ and the fluid is in the ambipolar diffusion regime. In these conditions, equations (3.9) and (3.10) show that $|\sigma_1| \ll \sigma_2$. On the contrary, near the midplane either component may dominate, depending on the fluid density and the strength of the magnetic field. $|\sigma_1|$ will be larger if the fluid density is relatively small (larger radius) and/or the field is stronger. Conversely, if the field is weak and the density is sufficiently high, $\sigma_\parallel \sim \sigma_2 \gg |\sigma_1|$ and the conductivity will be resistive. This behaviour of the conductivity components as a function of height explains, in turn, the dependency of χ_{crit} with z: For weak fields it is $\ll 1$ near the midplane ($\sigma_2 \gg |\sigma_1|$), but if B is sufficiently strong, χ_{crit} close to the midplane ~ 1. It then increases with z and levels in the intermediate sections of the disc at ~ 1 ($|\sigma_1| \gg \sigma_2$). Finally, χ_{crit} drops sharply near the surface ($\sigma_2 \gg |\sigma_1|$ again).

We now briefly turn our attention to the dependency of the magnetic coupling with height. Note that χ first increases with z, as expected, in response to the enhanced ionisation fraction, and lower fluid density, away from the midplane. Closer to the surface, it decreases again, as a result of the abrupt drop in the magnitudes of the conductivity components. In the following subsections we explore more fully the dependency of χ versus χ_{crit} with height, which indicates which non-ideal MHD regime is locally dominant, for the disc models of interest.

Minimum-mass solar nebula disc

Figs. 3.4 to 3.6 present curves of χ (solid lines) and $\chi_{crit} \equiv |\sigma_1|/\sigma_\perp$ (dashed lines) as a function of height for the fiducial model. Results are shown for $R = 1$, 5 and 10 AU and different choices of the magnetic field strength. Cosmic rays are either included (top panel of each figure) or excluded from the disc (bottom panels). Bottom (solid) and leftmost (dashed) curves correspond to $B = 1$ mG in all cases. B changes by a factor of 10 between curves, except that for 5 and 10 AU the top (and rightmost) curves correspond to the maximum field strength for which perturbations grow. Fluctuations in the magnetic coupling at low z/H (lower panel of Fig. 3.5) reflect fluctuations in the X-ray ionisation rate (Fig. 3, Igea & Glassgold 1999) in

this region of parameter space.

We note that in all plots, the magnetic coupling near the midplane increases with B. In these regions of the disc, both β_i and β_e are typically $\ll 1$ (except possibly when B is very strong) and from equation (3.11),

$$\sigma_\perp \approx \frac{cen_e}{B}(\beta_i - \beta_e)\,, \tag{3.67}$$

which is independent of B. As a result, $\chi \propto B^2$. On the contrary, near the surface the β_j can be very large and

$$\sigma_\perp \approx \frac{cen_e}{B}\frac{(\beta_i - \beta_e)}{\beta_e\beta_i} \propto \frac{1}{B^2}\,. \tag{3.68}$$

Because of this, near the surface χ is quite insensitive to changes in B, as evidenced in Figs. 3.4 to 3.6.

Note that when cosmic rays are assumed to be excluded from the disc, there is a discontinuity in the curve of χ vs. z/H at $R = 1$ and 5 AU. This discontinuity is caused by the drop in the ionisation fraction at the height where x-rays are not able to penetrate any further within the disc (see bottom panels of Figs. 3.4 and 3.5). It is, therefore, not present at 10 AU, because x-rays reach the midplane at this radius (see bottom panel of Fig. 3.6).

In general, when B increases, the region around the midplane where Hall diffusion is locally dominant ($\chi < |\sigma_1|/\sigma_\perp$) is reduced, as a result of the stronger magnetic coupling. At 1 AU, when cosmic ray ionisation is included, this criterion is satisfied in the inner sections of the disc for all magnetic field strengths of interest (Fig. 3.4, top panel). Above this region, there is a relatively small section where ambipolar diffusion is locally dominant while near the surface, ideal-MHD holds for all magnetic field strengths.

For $R = 5$ AU (Fig. 3.5, top panel), Hall diffusion dominates for $z/H \lesssim 2$ when $B \lesssim 10$ mG, but for 10 mG $\lesssim B \lesssim 100$ mG, ambipolar diffusion is locally dominant in the inner sections of the disc ($|\sigma_1|/\sigma_\perp < \chi < 10$). For stronger fields, the magnetic coupling is such that $\chi > 10$ even at the midplane and the fluid is in ideal-MHD conditions over the entire cross-section of the disc. At this radius, the fluid is in the resistive regime only for very weak fields ($B \lesssim 1$ mG) and very high densities ($n_H > 10^{12}\,\mathrm{cm}^{-3}$; Wardle, in prep.). Similarly, results at $R = 10$ AU (Fig. 3.6, top panel), show that ambipolar diffusion dominates in the inner sections of the

disc for $B < 10$ mG. For stronger fields, ideal-MHD is a good aproximation at all z.

When cosmic rays are assumed to be excluded from the disc, the previous results at 1 AU (bottom panel of Fig. 3.4) are largely unchanged, except for those obtained with $B = 1$ G, where Hall diffusion dominates now for $z/H \sim 1.8$, up from ~ 1 in the previous case. This is due to the sharp fall in the magnetic coupling in the region which x-rays are unable to reach. At 5 AU, the Hall regime is now dominant near the midplane for all studied magnetic field strengths, while for $R = 10$ AU there is now a Hall dominated central region for $B \lesssim 10$ mG. It extends to $z/H \sim 1.3$. When $B \lesssim 100$ mG, ambipolar diffusion dominates near the midplane, but for stronger fields ideal MHD holds for all z.

Finally, we observe that (as expected), the magnetic coupling at the midplane increases with radius in response to the higher ionisation fraction in the central sections of the disc at larger radii. In fact, χ_o increases by 3 - 4 orders of magnitude between $R = 1$ and 10 AU. On the contrary, the coupling at the surface does not change as much with radius, decreasing only from ~ 22 to ~ 2.5 between the same radii.

A more massive disc

Fig. 3.7 displays curves of χ and χ_{crit} as a function of height for a more massive disc, as detailed in section 3.2.2. The ionisation balance is calculated assuming that cosmic rays penetrate the disc and results are shown for $R = 1$, 5 and 10 AU for the same range of magnetic field strengths explored in the minimum-mass solar nebula model.

Increasing the surface density causes the ionisation fraction near the midplane to drop sharply. As a result, the magnetic coupling is drastically reduced in these regions at all radii. This is especially noticeable at 1 AU, where in this case x-rays are completely attenuated for $z/H < 2.6$. This, together with a very weak ionisation rate ($\zeta_{CR} \sim 10^{-18}$ for $z/H \approx 2.6$ and it is negligible at $z = 0$), causes χ to be very low – and only weakly dependent on z – in this section of the disc.

The weaker coupling at low z results in Hall diffusion being locally dominant over a larger cross-section of the disc in this model. We find that for $R = 1$ AU, there is again a Hall dominated region about the midplane for all studied B. This section now extends to $z/H \sim 2.3$ for $B = 1$ G, up from $z/H \sim 1$ in the minimum-mass

solar nebula disc. For weaker fields, these regions are also larger.

For $R = 5$ AU, Hall diffusion is now dominant near the midplane for $B < 1$ G. For comparison, in the previous case Hall conductivity was locally important for $B < 10$ mG. Furthermore, ambipolar diffusion dominates over a small cross-section of the disc for all but the strongest ($B \gtrsim 1$ G) magnetic field strengths at this radius. This contrasts with the previous case, where ideal MHD held at all z when $B \gtrsim 100$ mG. Even at 10 AU, Hall diffusion now dominates near the midplane when $B \lesssim 10$ mG. When B is stronger than this, but still $\lesssim 100$ mG, ambipolar diffusion predominates for $z/H \lesssim 2$, while in the minimum-mass solar nebula, ideal-MHD held for $B \gtrsim 10$ mG.

3.4.4 Magnetic field strength

In the following sections we will discuss how the properties of the MRI depend on the strength of the unperturbed magnetic field B_o. The origin of this field, as well as its likely configuration in protoplanetary discs, remains unclear. Two main scenarios have been considered in the literature to explain the magnetisation of discs (e.g. Stepinski 1995): On the one hand, the field may originate in the molecular cloud from which the material that forms the protostar–disc system has collapsed. In this case the field is advected in, as well as amplified, during the collapse (Pudritz & Norman 1983, Königl 1989). This is an attractive picture, because the resulting field configuration seems favourable for driving hydromagnetic winds, so commonly observed in young stellar objects. On the other hand, the field can be generated within the disc itself, as a result of dynamo action (Tout & Pringle 1992, 1996; Stepinski 1995). In this scenario, the dynamo amplifies an arbitrarily small pre-existing seed field.

The magnetorotational instability itself has been associated with a self-sustaining dynamo model (Tout & Pringle 1992): The disc shear turns B_r into B_ϕ while the MRI creates both horizontal field components from the vertical field. Finally, B_z is generated from both B_r and B_ϕ by the Parker instability. It has been argued that this mechanism can generate a quasi-steady-state dynamo with an associated viscosity parameter $\alpha \lesssim 1$ (Tout & Pringle 1992). It may also mantain a distribution of flux loops in all scales through an 'inverse cascade' process (Tout & Pringle 1995), which produces large loops from the original smaller ones via reconnection of the

field lines. As a result, the original flux loops of length-scale $\lesssim H$ produced by the dynamo can be transformed into loops of the appropriate scale ($\sim R$) for the launching of centrifugally-driven winds and jets.

As mentioned above, a shared consensus on whether the magnetic field in protoplanetary discs is generated in the disc or in the parent cloud has not been reached. We do not explore this issue any further, given that in this study the initial magnetic field B_o is a free parameter. In the next section, we analyse the effect of different conductivity regimes being dominant at different heights, in the structure and growth rate of MRI perturbations. Different disc models, radial locations and magnetic field strengths are discussed.

3.5 MAGNETOROTATIONAL INSTABILITY

3.5.1 Structure of the perturbations

All unstable modes at 1 AU

Fig. 3.8 shows the structure and growth rates of all unstable MRI perturbations for the fiducial model at 1 AU and $B = 100$ mG. Solid lines denote δB_r while dashed lines correspond to δB_ϕ. This notation is observed in this paper in all plots that display the structure of the instability.

The fastest growing perturbation in this case grows at $\nu = 0.5020$ and there are 15 unstable modes with $0.1151 \leq \nu \leq 0.5020$. Slow growing perturbations, with $\nu < 0.1806$, are active even at the midplane, while faster modes exhibit a central magnetically inactive (dead) zone (Gammie 1996, Wardle 1997). Moreover, the extent of the dead zone increases with the growth rate and for the fastest growing mode it extends to $z/H \sim 1.6$. We observe that δB_r and δB_ϕ, especially in the slow growing modes, are asymmetrical about zero and their averages over vertical sections of the disc have opposite signs. This appears to be related to the dependency of these two fluid variables in equation (3.47).

Most unstable modes at different radii, including cosmic ray ionisation

The weakest strength for which unstable modes could be computed was 1 mG. This is a computational, rather than a physical limit: the dependency of ν_{max} with B

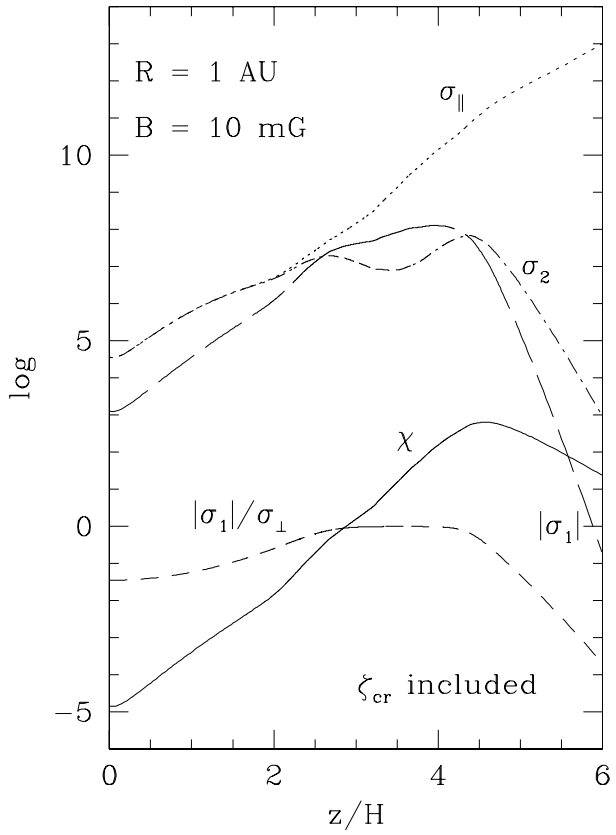

Figure 3.3 Example of the dependency of the conductivity components parallel ($\sigma_\parallel$) and perpendicular ($|\sigma_1|$ and σ_2) to the field, magnetic coupling (χ) and $\chi_{crit} \equiv |\sigma_1|/\sigma_\perp$ as a function of height. Results shown correspond to the fiducial model for $R = 1$ AU and $B = 10$ mG. Note that for $z/H \lesssim 2$, $\sigma_\parallel \sim \sigma_2 \gg |\sigma_1|$ and the conductivity is resistive. There is then a central section for which $|\sigma_1| \gg \sigma_2$ (the fluid is in the Hall conductivity regime), while for higher vertical locations $\sigma_\parallel \gg \sigma_2 \gg |\sigma_1|$ and ambipolar diffusion dominates. In the region where $\chi < \chi_{crit}$, Hall diffusion dominates the structure and growth rate of the MRI (SW03). Note also that χ could be reduced by up to a factor of 300 near the surface if dissociative – and not radiative – recombination dominates the ionisation balance at high z above the midplane.

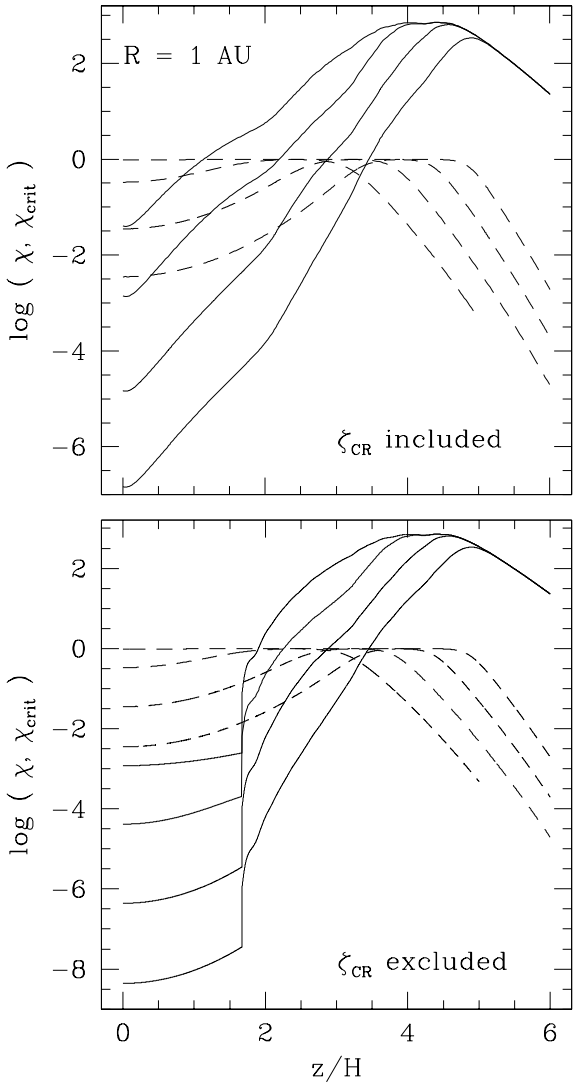

Figure 3.4 Comparison of the local magnetic coupling χ (solid lines) and $\chi_{crit} \equiv |\sigma_1|/\sigma_\perp$ (dashed lines) for the fiducial model at $R = 1$ AU and different choices of the magnetic field strength. In each case, Hall diffusion is dominant in the regions where $\chi < \chi_{crit}$ (SW03). Ambipolar diffusion dominates where $\chi_{crit} < \chi \lesssim 10$. When χ is stronger than this, the fluid is in nearly ideal-MHD conditions (W99). From top to bottom (solid lines), and right to left (dashed lines), the magnetic field drops from 1 G to 1 mG. B changes by a factor of 10 between curves in all cases. Top panel: Cosmic rays are present. Hall diffusion dominates for $z/H \lesssim 3.5$ to $z/H \lesssim 1$ for B increasing from 1 mG to 1 G, respectively. Bottom panel: Cosmic rays are excluded from the disc by protostellar winds. Note the discontinuity in χ at the height below which x-rays are completely attenuated.

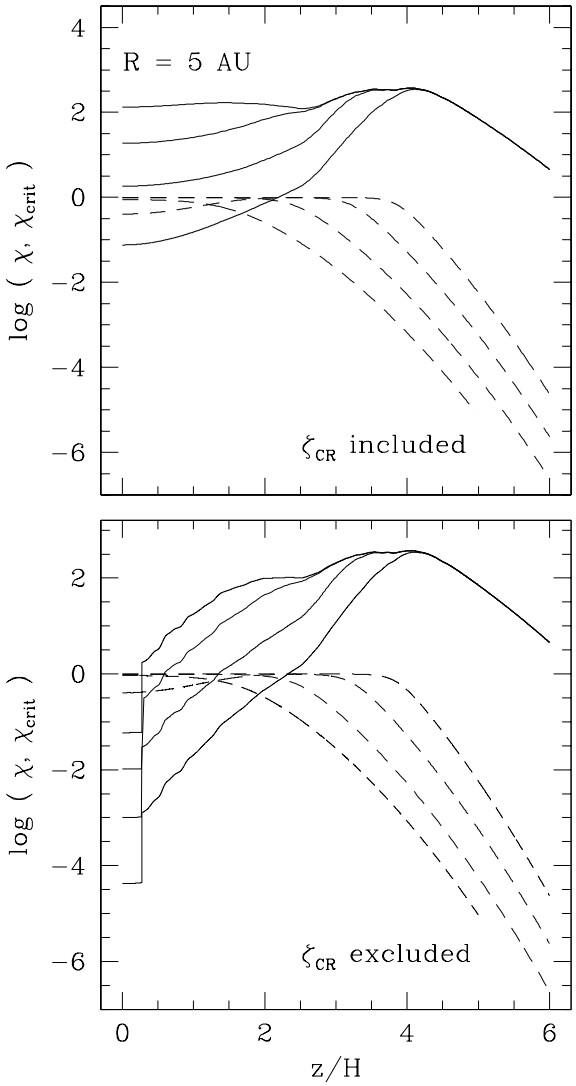

Figure 3.5 As per Fig. 3.4 for $R = 5$ AU. Top (and rightmost) lines correspond here to $B = 795$ mG (top panel) and $B = 615$ mG (bottom panel), which are the maximum field strengths for which perturbations grow in each scenario. When cosmic rays are included, the Hall regime dominates near the midplane for $B \lesssim 10$ mG. Similarly, for $B < 100$ mG, there is an intermediate region where $|\sigma_1|/\sigma_\perp < \chi < 10$, and ambipolar diffusion is dominant. For stronger fields, ideal-MHD holds for all z. When cosmic rays are excluded, Hall diffusion dominates near the midplane, and ambipolar diffusion is dominant at intermediate heights, for all B of interest here.

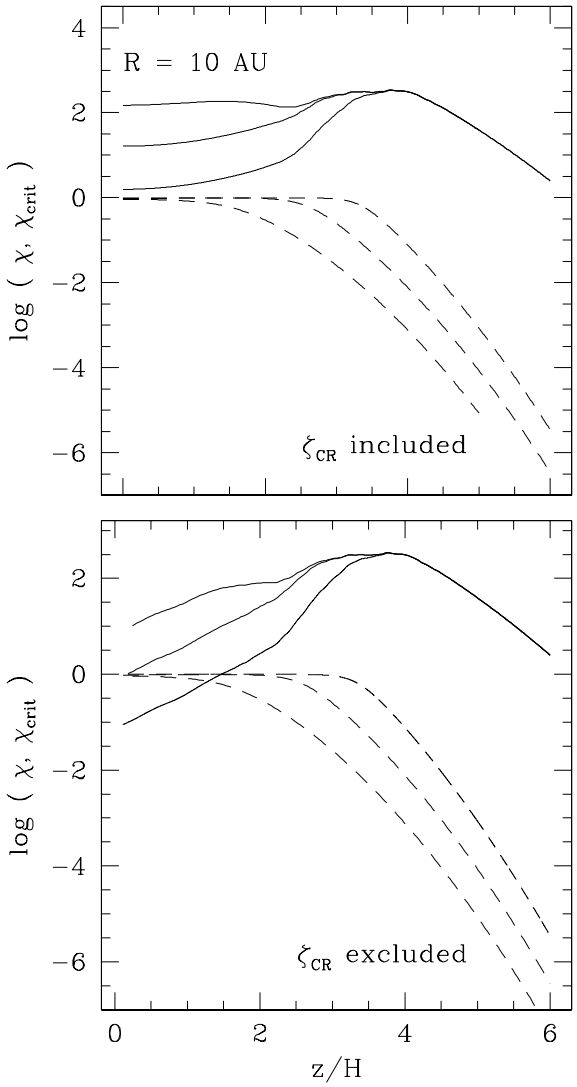

Figure 3.6 As per Figs. 3.4 and 3.5 for $R = 10$ AU. From top to bottom (and right to left), lines correspond here to $B = 100$, 10 and 1 mG. In this case, if cosmic rays are present, Hall diffusion is not dominant locally for any field strength, given the strong magnetic coupling near the midplane. Ambipolar diffusion dominates when $B \lesssim 10$ mG, but for stronger fields ideal-MHD holds over the entire cross-section of the disc. If cosmic rays are removed, the Hall regime is relevant near the midplane only for $B \lesssim 10$ mG. When $B \gtrsim 100$ mG, ideal MHD holds for all z.

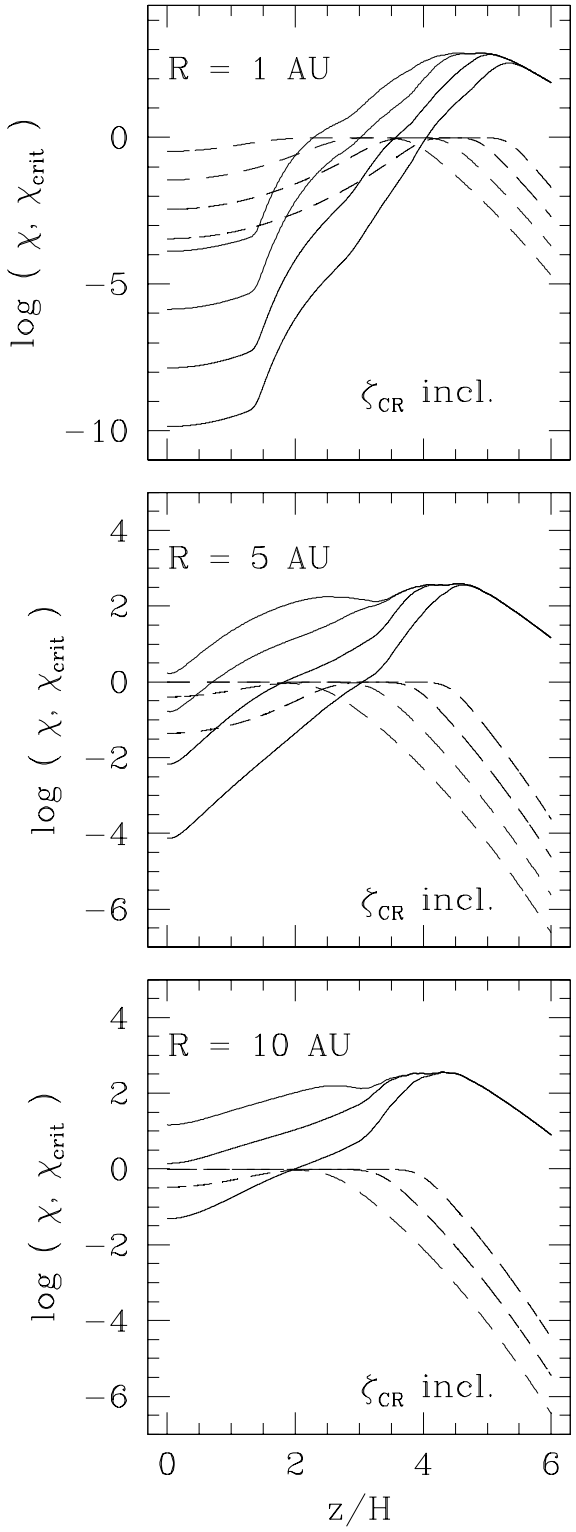

Figure 3.7 As per Figs. 3.4 to 3.6 for $R = 1$, 5 and 10 AU for a more massive disc, such that $\Sigma_o^{'} = 10\Sigma_o$ and $\rho_o^{'} = 10\rho_o$. Cosmic rays are present. From top to bottom (and right to left), lines correspond to $B = 1$, 0.1, 10^{-2} and 10^{-3} G ($R = 1$ and 5 AU), and $B = 0.1$, 10^{-2} and 10^{-3} G ($R = 10$ AU). The increased surface density causes the magnetic coupling to drop near the midplane. As a result, Hall conductivity dominates over a larger section

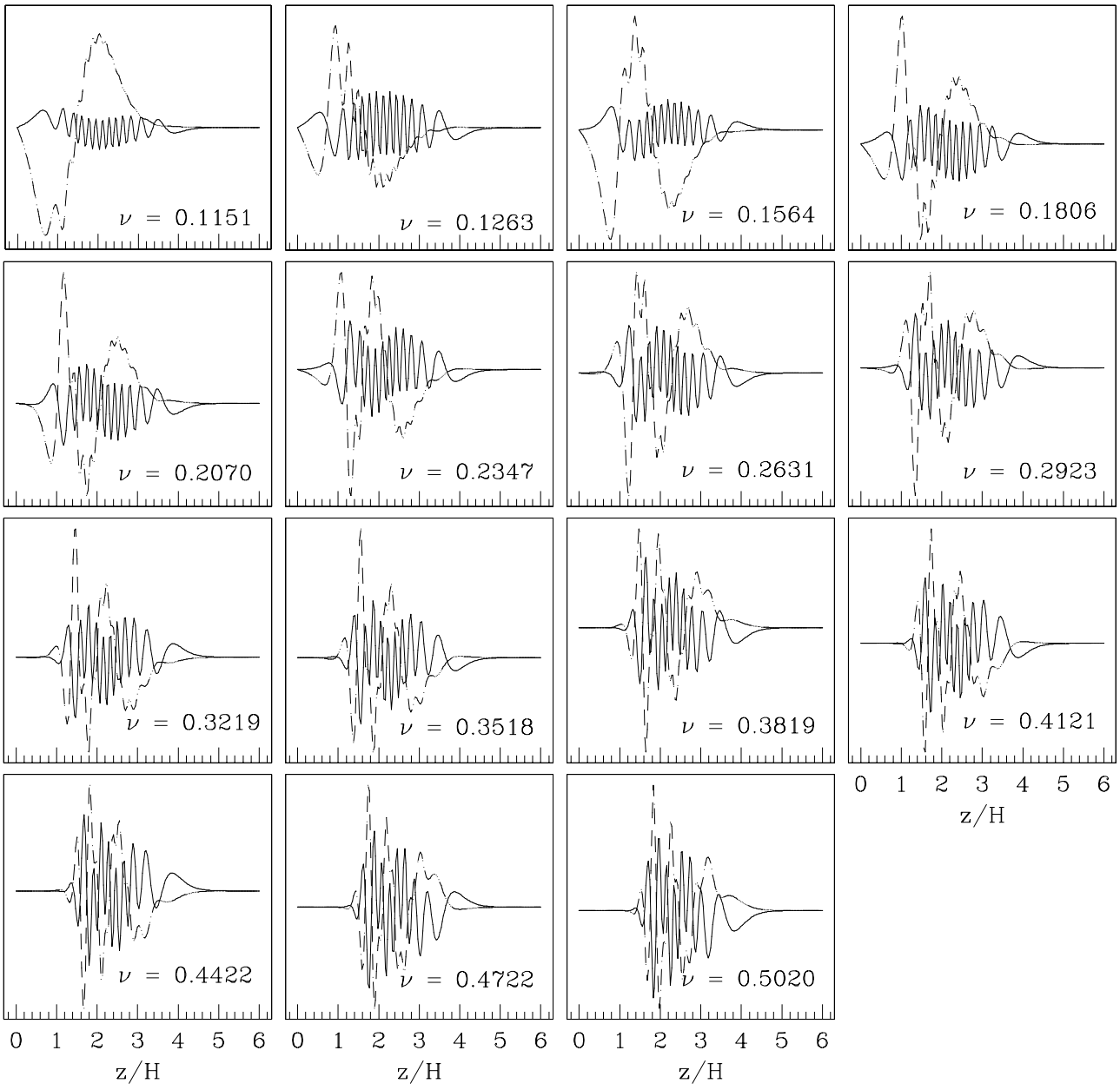

Figure 3.8 Structure of all unstable modes for the fiducial model at $R = 1$ AU and $B = 100$ mG. In each case solid lines show δB_r while dashed ones correspond to δB_ϕ. The growth rate is indicated in the lower right corner of each panel. There are 15 unstable modes, with $0.1151 \leq \nu \leq 0.5020$. Some perturbations grow at the midplane, particularly when $\nu < 0.1806$. Modes growing faster than this show a dead region around the midplane, whose vertical extent increases with the growth rate of the perturbations. Note the asymmetry of δB_r and δB_ϕ about zero, especially in slowly growing modes.

in the weak-field limit, shows no evidence for a minimum required field strength for the instability to grow (see section 3.5.2). A comparison of the structure of the most unstable modes for the fiducial model at $R = 1$, 5 and 10 AU is shown in Fig. 3.9. We display solutions for B from 1 mG, up to the maximum field strength for which unstable modes grow for each radius. Unless stated otherwise, this criterion is followed in all plots that show the structure of the fastest growing modes as a function of B in this study. Note that the maximum value of B is dependent on the disc model, the ionising agents incorporated and radius of interest.

Both the structure and growth rate of these perturbations are shaped by the competing action of different conductivity components, whose relative importance change with height. We defer the analysis of their growth rate to section 3.5.2. Here, we discuss the structure as a function of z. Note first of all that at each radius, the wavelength of the perturbations increase with the magnetic field strength, as expected by both ideal-MHD and non-ideal MHD local analyses (Balbus & Hawley 1991, W99).

At 1 AU (leftmost column of Fig. 3.9), for $B \lesssim 500$ mG, the region next to the midplane is a magnetically inactive zone (Gammie 1996, Wardle 1997). The extent of this region decreases as the field gets stronger. For example, for $B = 1$ mG it extends from the midplane to $z/H \sim 1.8$, but when $B > 500$ mG, there is no appreciable dead region, a result of the stronger magnetic coupling close to the midplane and the relatively small wavenumber of the perturbations. Also, at this radius, when B is relatively strong ($B > 500$ mG), the amplitude of these modes increase with z, a property that is typical of MRI perturbations driven by ambipolar diffusion. Ambipolar diffusion modes have this property because, as the local analysis (W99) indicates, in this limit the local growth of unstable modes increases with the magnetic coupling, which (except in the surface regions) increases with z (see Fig. 3.3). As a result, the local growth rate of the MRI also increases with height in this regime and is able to drive the amplitude of global unstable modes to increase. This explains the shape of the envelope of these modes. Finally, note that when the magnetic field is weak, the perturbations' wavenumber is very high, and δB_r and δB_ϕ are not symmetrical about $z = 0$.

At 5 AU, when $B \gtrsim 100$ mG, perturbations grow even at the midplane. For weaker fields, they exhibit only a very small dead zone which extends to $z/H \lesssim 0.5$. Note also that the envelope of these modes, particularly for $B \gtrsim 100$ mG, is fairly

flat. This is explained by recalling that the magnetic coupling at the midplane in this region is very high ($\chi \sim 90$ for $B = 500$ mG, Fig. 3.5, top panel), so the ideal-MHD approximation holds. Under these conditions, unstable modes peak at the node closest to the midplane, given that the local growth rate is not a strong function of χ and does not vary by much with height (see also top row of Fig. 6 of SW03, which shows similar envelopes for perturbations obtained with $\chi_o = 100$ and different configurations of the conductivity tensor). On the other hand, for $B \lesssim 100$ mG, non-ideal MHD effects are important. When $B = 10$ mG, ambipolar diffusion is dominant for $z/H \lesssim 2.3$. This conductivity term is likely to drive this perturbation's structure, as evidenced by the central dead zone and the envelope peaking at an intermediate height. For $B = 1$ mG, Hall conductivity is dominant close to the midplane ($z/H \lesssim 2$), the region where the envelope of this perturbation peaks. Furthermore, the high wavenumber suggests that its structure is determined by local effects. As a result, Hall conductivity is likely to drive the structure of this mode.

Finally, for $R = 10$ AU there is no appreciable dead zone for $B \gtrsim 10$ mG, given the strong magnetic coupling at this radius. Even for $B = 1$ mG, $\chi_o \sim 3$, a figure that increases to ~ 100 for $B = 100$ mG. As a result, the fluid is in nearly ideal-MHD conditions (see section 3.4.3), which explains the flat envelope of these modes.

Most unstable modes at different radii, excluding cosmic ray ionisation

We also calculated the structure of the most unstable modes at the same three radial positions under the assumption that cosmic rays are excluded from the disc by protostellar winds (Fig. 3.10). In this case the central dead zones at 1 AU ($B \lesssim 100$ mG) extend over a larger cross-section of the disc, given that cosmic rays (when present) are the main source of ionisation near the midplane at this radius (see section 3.4.2). Without them, the electron fraction below $z/H \sim 1.7$ (where x-rays are completely attenuated) plummets, causing the amplitude of MRI perturbations in this section of the disc to be severely reduced. As a result, when $B \lesssim 100$ mG, perturbations are damped for $z/H \lesssim 2$. Another difference with the previous case is noticeable for stronger fields ($B \geq 500$ mG), where before the MRI was active even at the midplane. In this case, the abrupt change in the ionisation balance at the height where x-ray ionisation becomes active, (Fig. 3.1, top panel),

causes the current to be effectively discontinuous there and produces the observed kink in the amplitude of these modes.

In the zone where x-rays are excluded ($z/H \lesssim 1.7$), the main ionising agent is the decay of radioactive elements within the disc. However, they can only produce very weak magnetic coupling. For example, $\chi_o \sim 10^{-8}$ for $B = 1$ mG, and it only increases to $\sim 10^{-3}$ when $B = 1$ G. As a result, the amplitude of the perturbations near the midplane, even for strong fields ($B \gtrsim 500$ mG), is very small at this radius. If the abundance of metals in the gas phase is reduced from the fiducial value adopted here ($\delta_2 \approx 0.02$) to (say) $\sim 2 \times 10^{-3}$, the zone ionised only by radioactivity becomes magnetically dead (as expected). The perturbations' growth is only marginally affected.

For $R = 5$ AU, we also observe a small kink in the perturbations' amplitude for $B \gtrsim 100$ mG. In this case it occurs much closer to the midplane, because at this radius x-rays penetrate to $z/H \sim 0.3$. Finally, for $R = 10$ AU, x-rays penetrate the entire cross section of the disc, so there is no kink in the amplitude of these modes. However, the midplane cosmic ray ionisation rate at this radius is about two orders of magnitude larger than that of x-rays (in fact they dominate over x-rays for $z/H \lesssim 2.5$, see Fig. 3.1, bottom panel), so excluding them does reduce significantly the magnetic coupling in this region. As an illustration of this, note that for $B = 10$ mG, χ_o decreases from ~ 16 in the previous case to only ~ 1 here (see Fig. 3.6). As a result, for $z/H \lesssim 0.3$ the fluid is in the Hall regime while ambipolar diffusion dominates at higher z. Being a high wavenumber perturbation, the structure of this mode reflects mainly local fluid conditions. This explains the shape of its envelope (see rightmost column of Fig. 3.10, second panel from the top): flat envelope close to the midplane where the Hall effect is dominant and amplitude increasing with z at higher vertical locations, driven by ambipolar diffusion. Finally, for $B = 1$ mG, $\chi < |\sigma_1|/\sigma_\perp$ for $z/H < 1.3$. This, together with the high wavenumber of the perturbations, causes Hall diffusion to shape the envelope of this mode.

Conductivity regime comparison ($\sigma_1 B_z > 0$)

It is interesting to compare the structure of the most unstable perturbations obtained with different configurations of the conductivity tensor (assuming that different conductivity regimes dominate over the entire cross section of the disc) against the full

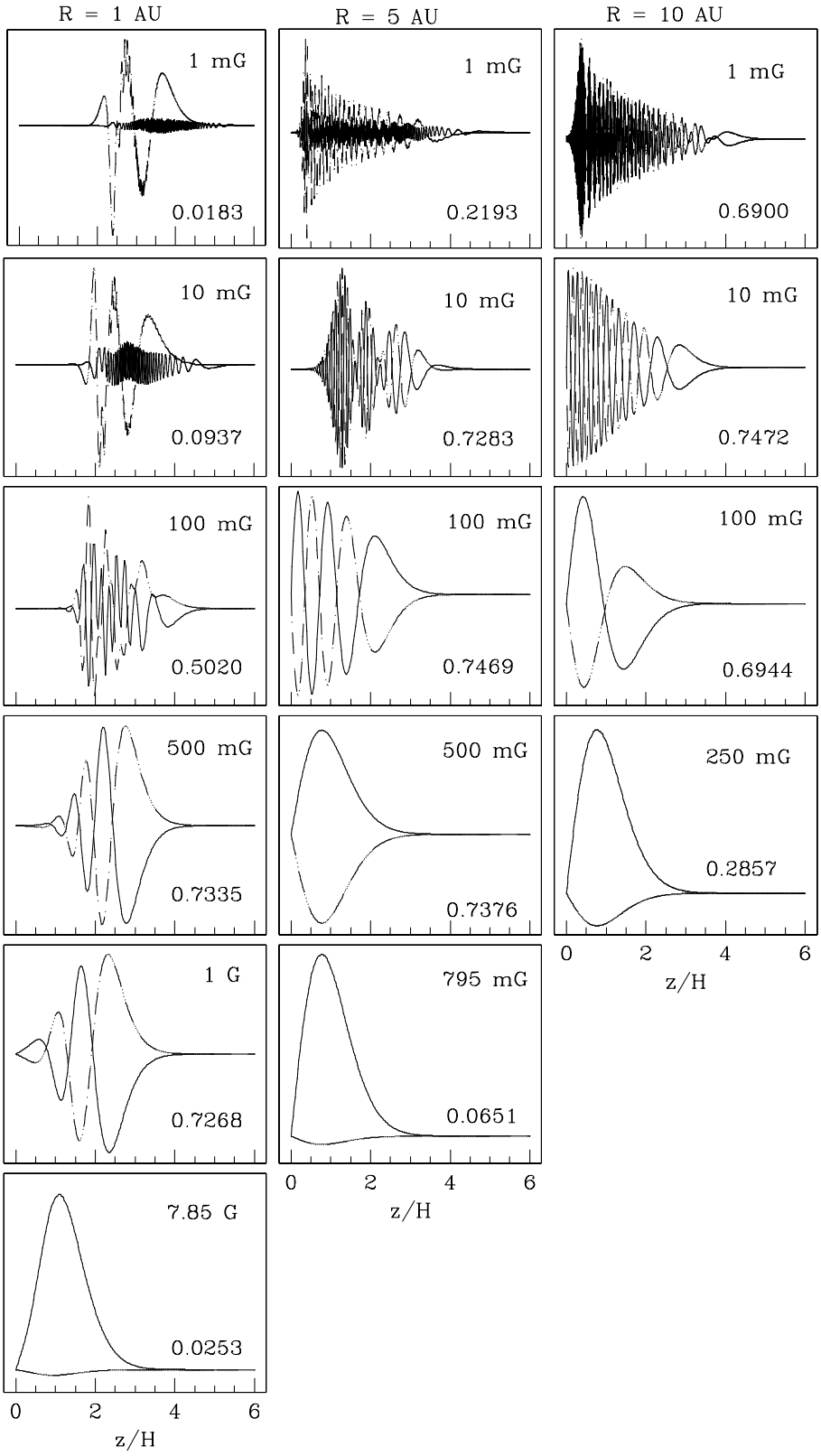

Figure 3.9 Comparison of the structure of the most unstable modes for the fiducial model at $R = 1$, 5 and 10 AU for different choices of the magnetic field strength. B is indicated in the upper right hand of each panel while the growth rate is shown in

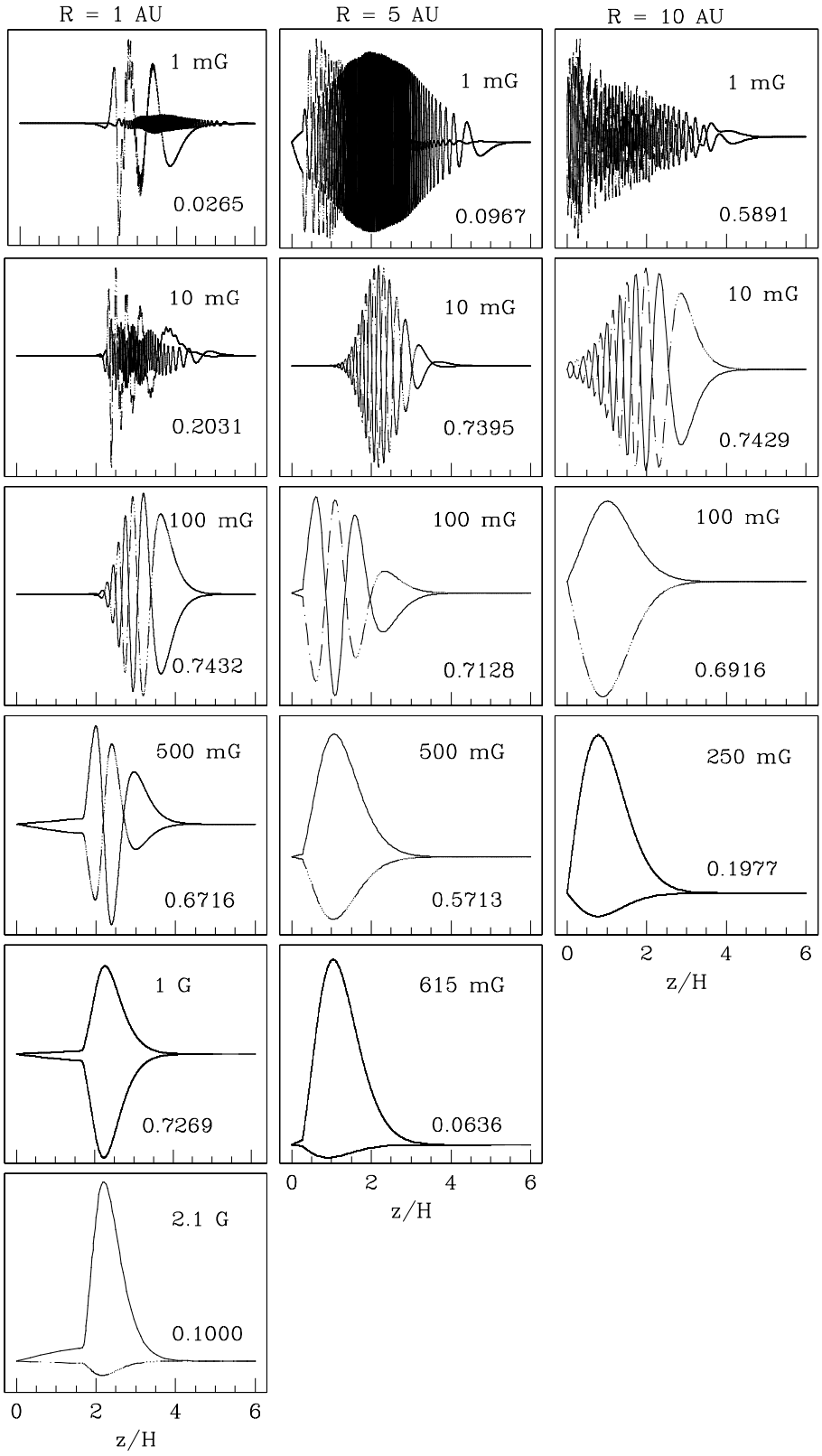

Figure 3.10 As per Fig. 3.9 assuming cosmic rays are excluded from the disc. Note the increased extent of the central dead zone at 1 AU ($B \lesssim 100$ mG) and the kink in the amplitude of the perturbations for stronger fields. This feature is caused by the sharp change in the ionisation balance of the disc at the height where x-ray ionisation becomes

conductivity results discussed in section 3.5.1. This way we can explore more fully the effects of different conductivity components in the overall properties of the instability. Fig. 3.11 presents such solutions for the fiducial model at $R = 1$ AU as a function of the strength of the magnetic field. The left column shows solutions computed with a full conductivity tensor, while the middle and right ones display modes obtained using the ambipolar diffusion ($\sigma_1 = 0$) and Hall regime ($\sigma_2 = 0$, $\sigma_1 B_z > 0$) approximations, respectively.

Note that, for all magnetic field strengths shown here, perturbations computed using the ambipolar diffusion approximation have a more extended central dead zone than modes incorporating a full conductivity tensor. This is in agreement with the local analysis (W99), which showed that the growth of MRI perturbations in the ambipolar diffusion limit decreases steadily with the local magnetic coupling. As a result, the local growth of these modes is severely restricted near the midplane. This is especially effective for weaker fields, when global effects are less important due to the high wavenumber of the perturbations. For example, when $B = 1$ mG, the magnetically dead zone in modes found using the ambipolar diffusion approximation extends to $z/H \sim 2$. The thickness of the dead region decreases for stronger B, but even with $B = 1$ G, there is a small section ($z/H \lesssim 0.5$) in which perturbations do not grow.

Turning now our attention to Hall perturbations, we observe that their amplitude is fairly stable, especially for strong fields ($B \gtrsim 500$ mG), where they show the characteristic flat envelope reported by SW03. When the field is weaker than this, perturbations are damped near the midplane. This is particularly evident for $B <$ 100 mG and is probably related to the fact that at 1 AU the magnetic coupling at the midplane in this limit is very low. Even for $B = 100$ mG, χ_o in the Hall limit $\sim 10^{-4}$ and it decreases to $\sim 10^{-10}$ for $B = 1$ mG (note that these values are significantly smaller than the ones shown in Fig. 3.4, which were obtained with a full conductivity tensor). Local results highlight that the maximum local growth rate of MRI perturbations in the Hall limit is effectively unchanged from the ideal case when $\chi \to 0$ (W99). However, the global analysis presented here shows that when the coupling is very low, the amplitude of global Hall limit perturbations can be damped close to the midplane (see rightmost column of Fig. 3.11, top three panels). On the other hand, there is only a small dead zone for $B \sim 1$ mG, which extends from the midplane to $z/H \sim 0.5$. For stronger fields, there is no appreciable dead

region.

In general, the structure of full σ perturbations reflect the contribution of Hall as well as ambipolar diffusion conductivity terms. When the magnetic field is strong ($B > 100$ mG), ambipolar diffusion is locally dominant over a more extended section of the disc, and the dead zone of perturbations in this limit is smaller than they are for weaker fields. On the other hand, modes in the Hall limit grow now even at the midplane and have a significantly higher wavenumber than ambipolar diffusion perturbations. This is reflected in the structure of full σ modes in this region of parameter space: Their envelope is shaped by ambipolar diffusion (the amplitude increases with height), but the wavenumber is higher and they grow closer to the midplane than pure ambipolar diffusion modes do. This reflects the contribution of the Hall effect. These results are also in agreement with similar trends found with illustrative calculations in SW03.

It was discussed in section 3.4.3 that at this radius (1 AU), Hall conductivity is locally dominant near the midplane for all magnetic field strengths of interest. The transition to the zone where ambipolar diffusion dominates occurs at a lower z for stronger fields (Fig. 3.4, top panel). This analysis reveals that the Hall effect modifies the structure of MRI modes even when Hall diffusion is locally dominant only for a small section close to the midplane of the disc. In section 3.5.2 it will be discussed how the Hall effect also alters the growth of all fastest growing modes at this radius.

At 5 AU, ambipolar diffusion is important in the inner sections of the disc for $B \lesssim 100$ mG (Fig. 3.5). It is expected that perturbations obtained using this approximation will be different from the corresponding full σ modes in this region of parameter space. Fig. 3.12 compares solutions obtained with different configurations of the conductivity tensor at this radius. Ambipolar diffusion modes (left column) are indeed different from full σ ($\sigma_1 B_z > 0$) ones (middle column) when $B \lesssim 100$ mG. For stronger fields, ideal-MHD holds, so the structure of MRI modes computed using different configurations of the conductivity tensor are alike, as expected.

Conductivity regime comparison ($\sigma_1 B_z < 0$)

So far we have discussed solutions obtained with a $\sigma_1 B_z > 0$ Hall conductivity term, which corresponds to the case where the magnetic field and angular velocity vectors

of the disc are parallel ($\mathbf{\Omega} \cdot \mathbf{B} > 0$). We now explore how these results are modified when these vectors are antiparallel.

As noted before, we explored in this case a reduced region of parameter space. In particular, solutions at 1 AU could not be computed at all, as $\chi_o \ll 2$ for all B of interest at this radius, the limit below which all wavenumbers grow in this regime (W99, see also section 3.4.1). On the other hand, results at 10 AU do not differ appreciably in this case from those obtained using a $\sigma_1 B_z > 0$ conductivity, given the strong magnetic coupling throughout the cross-section of the disc at this radial location. At 5 AU, however, Hall diffusion is important for relatively weak fields ($B \lesssim 10$ mG), and both sets of results should be different in this region of parameter space. Fig. 3.12 (middle and right columns) compares the structure of MRI unstable modes computed with a positive and negative Hall conductivity at this radius, as a function of the magnetic field strength. When $\sigma_1 B_z < 0$, no results could be computed for $B < 8$ mG, as $\chi_o < 2$ in these cases. We find that, indeed, for $B = 10$ mG the most unstable mode computed with a negative Hall conductivity has a higher wavenumber, and a slower growth rate, than the corresponding mode with $\sigma_1 B_z > 0$.

More massive disc

To finalise the analysis of the structure of MRI perturbations, we describe now the properties of unstable modes in a more massive disc, as characterised in section 3.2.2. Results are displayed in Fig. 3.13. As expected, the larger column density causes unstable modes to have a more extended central dead zone in relation to results in the minimum-mass solar nebula model. This is particularly noticeable for $R = 1$ AU, where there is now a magnetically inactive zone for $B \lesssim 1$ G. X-rays are excluded from the midplane at this radius (they can only penetrate up to $z/H \sim 2.6$ for this disc model) and the cosmic ray ionisation rate at $z = 0$ is negligible. As a result, even for $B = 1$ G the magnetic coupling at the midplane is $\sim 10^{-4}$, which causes perturbations to be damped at low z. We observe here the same trends discussed in the analysis of the minimum-mass solar nebula model in relation to the structure of these modes. Ambipolar diffusion shapes the envelopes, particularly for strong fields, while Hall diffusion increases their wavenumber in comparison with results in the ambipolar diffusion limit. Finally, note the kink on the amplitude of

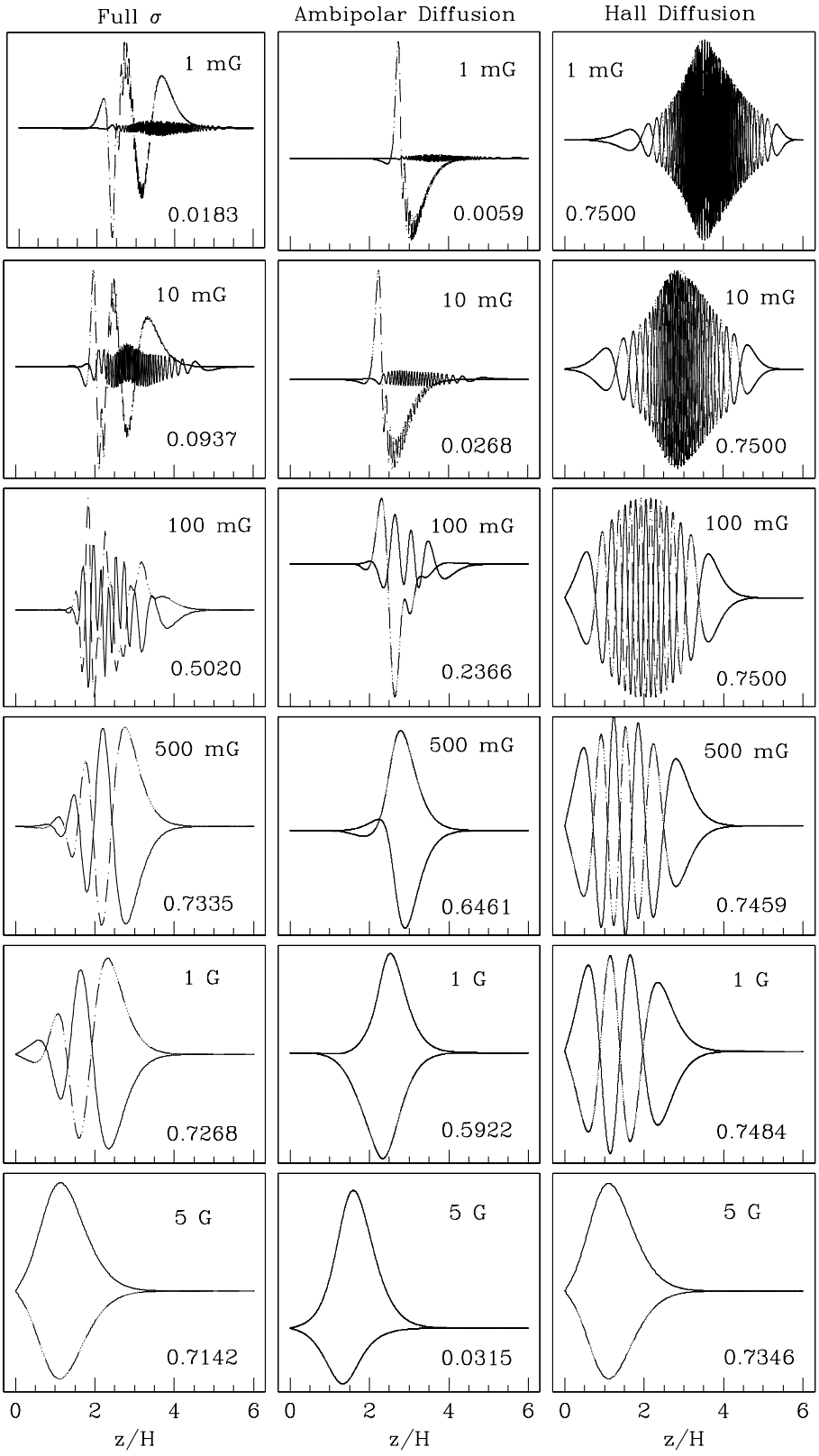

Figure 3.11 Comparison of the structure of the most unstable modes of the MRI for the fiducial model at $R = 1$ AU as a function of the field strength for different configurations of the conductivity tensor. The field strength spans from 1 mG up to 5 G, the maximum

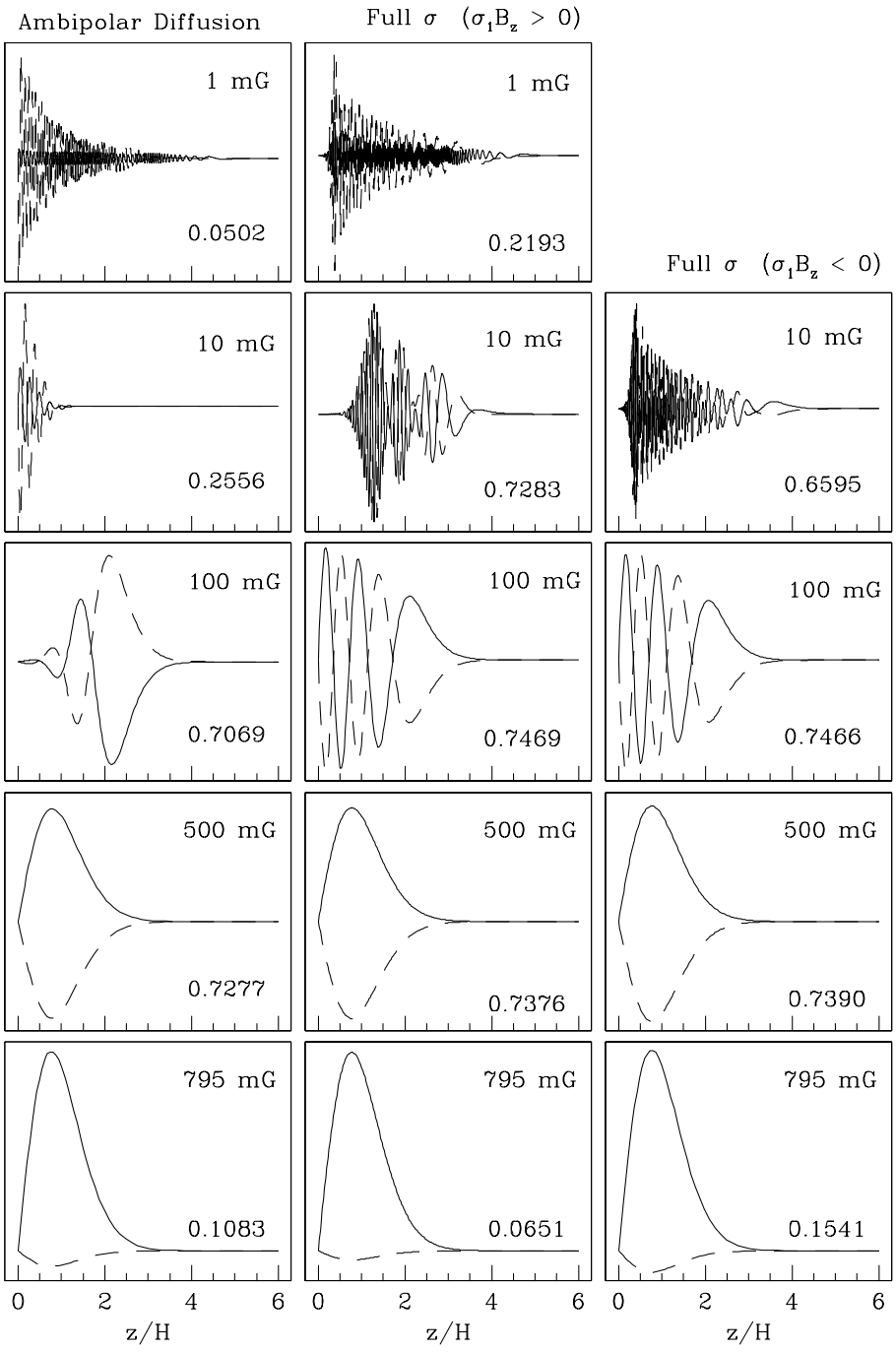

Figure 3.12 Comparison of the structure of the fastest growing modes for the fiducial model at $R = 5$ AU, for different configurations of the conductivity tensor. The left column corresponds to the ambipolar diffusion approximation. The middle and right columns show solutions obtained with a full conductivity tensor when the magnetic field and angular velocity vectors of the disc are parallel ($\sigma_1 B_z > 0$) and antiparallel ($\sigma_1 B_z < 0$), respectively.

the $B = 5.85$ G mode, attributed to the sharp increase in the ionisation fraction at the height where x-ray ionisation becomes active.

At 5 AU, there is also a more extended dead zone, observed up to $B \sim 100$ mG, in comparison with that of perturbations obtained using the minimum-mass solar nebula model. In that case, ideal-MHD conditions held throughout the cross-section of the disc for $B = 100$ mG, with $\chi_o \sim 20$ (see section 3.5.1). On the contrary, in the present model, $\chi_o \sim 0.2$ for this magnetic field strength and ambipolar diffusion is locally dominant for $0.7 \lesssim z/H \lesssim 2$ (see Fig. 3.7, middle panel). As a result, the amplitude of this perturbation increases with z, a typical behaviour of ambipolar diffusion driven MRI, instead of being flat as before.

Finally, for $R = 10$ AU, ideal-MHD conditions hold throughout the disc cross-section for $B \gtrsim 100$ mG (Fig. 3.7, bottom panel). Because of this, the envelopes are flat in this region of parameter space (see Fig. 3.13, right column, lower two panels). On the other hand, when $B \sim 10$ mG, $\chi_o \sim 1.5$ and ambipolar diffusion dominates up to $z/H \sim 2$. As a result, this mode exhibits a small central dead zone and the envelope peaks at an intermediate height. Finally, when $B \sim 1$ mG, $\chi_o \sim 0.05$ and Hall diffusion is dominant for $z/H \lesssim 2$. Consequently, the central dead zone is much reduced, and this perturbation grows closer to the midplane despite the weak magnetic coupling.

3.5.2 Growth rate of the perturbations

Fastest growing modes for different conductivity regimes

The dependency of the growth rate of the most unstable modes with the strength of the magnetic field is shown in Fig. 3.14 for different configurations of the conductivity tensor. Results correspond to the fiducial model at $R = 1$ AU (top panel) and 10 AU (bottom panel). We will use Fig. 3.12 to analyse the corresponding results at 5 AU.

The overall dependency of the ν_{max} vs. B curve for full σ modes is typically as follows: ν_{max} initially increases with B with a $\sim$ power law dependency. It then levels at ~ 0.75, the maximum growth rate for ideal-MHD perturbations in Keplerian discs. Eventually, the maximum growth rate decays sharply at a characteristic magnetic field strength at which the perturbations' wavelength is $\sim H$, the scaleheight of the disc. Note that in the weak-field limit, the dependency of the ν_{max} vs. B curve

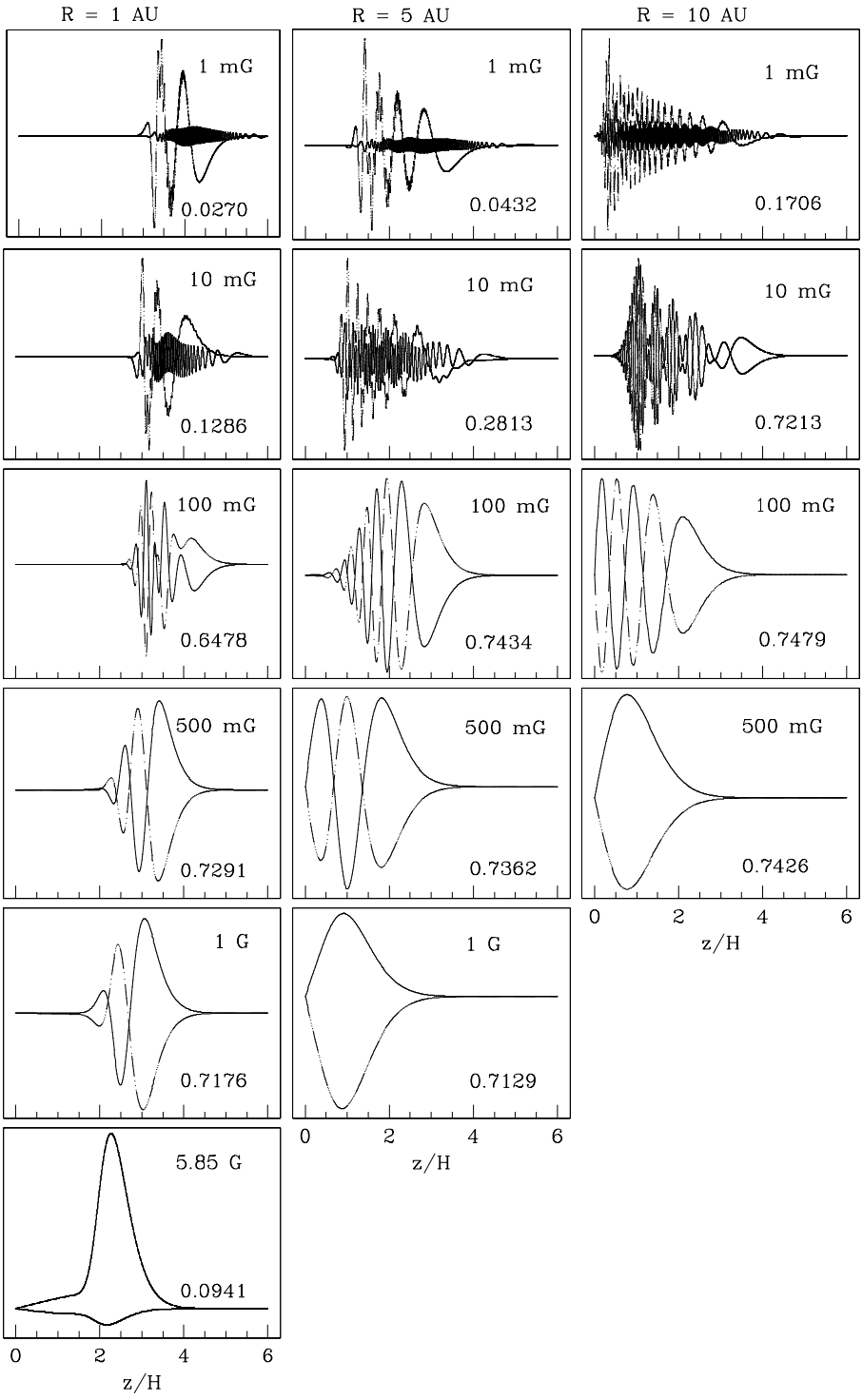

Figure 3.13 Comparison of the structure of the most unstable modes of the MRI for a more massive disc, incorporating cosmic ray ionisation. We present results at $R = 1$, 5 and 10 AU as a function of the strength of the magnetic field. The disc surface and mass density are $\Sigma_o^{'} = 10\Sigma_o$ and $\rho_o^{'} = 10\rho_o$. For simplicity, it was assumed that the temperature, sound speed and scale height are unchanged from those of the minimum-mass solar nebula model. Note that these modes have a more extended central dead zone, especially for $R = 1$ AU,

shows no evidence of a minimum field strength, below which modes do not grow. This characteristic shape of the ν_{max} vs. B curve can be explained in terms of the dependency of the perturbations' growth rate with B when different conductivity components are dominant at different heights.

Examining Fig. 3.14 (top panel), it is clear that for weak fields ($B \lesssim 200$ mG), perturbations computed with a full σ have a ν_{max} vs. B dependency similar to that of solutions obtained using the ambipolar diffusion approximation. This indicates that this feature is driven by ambipolar diffusion. In this limit, the local maximum growth rate of MRI modes increases with the magnetic coupling (W99), which in turn, increases with B, except when β_i and $|\beta_e| \gg 1$ (e.g. near the surface). As a result, ν_{max} should increase with B, as observed. On the contrary, when the magnetic field is stronger than ~ 200 mG, the growth rate of MRI modes obtained with a full conductivity tensor is practically identical to that of Hall limit modes. In this region of parameter space, the growth rate of global modes remains unchanged when the magnetic field gets stronger, as expected when Hall diffusion drives the growth of the instability. Eventually, B becomes strong enough that the fastest growing mode becomes $\sim$ the scaleheight of the disc, and the growth rate rapidly declines. These results are in agreement with previous findings by W99 and SW03.

Note also that the maximum growth rate of perturbations in the Hall limit does not change appreciably with B, until they are damped for a sufficiently strong field, as expected. In fact, Hall perturbations grow at $\sim$ the ideal-MHD rate even for $B \sim 1$ mG.

Hall diffusion is locally dominant at 1 AU in the lower sections of the disc for all magnetic field strengths for which unstable modes exist (Fig. 3.4, top panel). As a result, perturbations obtained with a full conductivity tensor grow significantly faster than modes found using the ambipolar diffusion approximation for all B.

For $R = 5$ AU, the Hall effect increases the growth rate of full σ perturbations when $B \lesssim 10$ mG, the region of parameter space where Hall diffusion is locally dominant near the midplane (compare the growth rates in left and middle columns of Fig. 3.12). Moreover, full σ modes computed with $\sigma_1 B_z > 0$ (middle column) and $\sigma_1 B_z < 0$ (right column) grow at different speeds and have different structure, as expected in the region where Hall diffusion dominates.

Finally, Fig. 3.14 (bottom panel) displays the growth rate of the most unstable modes at 10 AU. Results were computed with a full conductivity tensor – but with

opposite signs of $\mathbf{\Omega} \cdot \mathbf{B}$ –, as well as using the ambipolar diffusion approximation. In this case, Hall diffusion is locally unimportant for all B studied here, so the sign of $\sigma_1 B_z$ does not affect the growth of the perturbations. On the other hand, at this radius, ambipolar diffusion is important for $B \lesssim 10$ mG. This slows the growth of perturbations in the ambipolar diffusion limit when the magnetic field is weaker than this value.

Fastest growing modes at different radii

We also compare the growth rate of the most unstable modes at different radii as a function of the strength of the magnetic field (Fig. 3.15). Three sets of results are displayed. The first two correspond to the minimum-mass solar nebula disc assuming cosmic rays either penetrate the disc (top panel) or are excluded from it (middle panel). The last set presents results for the more massive disc model (bottom panel), incorporating cosmic ray ionisation. Note that in all three cases, MRI perturbations grow over a wide range of magnetic field strengths.

The maximum field strength for which unstable modes exist (within each panel), is weaker at larger radii. In ideal-MHD conditions, as well as when either the ambipolar diffusion or Hall ($\sigma_1 B_z > 0$) conductivity regimes dominate, unstable MRI modes are damped when $v_A/c_s \sim 1$ (Balbus & Hawley 1991), which corresponds to $\lambda \sim H$. In the Hall ($\sigma_1 B_z < 0$) limit, unstable modes have been found for $v_A/c_s \sim 3$ (SW03, albeit using a constant conductivity profile). In any case, as both the gas density (eq. 3.26) and the sound speed (eq. 3.17) decrease with radius, the ratio of the Alfvén to sound speed associated with a particular magnetic field strength increases with R, and as a result, the perturbations are damped at a weaker field for larger radii.

The maximum magnetic field strengths for which MRI unstable modes grow, as well as the range for which $\nu_{max} \sim$ the ideal-MHD rate, are summarised in Table 3.1 for the radii and disc structures of interest here. Note that for the fiducial model, we obtained unstable modes at 1 AU for $B \lesssim 8$ G. The growth rate is of the order of the ideal-MHD rate ($\nu = 0.75$) for 200 mG $\lesssim B \lesssim 5$ G.

When cosmic rays are assumed to be excluded from the disc (see middle panel of Fig. 3.15 and central two columns of Table 3.1), unstable modes are obtained at 1 AU only for $B \lesssim 2$ G. The corresponding range at 5 AU is only slightly reduced and

Table 3.1 Magnetic field strengths for which MRI perturbations grow at 1, 5 and 10 AU for different disc models and sources of ionisation. For the minimum-mass solar nebula disc, two sets of results are shown, where cosmic rays are either present or excluded from the disc. For the massive disc model, only the former case is presented. Columns labeled 'B_{max}' list the maximum value of B for which each disc supports unstable MRI modes. Similarly, the '$B(\nu \sim 0.75)$' columns specify the subset of these for which perturbations grow at nearly the ideal-MHD rate ($\nu \sim 0.75$).

	Minimum-mass solar nebula				Massive Disc	
	ζ_{CR} included		ζ_{CR} excluded		ζ_{CR} included	
Radius (AU)	B_{max}	$B(\nu \sim 0.75)$	B_{max}	$B(\nu \sim 0.75)$	B_{max}	$B(\nu \sim 0.75)$
1	7.85	0.2 - 5	2.10	0.1 - 1	5.85	0.2 - 0.5
5	0.80	0.02 - 0.5	0.62	0.01 - 0.05	2.36	0.05 - 0.5
10	0.25	0.002-0.05	0.25	0.005 - 0.05	0.82	0.01 - 0.5

it is essentially the same as before at 10 AU. This is consistent with our expectation that cosmic rays are a particularly important source of ionisation at 1 AU, where x-rays are excluded from the midplane. In this case, $\nu_{max} \sim 0.75$ at 1 AU for 100 mG $\lesssim B \lesssim$ 1 G.

In the massive disc model (bottom panel of Fig. 3.15 and two rightmost columns of Table 3.1), the MRI is active at 1 AU for $B \lesssim 6$ G and $\nu_{max} \sim 0.75$ for 200 mG $< B <$ 500 mG. For $R = 5$ and 10 AU, MRI unstable modes exist in this disc for stronger fields than in the minimum-mass solar nebula model. This can be explained by recalling that the larger mass and column density translates, at these radii, into a larger gas pressure and a stronger equipartition magnetic field strength at the midplane. MRI modes are, as a result, damped for a stronger field than they are in the minimum-mass solar nebula model. On the contrary, for $R = 1$ AU, the range of magnetic field strengths over which perturbations grow does not change appreciably, given the shielding of the inner sections at this radius.

3.6 Discussion

In this paper we have explored the vertical structure and linear growth of MRI perturbations of an initially vertical magnetic field, using a realistic ionisation profile

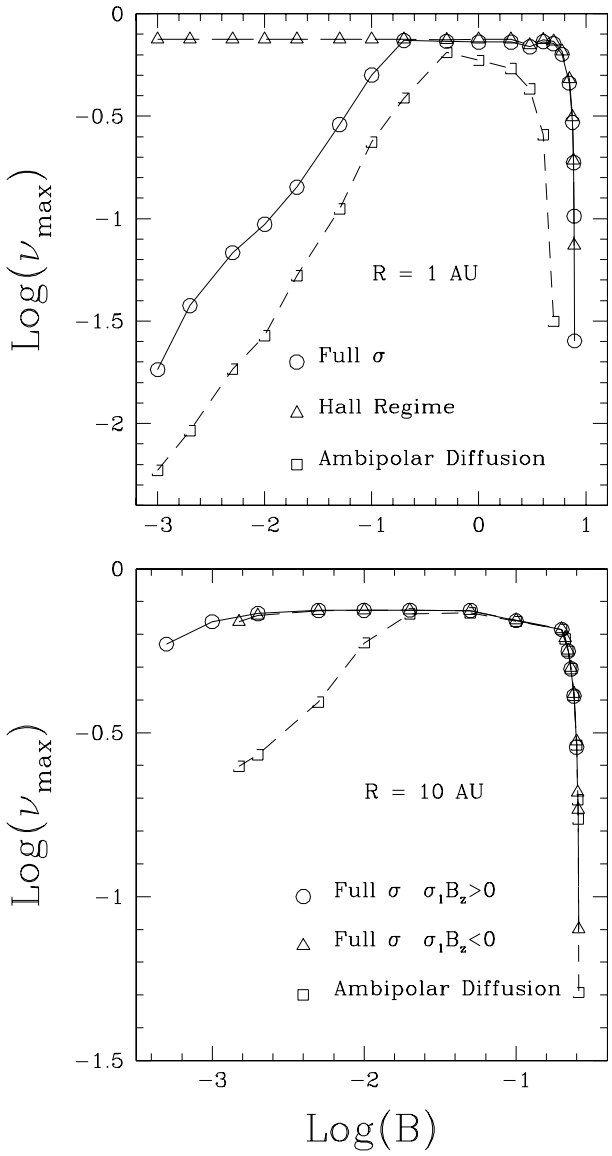

Figure 3.14 Growth rates of the fastest growing modes as a function of the strength of the magnetic field for different configurations of the conductivity tensor. Results are presented at $R = 1$ AU (top panel) and 10 AU (bottom panel) for the fiducial model. It is evident that at 1 AU, when the magnetic field is weak ($B \lesssim 200$ mG), perturbations are driven by ambipolar diffusion. As a result, ν_{max} increases with B. As the field gets even stronger, the maximum growth rate of full σ and Hall limit perturbations are practically identical, signalling that Hall conductivity determines the growth of global unstable modes in this region of parameter space. Finally, ν_{max} decreases rapidly when B is so strong that the wavelength of the fastest growing mode is $\sim$ the scaleheight of the disc.

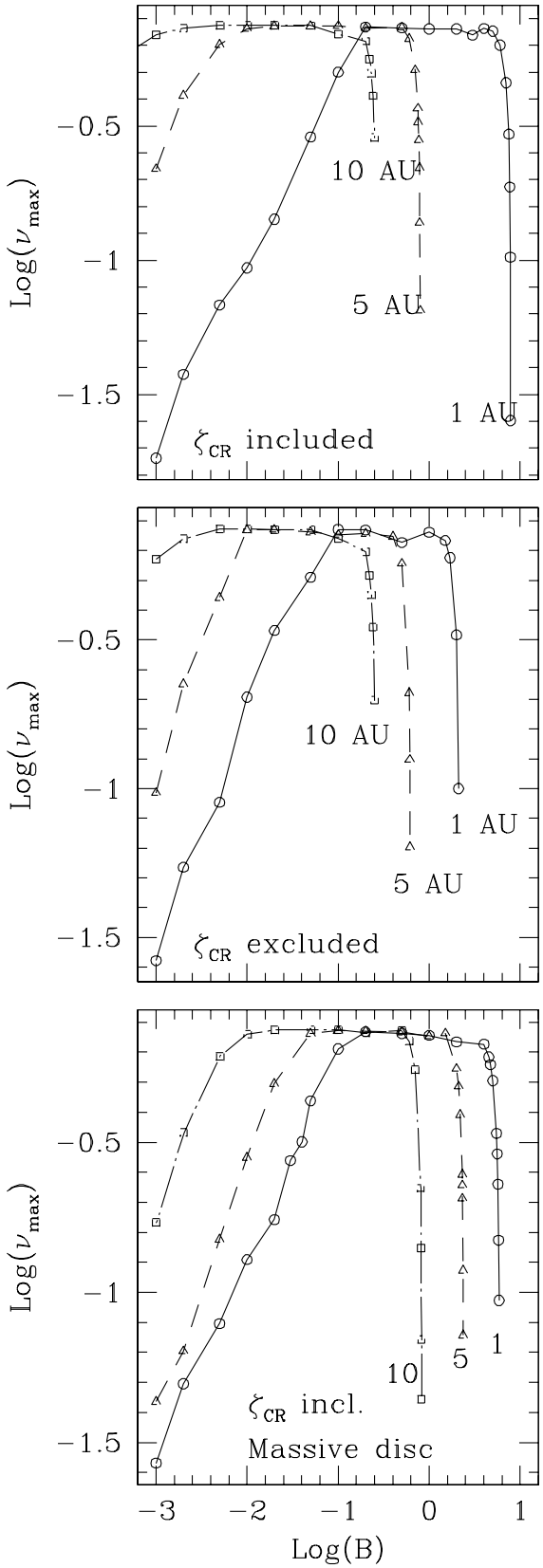

Figure 3.15 Growth rate of the most unstable modes of the MRI for $R = 1$, 5 and 10 AU as a function of the strength of the magnetic field. Top and middle panels show results obtained with the fiducial model, assuming cosmic rays are either included, or

and assuming that ions and electrons are the sole charge carriers. This formulation is appropriate to model low conductivity discs (Gammie & Menou 1998; Menou 2000; Stone et al. 2000) at late stages of accretion, after dust grains have settled into a thin layer around the midplane ($\sim 10^5$ years, Nakagawa et. al. 1981, Dullemond & Dominik 2004) and become dynamically uncoupled from the gas at higher z. Solutions were obtained at 1, 5 and 10 AU from the central object as a function of the strength of the magnetic field for different configurations of the conductivity tensor, disc model and sources of ionisation.

We have shown that the magnetic field is dynamically important in low conductivity accretion discs over a wide range of field strengths. An example of this activity is the generation and sustaining of MRI-unstable modes, which are thought to be required to provide the angular momentum transport for accretion to proceed. The structure and growth rate of MRI perturbations are a function of the disc properties and the strength of the field. For a particular radius and disc model, they are a result of the competing action of different dominant conductivity components at different heights.

For $R \sim$ a few AU and relatively weak fields ($B \lesssim 100$ mG at 1 AU or $B \lesssim 1$ mG at 5 AU), the fluid close to the midplane is in the Ohmic conductivity regime ($\sigma_\parallel \sim \sigma_2 \gg |\sigma_1|$, e.g. see Fig. 3.3). Conversely, for larger radii (or stronger fields) Hall conductivity dominates even at $z = 0$ (Wardle, in preparation; see also section 3.4.3). Ambipolar diffusion dominates above this region until $\chi \sim 10$ (W99). For still higher z, the magnetic coupling is so strong that ideal-MHD holds. The heights at which these transitions take place, for a particular disc model and radial position, are a function of the strength of the magnetic field. Note that even when $|\sigma_1| \ll \sigma_2$, Hall diffusion still dominates the structure and growth of MRI modes when $\chi \lesssim \chi_{crit} \equiv |\sigma_1|/\sigma_\perp$ (SW03).

At 1 AU, for the fiducial model, unstable modes exist for $B \lesssim 8$ G. For a significant subset of these strengths (200 mG $\lesssim B \lesssim 5$ G), perturbations grow at about the ideal-MHD rate ($= 0.75\Omega$ in Keplerian discs). At this radius, Hall diffusion is locally dominant near the midplane for all magnetic field strengths for which MRI unstable modes exist. As a result, modes computed with a full conductivity tensor have a higher wavenumber, and grow faster, than perturbations obtained using the ambipolar diffusion approximation. On the other hand, ambipolar diffusion shapes the envelopes of these modes (especially for strong fields), causing them to peak at

an intermediate height, instead of having the characteristic flat envelope that modes in the Hall limit have for these field strengths.

Cosmic rays are an important source of ionisation at 1 AU, given that x-rays do not reach the midplane at this radius (see Fig. 3.1). Consequently, if they are assumed to be excluded from the disc, the extent of the magnetically inactive 'dead zone' about the midplane increases and unstable modes grow only for $B \lesssim 2.1$ G. Furthermore, under this assumption, perturbations obtained with a relatively strong initial magnetic field (e.g. $B \gtrsim 500$ mG), exhibit a kink in their amplitude. This feature is attributed to the sharp increase in the ionisation fraction at the height where x-ray ionisation becomes active. Finally, for the massive disc model ($\Sigma_o^{'} = 10\Sigma_o$ and $\rho_o^{'} = 10\rho_o$, incorporating cosmic ray ionisation), the central dead zone extends to a higher z at 1 AU, as the larger column density associated with this model causes the ionisation fraction at low z to drop sharply (the disc is shielded from x-rays below $z/H \approx 2.6$ and even the cosmic ray ionisation rate at the midplane is negligible). MRI perturbations grow in this case for $B \lesssim 6$ G, a range not significantly different from that of results in the fiducial model. This is the case because the effective surface density is largely unchanged, given the shielding of the inner sections.

At 5 AU, for the fiducial model, MRI-unstable modes grow for $B \lesssim 800$ mG. When 20 mG $\lesssim B \lesssim 500$ mG, the growth rate is $\sim 0.75\Omega$. At this radius, Hall diffusion increases the growth rate and wavenumber of unstable modes for $B \lesssim 100$ mG, but for stronger fields, perturbations obtained with different configurations of the conductivity tensor have similar structures and growth rates, a signal that ideal-MHD conditions hold (Fig. 3.12). We also conducted an analysis of the effect of the alignment of the magnetic field and the angular velocity vector of the disc. Results indicate that, at this radius, the sign of $\sigma_1 B_z$ is important for $B \lesssim 10$ mG, the range of magnetic field strengths for which Hall diffusion is locally dominant at low z. As in the 1 AU case, excluding cosmic rays reduces the range of magnetic field strengths for which MRI modes grow (unstable modes are found for $B \lesssim 600$ mG in this case) and there is a kink in the amplitude of the perturbations for $B \gtrsim 100$ mG. Finally, when the surface density of the disc is increased, the central dead zone occupies a larger cross-section, as expected, and unstable modes are found for stronger fields than in the fiducial model. This is a result of the stronger equipartition magnetic field strength for this disc model at this radial position.

At 10 AU, the MRI is active for $B \lesssim 250$ mG and the growth rate is close to the ideal-MHD rate for 2 mG $\lesssim B \lesssim$ 50 mG. Furthermore, for $B \lesssim 10$ mG, perturbations obtained with a full conductivity tensor grow significantly faster than modes in the ambipolar diffusion limit, which reflects the contribution of the Hall effect (Fig. 3.14, bottom panel). At this radius, when cosmic rays are excluded, the range of magnetic field strengths for which unstable modes exist is not affected, given that x-rays are able to penetrate to the midplane. In the more massive disc, the extent of the dead zone increases, especially for weak fields ($B \lesssim 10$ mG) and perturbations grow for stronger fields than in the minimum-mass solar nebula disc.

The results just presented demonstrate how the properties of global (in the z direction) MRI unstable modes are dependent on the competing action of different conductivity regimes dominating at different heights. When the wavenumber is high, global effects – driven by the stratification of the disc – are less important and the modes' structure is largely determined by local fluid conditions. In agreement with our previous paper (SW03), we find that in this case, perturbations driven by Hall diffusion peak closer to the midplane than those where ambipolar diffusion is the dominant diffusion mechanism. Conversely, when global effects are important, the envelope of the perturbations is shaped by ambipolar diffusion while the Hall effect, which is typically important close to the midplane, increases the wavenumber and growth rate of the perturbations.

In section 2.1 it was discussed why the MRI is one of the most promising mechanisms to generate and sustain the angular momentum transport required for disc material to accrete. The angular momentum flux associated with the fastest growing mode in the linear regime is given by,

$$L = \rho Re(\delta v_r) Re(\delta V_\phi) - \frac{Re(\delta B_r) Re(\delta B_\phi)}{4\pi}\,, \tag{3.69}$$

where the two terms in the right hand side correspond to transport via Reynolds and Maxwell stresses, respectively. The vertical profile of this quantity turns out to be a good indicator of the vertical sections where angular momentum is transported once the instability becomes non-linear. This is so because the fastest growing mode in the linear regime is also an exact solution to the full non-linear fluid equations in the incompressible limit (Goodman & Xu 1994). Given this, and the importance of this transport mechanism for accretion, we present in Fig. 3.16 the angular momentum

flux (equation 3.69) associated with the modes shown in Fig. 3.9. Note that the regions where no angular momentum is being transported correspond well with the 'dead zones' (understood as the regions where $\delta B_r \approx \delta B_\phi \approx 0$) identified in that figure. This is expected, given that the MRI transports angular momentum mainly via magnetic stresses. At 1 AU, a magnetically inactive zone is observed for $B \lesssim 1$ G, while for larger radii even regions close to the midplane are active. These results are consistent with angular momentum being transported radially outwards by the MRI, in the inner regions of discs, for a wide range of magnetic field strengths and fluid conditions.

In the present formulation, it was assumed that ions and electrons are the only charge carriers. As discussed earlier, this is valid in late evolutionary stages of accretion, when dust grains have sedimented enough towards the midplane that they can be neglected when studying the dynamics of the gas at higher z. If grains are well mixed with the gas, however, recombinations on dust surfaces are expected to be dominant and $n_e \ll n_i$ (e.g. Wardle 2003, Desch 2004). The settling of dust grains is, consequently, a crucial factor in the overall equilibrium structure of discs. The timescale for this settling to occur is expected to be affected by MHD turbulence. Although in quiescent discs dust grains may quickly settle into a thin sub-layer about the midplane, the vertical stirring caused by MHD turbulence could potentially transport them back to higher vertical locations, preventing them from settling below a certain height (Dullemond & Dominik 2004 and references therein). It is also likely that the transition between vertical sections where dust grains are well mixed with the gas phase and those completely depleted of grains by settling is not 'extremely sharp' (Dullemond & Dominik 2004). The efficiency of this stirring is dependent on the disc being able to support MHD turbulence in the vertical locations where dust grains are present. On the other hand, dust grains can reduce the abundance of free electrons, and the efficiency of MHD turbulence itself, by providing additional recombination pathways on their surfaces. This, in turn, will reduce the vertical extent of the magnetically active regions, and the angular momentum flux through the disc. Ultimately, the equilibrium structure, and magnetic activity, of accretion discs will reflect the complex interplay between all these processes.

It is expected that the structure and growth of MRI unstable modes in such environments will be affected by the dependency of the ionisation balance with height in

the presence of chemistry taking place on grain surfaces. The study of the properties of the MRI in a disc where dust dynamics and evolution are determined consistently, and where Hall conductivity is taken into account, is essential to understand more fully the presence and efficiency of MRI-driven angular momentum transport in accretion discs. Non-ideal MHD simulations that explore the MRI non-linear stages as outlined above are of particular interest. Nevertheless, from the results presented in this paper, it is clear that Hall diffusion is crucial for the realistic modelling of the magnetorotational instability in protostellar discs, particularly at a distance of $\sim$ a few AU from the central object. More generally, Hall conductivity is an important factor when studying the magnetic activity of low conductivity discs at these radii.

3.7 Summary

We have presented in this paper the vertical structure and linear growth of the magnetorotational instability (MRI) in weakly ionised, stratified accretion discs, assuming an initially vertical magnetic field. Both the density and the conductivity are a function of height. Moreover, the conductivity is treated as a tensor and obtained with a realistic ionisation profile. Two disc models were explored: The minimum-mass solar mebula disc (Hayashi 1981; Hayashi, Nakagawa & Nakazawa 1985) and a more massive disc, with the mass and surface density increased by a factor of 10.

This formulation is appropriate for the study of weakly ionised astrophysical discs, where the ideal-MHD approximation breaks down (Gammie & Menou 1998; Menou 2000; Stone et al. 2000). The ionisation sources relevant here, outside the inner 0.1 AU from the central object, are non-thermal: Cosmic rays, x-rays and radioactive decay. For the minimum-mass solar nebula model we compare solutions obtained including all three sources of ionisation with those arrived at assuming that cosmic rays are excluded from the disc by the protostar's winds. Recombination processes are taken to occur in the gas-phase only, which is consistent with the assumption that dust grains have settled into a thin layer about the midplane, and ions and electrons are the only charge carriers. Perturbations of interest have vertical wavevectors ($k = k_z$) only, which are the most unstable modes (when initiated from a vertically aligned magnetic field) in both the Hall and Ohmic regimes (Balbus & Hawley 1991; Sano & Miyama 1999). This is not necessarily the case in the

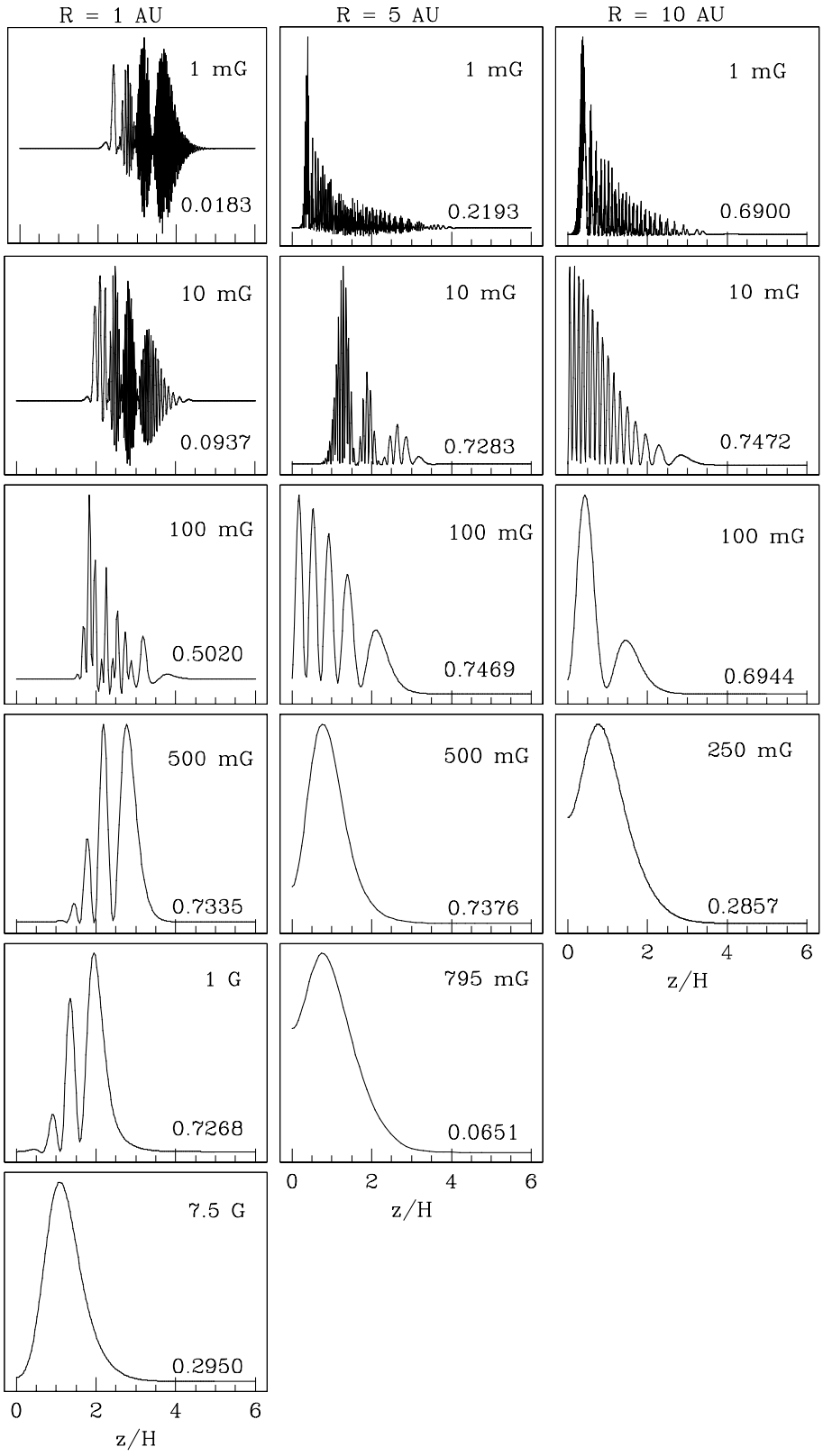

Figure 3.16 Angular momentum flux L (see equation 3.69) associated with each of the modes presented in Fig. 3.9. At 1 AU, there is a central 'dead zone' for $B \lesssim 1$ G. For larger radii, even regions close to the midplane are actively transporting angular momentum radially outwards. Note L goes to zero at large z/H in all panels.

ambipolar diffusion limit (Kunz & Balbus 2004, Desch 2004), where the fastest growing modes can have radial as well as vertical wavenumbers. Under the adopted approximations, the properties of the MRI in the ambipolar diffusion and Ohmic conductivity limits are identical.

Three parameters were found to control the dynamics and evolution of the fluid: (*i*) the local ratio of the Alfvén to sound speed (v_A/c_s); (*ii*) The local coupling between ionised and neutral components of the fluid (χ), which relates the frequency at which non-ideal effects are important with the dynamical (Keplerian) frequency of the disc; and (*iii*) the ratio of the components of the conductivity tensor perpendicular to the magnetic field (σ_1/σ_2), which characterises the conductivity regime of the fluid. These parameters were evaluated at $R = 1$, 5 and 10 AU for a range of magnetic field strengths. The linearised system of ODE was integrated from the midplane to the surface of the disc under appropriate boundary conditions and solutions were obtained for representative radial locations of the disc as a function of the magnetic field strength and for different configurations of the conductivity tensor.

The main results of this study are summarised below.

1. For the minimum-mass solar nebula model, incorporating cosmic ray ionisation (the fiducial model):

   At 1 AU, unstable MRI modes exist for $B \lesssim 8$ G. When 200 mG $\lesssim B \lesssim 5$ G, the most unstable modes grow at $\sim$ the ideal-MHD rate ($= 0.75\Omega$). Hall diffusion dominates the structure and growth rate of unstable modes for all magnetic field strengths for which they grow. For strong fields, ambipolar diffusion shapes the envelope of the perturbations, which peak at an intermediate height. Finally, at this radius, a magnetically dead zone (Gammie 1996, Wardle 1997) exists when $B < 1$ G. As expected, the vertical extent of this zone decreases when the magnetic field gets stronger. It increases when a more massive disc model is used.

   At 5 AU, MRI-unstable modes grow for $B \lesssim 800$ mG and the growth rate is close to the ideal MHD rate for 20 mG $\lesssim B \lesssim 500$ mG. Perturbations incorporating Hall conductivity have a higher wavenumber and grow faster than solutions in the ambipolar diffusion limit for $B \lesssim 100$ mG. When $B \lesssim$ 10 mG, the structure and growth of full σ perturbations are dependent on

the alignment of the magnetic field and angular velocity vectors of the disc. Unstable modes grow even at the midplane for $B \geq 100$ mG but for weaker fields, a small dead region exists.

At 10 AU, the MRI is active for $B \lesssim 250$ mG. The growth rate is close to the ideal-MHD rate for 2 mG $\lesssim B \lesssim 50$ mG and when $B \lesssim 10$ mG, perturbations obtained with a full conductivity tensor grow significantly faster than modes in the ambipolar diffusion limit. Modes show only a very small dead region when $B \sim 1$ mG.

2. When the magnetic field is weak (e.g. $B \lesssim 200$ mG at 1 AU), the maximum growth rate of unstable MRI modes (ν_{max}) increases with the strength of the magnetic field, a feature driven by ambipolar diffusion.

3. When cosmic rays are assumed to be excluded from the disc, unstable modes at 1 AU grow only for $B \lesssim 2.1$ G. Results at 5 AU only change slightly, while solutions at 10 AU are not affected at all, as expected.

4. For the massive disc model ($\Sigma_o^{'} = 10\Sigma_o$ and $\rho_o^{'} = 10\rho_o$, incorporating cosmic ray ionisation), MRI perturbations grow for stronger fields at 5 and 10 AU, in relation to the minimum-mass solar nebula model. Results at 1 AU are unchanged, given that in this case the effective surface density is not significantly different.

MRI perturbations grow in protostellar discs for a wide range of fluid conditions and magnetic field strengths. Hall diffusion largely determines the structure and growth rate of perturbations at radii of order of a few AU from the central protostar. This indicates that, despite the low magnetic coupling, the magnetic field is dynamically important in low conductivity astrophysical discs and will impact the dynamics and evolution of these discs.

Chapter 4

Impact of dust grains

Impact of dust grains

4.1 Introduction

The role magnetic fields are able to play in the dynamics and evolution of low conductivity discs is largely determined by the degree of coupling between the field and the neutral gas. This magnetic coupling reflects the equilibrium between ionisation and recombination processes taking place in the disc. In protostellar discs, ionisation processes outside the innermost sections ($R \gtrsim 0.1$ AU) are non-thermal, driven by interstellar cosmic rays, x-rays emitted by the central protostar and the decay of radioactive materials (Hayashi 1981; Glassgold, Najita & Igea 1997; Igea & Glassgold 1999; Fromang, Terquem & Balbus 2002). On the other hand, free electrons are lost through recombination processes which, in general, take place either in the gas phase (through the dissociative recombination of electrons with molecular ions and the radiative recombination with metal ions) or on grain surfaces (e.g. Nishi, Nakano & Umebayashi 1991).

Dust grains affect the level of magnetic coupling in protostellar discs when they are well mixed with the gas (e.g. in relatively early stages of accretion and/or when turbulence prevents them from settling towards the midplane). They do so in two ways. First, they reduce the ionisation fraction by providing additional pathways for electrons and ions to recombine on their surfaces. Second, charged dust particles can be important charged species in high density regions (Umebayashi & Nakano 1990; Nishi, Nakano & Umebayashi 1991). For example, at 1 AU in a disc where 0.1μm

grains are present, positively charged grains are the most abundant ionised species within two scaleheights from the midplane (Wardle in prep.). As dust particles generally have large cross sections, collisions with the neutrals are important and they become decoupled (or partially decoupled) to the magnetic field at densities for which smaller species, typically ions and electrons, would still be well tied to it.

Both of these mechanisms act to lower the conductivity of the fluid, especially near the midplane where the density is high and ionisation processes are inefficient (in the minimum-mass solar nebula disc, for example, x-rays are completely attenuated below $z/H \sim 1.7$; see Fig. 3.1). As a result, in the inner sections of the disc the magnetic coupling is typically insufficient to couple the neutral particles to the field. On the contrary, near the surface, the coupling is generally adequate as the density is significantly lower and the ionisation fraction is higher. This accentuates the 'layered accretion' scenario, in which magnetic activity is supported only in the surface regions of the disc (Gammie 1996, Wardle 1997). Finally, it is worth noting that, in general, dust grains can affect the structure and dynamics of accretion discs via two additional mechanisms: Dust opacity can modify the radiative transport withing the disc –which, in turn, can dramatically alter its structure–, and dust particles may become dynamically important if their abundance is sufficiently high. In this study both effects are small because the disc is vertically isothermal and grains constitute only 1% of the mass of the gas (see below).

When dust grains are well mixed with the gas, they are expected to modify the magnetic activity of low conductivity discs through their impact on the conductivity. Therefore, a realistic study of the properties of the MRI in these discs must incorporate a consistent treatment of dust dynamics and evolution (unless they are assumed to have settled, a good approximatiion to model relatively late accretion stages, as in chapter 3). This analysis is further complicated because dust grains have complex spatial and size distributions (Mathis, Rumpl & Nordsieck 1977, Umebayashi & Nakano 1990), determined by the competing action of processes involving sticking, shattering, coagulation, growth (and/or sublimation) of ice mantles and settling to the midplane (e.g. Weidenschilling & Cuzzi 1993). Previous results (chapter 3) highlight the importance of incorporating in these studies a full conductivity tensor as well (Cowling 1957, Norman & Heyvaertz 1985, Nakano & Umebayashi 1986, Wardle & Ng 1999), as Hall diffusion largely determines the growth and structure of MRI perturbations, particularly at distances of the order of a few AU from the

central protostar.

We present in this chapter preliminary results on the vertical structure and linear growth of the MRI in a disc where dust grains are well mixed with the gas over the entire vertical dimension of the disc. For simplicity, we assume here that all particles have the same radius $a = 0.1\mu$m and constitute 1% of the total mass of the gas, a typical assumption adopted in studies of molecular clouds (Umebayashi & Nakano 1990). This fraction is constant with height, which means that we have assumed that no sedimentation has occurred. Although this is a very simplified picture, the results illustrate the importance of dust particles in the delicate ionisation equilibrium of discs, and consequently, on their magnetic activity.

This chapter is organised as follows: the adopted disc model is described in section 4.2, including a discussion of the typical dependency of the components of the conductivity tensor and magnetic coupling with height with, and without, grains. Section 4.3 then presents the structure and growth of MRI modes at a representative distance ($R = 10$ AU) from the central protostar, and compares solutions incorporating different configurations of the conductivity tensor. These results, and possible implications for the dynamics and evolution of low conductivity discs, are discussed in section 4.4.

4.2 Disc model

We adopt the minimum-mass solar nebula model (Hayashi 1981, Hayashi et al 1985) as our fiducial disc, and assume that it is geometrically thin and isothermal. Our formulation incorporates the disc vertical stratification, but neglects radial gradients. Under these assumptions, the equilibrium structure of the disc is the result of the balance between the vertical component of the gravitational force exerted by the central object and the pressure gradient of the fluid. The vertical profile of the gas density is then $\rho(r, z) = \rho_o(r)$ exp $(-0.5z^2/H^2)$, where ρ_o is the midplane density and H is the scaleheight of the gas. Finally, the neutral gas is assumed to be composed of molecular hydrogen and helium, such that $n_{He} = 0.2n_{H_2}$, which gives $n_H(r, z) = \rho(r, z)/1.4m_H$.

As discussed above, the magnetic coupling in protostellar discs is expected to be low, given that ionisation processes are generally ineffective (except possibly in the surface regions), while recombination is accelerated by the high fluid density

and the presence of dust grains. As a result, magnetic activity is likely to occur near the surface, but it is expected to be suppressed in the inner sections of the disc (Gammie 1996, Wardle 1997). In regions where $\chi \gtrsim 10$ ideal-MHD conditions hold and the particular configuration of the conductivity tensor has little effect on the behaviour of the MRI. When χ is weaker than this but $\gtrsim |\sigma_1|/\sigma_\perp$, ambipolar diffusion dominates (Wardle 1999, see chapter 3). Finally, in the vertical sections where $\chi < |\sigma_1|/\sigma_\perp$, Hall diffusion modifies the structure and growth of MRI unstable modes, provided that the magnetic coupling is sufficient for unstable modes to grow (see section 3.5.1).

Fig. 4.1 shows the components of the conductivity tensor ($\sigma_\parallel$, $|\sigma_1|$ and σ_2), magnetic coupling (χ) and ratio $|\sigma_1|/\sigma_\perp$ as a function of height for the chosen radial position ($R = 10$ AU) and $B = 10$ mG. Two cases are considered: Dust grains have either settled into a thin layer about the midplane (top panel), or they are fully mixed with the gas phase over the entire vertical extention of the disc (bottom panel). Note that the field-parallel ($\sigma_\parallel$) and Pedersen (σ_2) conductivities are always positive, as all charged species contribute positively to them. On the contrary, the contribution to the Hall term (σ_1) by a particular charged species, depends on the sign of the charge (Wardle & Ng 1999).

When no grains are present (top panel), $|\sigma_1|$ dominates over σ_2 for $z/H \lesssim 2.5$. In this region, $\sigma_2 \lesssim |\sigma_1| \ll \sigma_\parallel$ and the fluid is in the Hall conductivity regime. For higher z, $\sigma_\parallel \gg \sigma_2 \gg |\sigma_1|$ and ambipolar diffusion dominates. Note that the Hall conductivity term decreases more sharply than the Pedersen conductivity in response to the fall in fluid density. As a result, $|\sigma_1|$ is typically several orders of magnitude smaller than σ_2 in the surface regions. As $\chi > |\sigma_1|/\sigma_\perp$ for all z, Hall diffusion is not expected to play an important role in the local properties of the MRI for this magnetic field strength.

This picture is dramatically changed when dust grains are assumed to be well mixed with the gas (Fig. 4.1, bottom panel). The conductivities shown here were taken from Wardle (in prep.), who modelled the ionisation balance following Umebayashi & Nakano (1990); Nishi, Nakano & Umebayashi (1991) and Sano et al. (2000), but allowing for higher charge states that are likely to occur in discs. Note that in this case, all conductivity components drop drastically in relation to the previous results. For example, the Pedersen conductivity drops by about 5 orders of magnitude at the midplane.

We also note that the Hall conductivity component shows characteristic 'spikes', at the heights where it changes sign. In particular, σ_1 is positive when $0 \lesssim z/H \lesssim 1.6$ and $2.5 \lesssim z/H \lesssim 4.1$. It is negative at all other vertical locations. The change in sign of σ_1 corresponds to a change in the direction of the magnetic field at the height where particular species become decoupled to it by collisions with the neutrals. This, in turn, changes the contribution of different charged species to this component of the conductivity tensor. In order to explore the contributions to σ_1 in each of the vertical sections in which it has a different sign, we describe the behaviour of the charged species at four representative heights, namely $z/H = 1$ and 3 (for which $\sigma_1 > 0$), and $z/H = 2$ and 5 (where $\sigma_1 < 0$). This discussion is based in calculations by Wardle (in prep.).

At $z/H = 1$, the density is sufficiently high for electrons to stick to the grains. As a result, they reside mainly on dust particles, as do about a third of the ions. The contribution of (negatively charged) grains and ions to the Hall conductivity term are very similar, with a small positive excess, which determines the sign of σ_1 in this region. On the contrary, at $z/H = 2$, ions are the dominant positively charged species, while the negative charges are still contained in dust grains, which drift together with the neutrals. Consequently, σ_1 is negative in this section of the disc. At $z/H = 3$, ions and electrons are the main charge carriers and ions dominate the contribution to the Hall term, which makes σ_1 positive. Finally, for $z/H = 5$, the dominant contribution to the Hall conductivity term comes from the small percentage of remaining negatively charged grains. As a result, σ_1 is negative (and very small).

Finally, note that $\sigma_\parallel \gg \sigma_2 \gg |\sigma_1|$ for all z. This confirms that Ohmic diffusion is unimportant at this radius, as expected, given the relatively low fluid density (e.g. Wardle in prep.). Nonetheless, Hall diffusion is important within three scaleheights of the midplane ($\chi < |\sigma_1|/\sigma_\perp$) and would determine the properties of the MRI, provided that the coupling is sufficient to support unstable modes. At higher z, the ionisation fraction is such that $|\sigma_1|/\sigma_\perp \lesssim \chi \lesssim 10$ and ambipolar diffusion dominates.

4.3 Results

Fig. 4.2 compares the structure and growth of the fastest growing MRI modes at the radius of interest for different choices of the magnetic field strength. The left

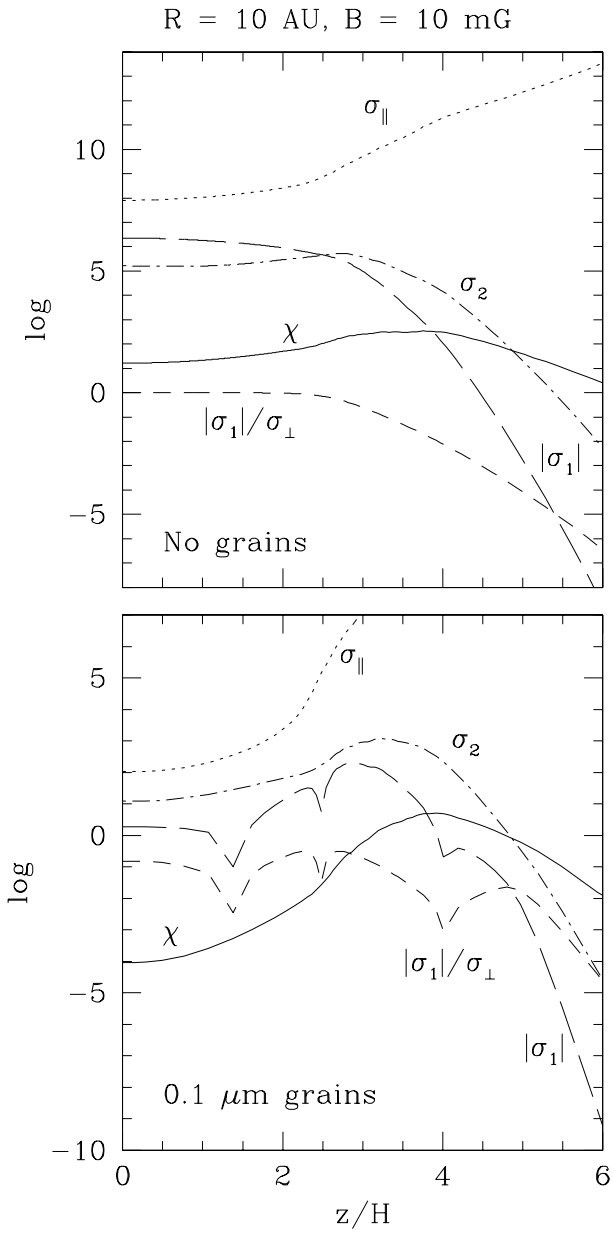

Figure 4.1 Components of the conductivity tensor ($\sigma_\parallel$, $|\sigma_1|$ and σ_2), magnetic coupling (χ) and $|\sigma_1|/\sigma_\perp$ as a function of height for $R = 10$ AU and $B = 10$ mG. Top panel corresponds to the case where dust grains are settled, so charges are carried by electrons and ions only. Bottom panel displays results assuming a population of 0.1μm grains is present. In the region where $\chi < |\sigma_1|/\sigma_\perp$, Hall diffusion determines the growth rate and structure of the MRI.

column displays solutions obtained assuming that grains have settled, while the right one shows results including the single size grain population described above. The properties of MRI perturbations at this radius, asuming that dust grains are settled, were discussed in detail in section 3.5. They are summarised again below for greater clarity.

Note that when ions and electrons are the sole charge carriers (left panel), Hall diffusion is important for $B \lesssim 1$ mG (see Fig. 3.6). This explains the high wavenumber, small central dead zone and fast growth of the perturbation for $B = 1$ mG. On the other hand, ambipolar diffusion is dominant close to the midplane for 1 mG $\lesssim B \lesssim 10$ mG. This component of the conductivity tensor typically drives the local growth rate (and amplitude) of MRI unstable modes to increase with height (see sections 3.5.1 and 3.5.2). As a result, the envelope of the perturbation for $B = 5$ mG peaks at an intermediate z. Finally, for stronger fields ($B \gtrsim 10$ mG), ideal-MHD holds at all heights, which causes the flat envelope, and growth at about the ideal-MHD rate, of the perturbation obtained with $B = 10$ mG. Unstable modes are found in this scenario for $B \lesssim 250$ mG (see Fig. 3.15, top panel). As the magnetic field is coupled to the gas even at the midplane, these perturbations are active at $z = 0$, with only the mode for $B = 1$ mG exhibiting a very small central dead zone.

The corresponding perturbations obtained under the assumption that dust grains are present are displayed in Fig. 4.2 (right panel). Note how the growth rate, wavenumber and range of magnetic field strengths for which unstable modes exist are all drastically diminished in relation to the previous case. The low magnetic coupling (see Fig. 4.1, bottom panel), especially within three scaleheights of the midplane, causes the amplitude of all perturbations in this section of the disc to be severely reduced. Unstable modes were found here only for $B \lesssim 10$ mG, a much reduced range compared with the few gauss for which unstable modes exist when ions and electrons are the only charge carriers.

Finally, Fig 4.3 compares results obtained using the full conductivity tensor (left column), and the ambipolar diffusion approximation (right column), as a function of the magnetic field strength for the radius of interest. For $B = 1$ mG, full σ perturbations grow faster and are active closer to the midplane, than modes obtained in the ambipolar diffusion limit. This is the result of the contribution of the Hall conductivity term, given that at 1 mG Hall diffusion is important and the magnetic coupling is sufficiently strong to support MRI unstable modes. Conversely, for $B = 5$

and 10 mG, the structure of perturbations in both limits is very similar. This is expected, as these perturbations peaks at a height ($z/H \sim 3$) where Hall diffusion is no longer locally dominant (see bottom panel of Fig. 4.1).

4.4 Discussion

In this chapter we have examined an illustrative example of the effect of dust grains in the magnetic activity of low conductivity discs. Solutions were computed for $R = 10$ AU, assuming a single size, 0.1μm grain population is well mixed with the gas phase at all z. The results indicate that the perturbations' wavenumber and growth rates are significantly reduced when grains are present. The central dead zone, which was practically nonexistent when grains were settled, extend now to $z/H \sim 3$. Unstable perturbations were found in this case for $B \lesssim 10$ mG. This maximum field strength corresponds well to the equipartition field at $z/H \approx 3.7$, the height at which the perturbation for this field strength peaks (see lower right panel of Fig. 4.2), as expected.

These results are preliminary and partial. They illustrate the impact of dust particles on the dynamics –and evolution– of low conductivity discs, using a single-size grain population. Solutions at 10 AU were computed more or less easily. However, even with this simplified formulation, the stiffness of the equations increases considerably for smaller radii. As a result, time constraints were eventually a limiting factor that prevented further investigation of this important topic closer to the protostar. This is material to be developed in future studies.

These results can be used, however, to estimate the maximum magnetic field strength to support magnetic activity at 1 AU. The magnetic coupling at this radius, in a disc including 0.1μm grains, is too weak below $z/H \sim 3.3$ to allow the field to sufficiently couple with the gas. (Wardle, in prep.). Assuming that the maximum field strength for the MRI to grow is also the equipartition field at about this height ($z/H \approx 3.5$), we can roughly estimate that the MRI should be active for $B \lesssim 400$ mG at 1 AU. This is a smaller range than the several gauss for which unstable modes exist when dust grains are not present. However, MRI modes still grow in this case for a wide range of field strengths.

The results just presented were obtained assuming that all grains have the same size and are well mixed with the gas at all z. More realistic spatial, and size, distri-

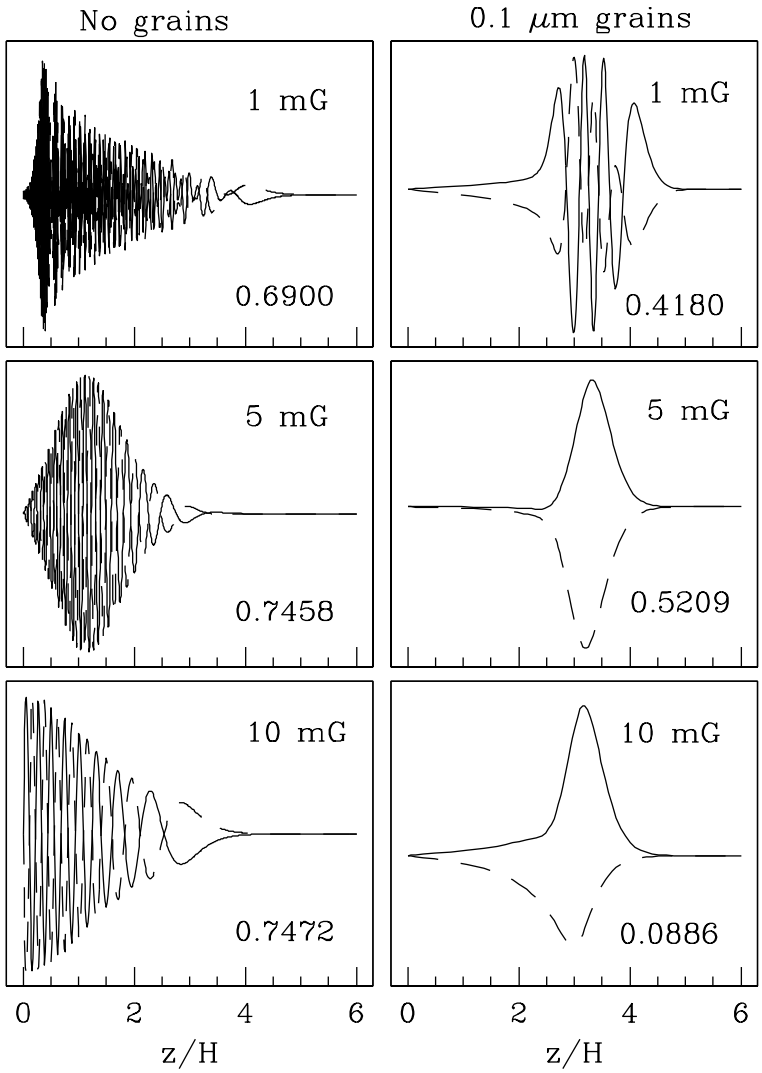

Figure 4.2 Structure and growth rate of the fastest growing MRI modes for $R = 10$ AU and different choices of the magnetic field strength. The left column shows the case where dust grains have settled, while the right one displays results assuming single size 0.1μm grains are well mixed with the gas. The growth rate is indicated in the lower right corner of each panel. The strength of the field appears in the top right corner. Note the reduced wavenumber and growth rate, as well as the extended dead zone of the perturbations obtained when dust grains are present.

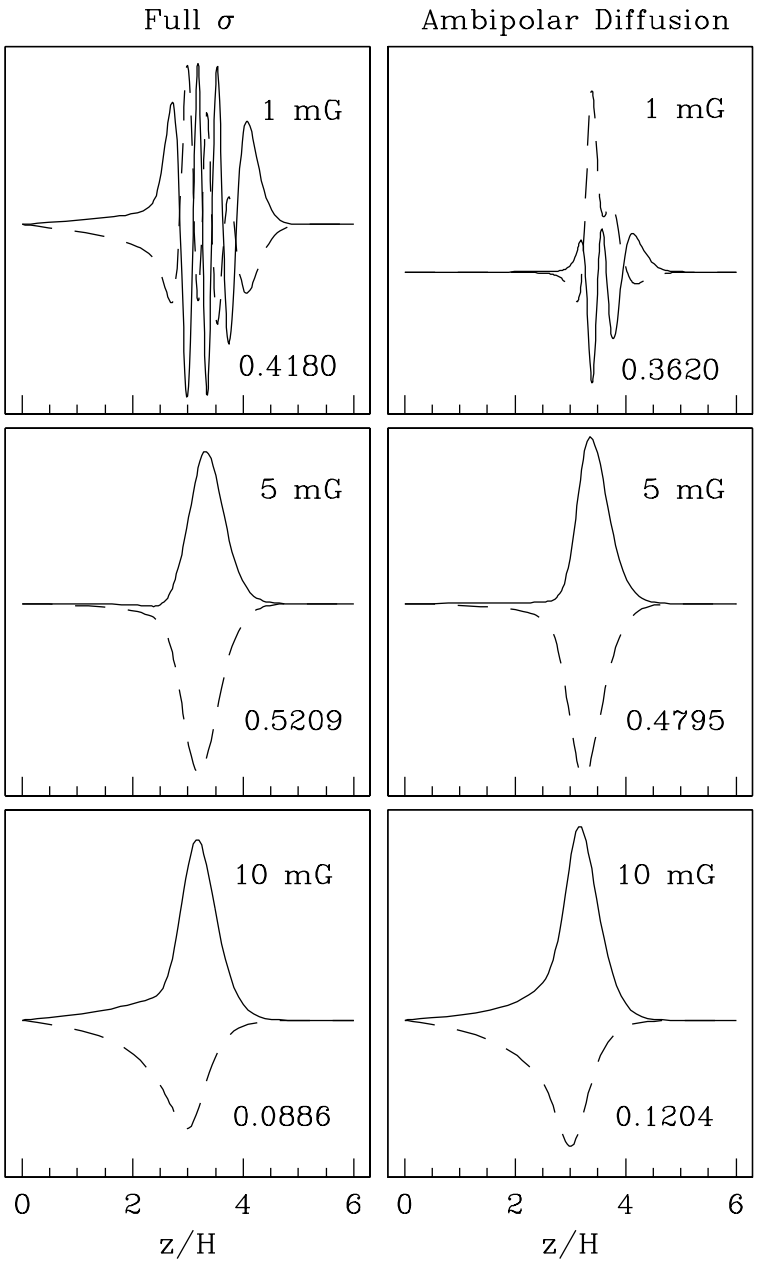

Figure 4.3 Structure and growth of the fastest growing MRI modes as a function of height for different configurations of the conductivity tensor: Full σ (left column) and the ambipolar diffusion approximation (right column).

butions must incorporate the effects of dust dynamics and evolution within the disc. Observations of the mid –and far– infrared spectra of discs have provided credible indications that dust properties in discs are indeed different from those of particles in diffuse clouds (e.g. Van Dishoeck 2004 and references therein). Two aspects of this dust evolution have been clearly identified. First, dust grains coagulate from 0.1μm to $\sim 1\mu$m particles. Second, (silicate) material becomes crystallised. It is believed that this crystallisation occurs in the disc, given that crystalline silicates are absent from the interstellar medium. Furthermore, the presence of this material at radial locations where the temperature is too low to produce them, suggests significant radial mixing takes place as well (e.g. Van Dishoeck 2004 and references therein). Similarly, simulations of dust dynamics and evolution also suggest that in quiescent environments, they tend to settle and agglomerate into bigger particles (e.g. Weidenschilling & Cuzzi 1993) and efficiently coagulate and grow icy mantles (Ossenkopf 1993). The effect of this settling in the spectral energy distribution (and optical appearance) of protostellar discs has been investigated in recent studies (Dullemond & Dominik 2004).

How quickly, and to what height, dust particles are able to settle is an important, and largely unanswered, question. According to Nakagawa, Nakazawa & Hayashi (1981), the mass fraction of ~ 1 - 10μm grains well mixed with the gas, diminishes from $\sim 10^{-1}$ to 10^{-4} in a timescale of about 2×10^3 to 10^5 years. Moreover, although the timescale for dust grains to sediment all the way to the midplane may exceed the lifetime of the disc, they may be able to settle within a few scaleheights from the midplane in a shorter timescale (Dullemond & Dominik 2004). This is complicated even more by the expectation that the transition between sections were dust grains are well mixed with the gas, and those completely depleted of them, occurs gradually (Dullemond & Dominik 2004). All these processes modify the surface area of dust grains and impact the recombination rate on their surfaces and the way they drift in response to magnetic stresses.

MHD turbulence may itself be an important factor for the settling of dust particles. It may, in particular, produce sufficient vertical stirring to prevent settling below a certain height (Dullemond & Dominik 2004 and references therein). However, this is contingent on the disc being able to generate and sustain MHD turbulence in the vertical sections where dust is present. This is not guaranteed, even if turbulence exists in other regions, as dust grains generally reduce the ionisation fraction of the

gas, as discussed above. As a result, the efficiency –and even viability– of MHD turbulence in the presence of dust grains, is an important topic that merits careful investigation.

Chapter 5

Conclusions

In this thesis we have examined the linear growth and vertical structure of the magnetorotational instability (MRI; Balbus & Hawley 1991, 1998; Hawley & Balbus 1991) in low conductivity discs. The MRI is the most promising candidate to generate and sustain angular momentum transport away from the central object, so disc material can be accreted. In addition, this is an important example of the magnetic activity of such discs. This work is relevant for the study of weakly ionised accretion discs, such as protostellar and quiescent dwarf novae systems (Gammie & Menou 1998, Menou 2000, Stone et al. 2000), where the low ionisation fraction causes the flux freezing approximation to break down.

Our method incorporates the effects of the magnetic coupling, the conductivity of the fluid and the strength of the magnetic field, which is initially vertical. Perturbations were restricted to have vertical wavevectors only, which are the most unstable modes for this field geometry when the fluid is in either the Hall or resistive conductivity regimes (Balbus & Hawley 1991, Sano & Miyama 1999). This is not necessarily the case in the ambipolar diffusion limit (Kunz & Balbus 2003), where the fastest growing modes can have radial wavevectors as well.

We treat the conductivity as a tensor, which is a function of location (r, z). This is the first study to explore the effect of Hall diffusion in a stratified disc. Using this formulation we examine the impact of different conductivity regimes dominating at different heights on the properties of the MRI. This is important, as Hall diffusion is relevant over a wide range of fluid conditions in low conductivity discs and is expected to modify the structure and growth of unstable modes, especially in regions where the magnetic coupling is low. When Hall diffusion dominates, local MRI

perturbations grow for levels of magnetic coupling below the minimum required for modes in the ambipolar diffusion limit to exist (Wardle 1999). The conclusions of this study are summarised as follows:

From the analysis of the structure and growth of the MRI in parameter space (chapter 2), we found that the envelopes of short-wavelength perturbations are determined by the action of competing local growth rates at different heights, driven by the vertical stratification of the disc. Ambipolar diffusion perturbations peak consistently higher above the midplane than modes including Hall conductivity. When the magnetic coupling is weak ($\chi < v_A/c_s$), perturbations calculated with the full conductivity tensor grow significantly faster, and are active over a more extended cross section of the disc, than those obtained adopting the ambipolar diffusion approximation. Similarly, when the magnetic coupling is reduced, the maximum growth rate decreases from the ideal rate ($\sim 0.75\Omega$) in a way that depends on the conductivity regime of the fluid. In particular, perturbations in the Hall limit grow at about the ideal rate when the midplane magnetic coupling (χ_o) exceeds v_A^2/c_s^2. In the ambipolar diffusion regime, the corresponding limit is $\chi_o > v_A/c_s$. These results are in agreement with findings of a local analysis (W99). We also derived an approximate criterion ($\chi \lesssim |\sigma_1|/\sigma_\perp$ for when Hall diffusion dominates the structure and growth of the MRI. This is satisfied over a broad range of conditions in low conductivity discs.

We then explored the linear phase of the MRI using a realistic ionisation model, under the assumption that dust grains have settled towards the midplane (chapter 3). Solutions were presented at representative radial locations ($R = 1$, 5 and 10 AU) as a function of the magnetic field strength for different disc models, configurations of the conductivity tensor and sources of ionisation. For the minimum mass solar nebula model, when cosmic rays are assumed to penetrate the disc, unstable modes exist at 1 AU for $B \lesssim 8$ G. When 200 mG $\lesssim B \lesssim 5$ G, the growth rate is of order the ideal-MHD rate (0.75Ω). When cosmic rays are excluded from the disc, unstable modes still grow for $B \lesssim 2$ G. Hall diffusion dominates the structure and growth of the instability at this radius for all magnetic field strengths for which unstable modes exist. Solutions obtained with a full conductivity tensor grow faster, and act over a wider vertical cross-section of the disc, than perturbations in the ambipolar diffusion limit. Finally, when the magnetic field is strong, ambipolar diffusion shapes the perturbations' envelopes, which peak at an intermediate height, instead of having

the fairly flat envelope modes in the Hall limit have in this region of parameter space. We conclude that, despite the low magnetic coupling, the magnetic field is dynamically important for a broad range of conditions in low conductivity discs. At radii of order 1 AU, it is crucial to incorporate Hall conductivity in studies of the magnetic activity of these discs, and in particular, in the analysis of the MRI.

In chapter 4 we explored the impact of dust grains on the solutions just discussed. They affect the dynamics of discs if they are well mixed with the gas. This is generally the case in early stages of accretion, and/or when turbulence prevents them from settling towards the midplane. Dust particles can become an important charged species, but their drift is impaired by collisions with the neutrals. They also open up additional mechanisms for more mobile charged particles to recombine. As a result, grains are expected to lower the ionisation fraction, and the conductivity, of the gas.

For simplicity, we assumed that all particles have the same radius (0.1μm) and constitute 1 % of the total mass of the gas (Umebayashi & Nakano 1990). We presented solutions for $R = 10$ AU and compared them with the results obtained when grains were absent. The growth rate, wavenumber and range of magnetic field strengths for which unstable modes exist drop sharply, as expected. Similarly, the central magnetic dead zone, which was practically nonexistent in the previous case, extends from the midplane up to $z/H \approx 3$. We find that Hall diffusion modifies the structure and growth of the MRI when $B \approx 1$ mG. However, for stronger fields ($B \gtrsim 5$ mG), perturbations in the ambipolar diffusion limit are similar to the properties of full conductivity modes as well. This is to be expected, as these perturbations peak at a vertical location where Hall diffusion is no longer locally dominant. Perturbations grow for $B \lesssim 10$ mG, a much reduced maximum strength from the ~ 250 mG for which the disc was active when grains were assumed to have settled. This maximum field strength (10 mG), is the equipartition field at the height for which perturbations peak, as expected.

Time constraints prevented further investigation, given the long runtime associated with finding modes for $R \lesssim 5$ AU. This is left for future work. However, the results at 10 AU can be used to estimate the activity of the disc at 1 AU. At this radius, the magnetic field is also not sufficiently coupled to the gas for $z/H \lesssim 3$ (Wardle, in prep.). Therefore, MRI unstable modes are expected to peak at a higher z. Assuming that the maximum field strength to support unstable MRI modes is

the equipartition field at that height (as was the case at 10 AU), we can roughly estimate the maximum field strength for which unstable modes are expected to grow at this radius. Using $z/H = 3.5$, we find that the magnetic field should be dynamically important for strengths up to ~ 400 mG.

These solutions were obtained assuming a single-size grain population was present. In general, however, grains have a complex size distribution (e.g. Mathis, Rumpl & Nordsieck 1977; Umebayashi & Nakano 1990). Also, although in quiescent environments they settle towards the midplane and become dynamically uncoupled to the gas at higher z, MHD turbulence may prevent them from sedimenting below a certain height (Dullemond & Dominik 2004). On the other hand, grains may diminish the efficiency of MHD turbulence itself, by reducing the gas magnetic coupling.

The equilibrium structure of low conductivity discs, and their magnetic activity, are the result of a complex interplay between many physical processes. We have explored here, in the context of an analysis of the linear phase of the MRI, the impact of some of these processes in the dynamics of discs: the magnetic field strength, level of magnetic coupling, magnetic diffusion, disc model, ionising sources and presence of dust grains. Other processes, notably the mechanism leading to the saturation of the MRI, can only be studied using a non-linear formulation. This is an important process, given that the saturated level of the Maxwell stress ($B_r B_\phi / 4\pi$) largely determines how much angular momentum is transported radially outwards by the MRI. The properties of the MRI in the saturated state seem, in turn, to be dependent on the characteristic length-scale of the instability in the linear phase (Sano, Inutsuka & Miyama 1998, Sano & Inutsuka 2001, Sano & Stone 2002b). This is so because the fastest growing mode in the linear regime is also an exact solution to the full non-linear equations in the incompressible limit (Goodman & Xu 1994). Numerical studies of the saturation of the MRI (Hawley & Balbus 1992; Matsumoto & Tajima 1995; Stone et. al. 1996; Sano, Inutsuka & Miyama 1998; Sano & Miyama (1999); Fleming, Stone & Hawley 2000; Sano & Inutsuka 2001; Sano & Stone 2002a, 2002b; Sano et. al. 2004) have not yet modelled the case when different conductivity regimes are dominant at different heights. The results of this study suggest that such a formulation is crucial for the realistic modelling of the saturated state of the MRI. In particular, we have seen that Hall diffusion tends to increase the wavenumber of unstable modes in relation to that of perturbations in the ambipolar diffusion limit for the same field strength. This suggests that non-linear models incorporating a

height-dependent conductivity, as well as Hall diffusion, are necessary to study the mechanism leading to the saturation of the MRI and, ultimately, the efficiency of MRI-driven angular momentum transport in low conductivity discs.

More generally, all these processes are also likely to affect other aspects of the activity of discs, such as planet formation and migration, launching of jets and dynamo action. Hopefully this study will draw attention to the importance of Hall diffusion and, more generally, to the link between the micro – and macro – physics in low conductivity accretion discs.

References

[1] Adams F. C., Lin D. N. C., 1993, in Protostars and Planets III, ed. E. H. Levy, J. I. Lunine (Tucson: U. Arizona Press), p. 721

[2] Adams F. C., Emerson J. P., Fuller G. A. 1990, ApJ, 357, 606

[3] Balbus S. A., 2003, Annu. Rev. Astron. Astrophys, 41, 555

[4] Balbus S. A., Hawley J. F., 1991, ApJ, 376, 214

[5] Balbus S. A., Hawley J. F., 1992a, ApJ, 392, 662

[6] Balbus S. A., Hawley J. F., 1992b, ApJ, 400, 610

[7] Balbus S. A., Hawley J. F., 1998, Rev. Mod. Phys., 70, 1

[8] Balbus S. A., Papaloizou J. C. B., 1999, ApJ, 521, 650

[9] Balbus S. A., Terquem C., 2001, ApJ, 552, 235

[10] Beckwith S. V. W., Sargent A. I., Chini R. S., Güsten R., 1990, AJ, 99, 924

[11] Blaes O. M., Balbus S. A., 1994, ApJ, 421, 163

[12] Blandford R. D., Payne D. G., 1982, MNRAS, 199, 883

[13] Brandenburg A., Nordlund A., Stein R. F., Torkelsson U., 1995, ApJ, 446, 741

[14] Cabot W., 1996, ApJ, 465, 874

[15] Cabot W., Pollack J., 1992, Geophys. Astrophys. Fluid Dyn., 64, 97

[16] Cabrit S., André P., 1991, ApJ, 379, L25

[17] Cabrit S., Edwards S., Strom S. E., Strom K. M., 1990, ApJ, 354, 687

[18] Chandrasekhar S., 1961, Hydrodynamic and Hydromagnetic Stability (New York, Dover)

[19] Christodoulou D. M., Contopoulos J., Kazanas D., 1996, ApJ, 462, 865

[20] Consolmagno G. J., Jokipii J. R., 1978, Moon Planets, 19, 253

[21] Contopoulos I., Saunty C., 2001, A& A, 365, 165

[22] Cowling, T. G. 1957, Magnetohydrodynamics (New York: Interscience)

[23] Desch S. J., 2004, ApJ, 608, 509

[24] Draine, B. T., Roberge, W. G., Dalgarno, A. 1983, ApJ, 264, 485

[25] Dullemond C. P., Dominik C., 2004, preprint(astro-ph/0405226 v1)

[26] Fleming T. P., Stone J. M., Hawley, J. F., 2000, ApJ, 530, 464

[27] Frank J., King A., Raine D., 2002, Accretion processes in astrophysics (Cambridge: Cambridge University Press)

[28] Fromang S., Terquem C., Balbus S. A., 2002, MNRAS, 329, 18

[29] Gammie, C. F., Balbus, S. A. 1994, MNRAS, 270, 138

[30] Gammie C. F., 1996, ApJ, 457, 355

[31] Gammie C. F., Menou K., 1998, ApJ, 492, L75

[32] Glassgold A. E., Feigelson E. D., Montmerle T., in Protostars & Planets IV, ed. V. G. Mannings, A. P. Boss, S. Russell (Tucson: Univ. Arizona Press), p. 429

[33] Glassgold A. E., Najita J., Igea J., 1997, ApJ, 480, 344

[34] Goodman J., Xu G., 1994, ApJ, 432,213

[35] Hartigan P., Edwards S. Ghandour L., 1995, ApJ, 452, 736

[36] Hawley J. F., Balbus S. A., 1991, ApJ, 376, 223

[37] Hawley J. F., Balbus S. A., 1995, Publ. Astron. Soc. Aust, 12, 159

[38] Hawley J. F., Gammie C. F., Balbus S. A., 1995, ApJ, 440, 742

[39] Hawley J. F., Gammie C. F., Balbus S. A., 1995, ApJ, 464, 690

[40] Hawley J. F., Stone J. M., 1998, ApJ, 501, 758

[41] Hayashi C., 1981, Prog Theor Phys Supp, 70, 35

[42] Hayashi C., Nakasawa K., Nakagawa Y., 1985, in Protostars & Planets II, ed. D.C. Black, M. S. Mathews (Tucson: Univ. Arizona Press), p. 1100

[43] Igea J., Glassgold A. E., 1999, ApJ, 518, 848

[44] Jin L., 1996, ApJ, 457, 798

[45] Kitamura Y., Momose M., Yokogawa S., Kawabe R., Tamura M., 2002, ApJ, 581, 357

[46] Königl A., 1989, ApJ, 342, 208

[47] Königl A., Pudritz R. E., 2000, in Protostars & Planets IV, ed. V. G. Mannings, A. P. Boss, S. Russell (Tucson: Univ. Arizona Press), p. 759

[48] Königl A., Ruden S. P., 1993, in Protostars & Planets III, ed. E. H. Levy, J. I. Lunine (Tucson: Univ. Arizona Press), p. 641

[49] Kunz M., Balbus S. A., 2004, MNRAS, 348, 355

[50] Levy E. H., Sonnet C. P., 1978, in Protostars & Planets, ed. T. Gehrels (Tucson: Univ. Arizona Press), p. 516

[51] Li Z. -Y., 1996, ApJ, 465, 855

[52] Lin D. N. C., Papaloizou J. C., 1980, MNRAS, 191, 37

[53] Lin D. N. C., Papaloizou J. C. B., Kley NAME. 1993, ApJ, 416, 689

[54] Looney L. W., Mundy L. G., Welch W. J., 2003, ApJ, 592, 255

[55] Lovelace R. V., Wang J. C., Sulkanen M. E., 1987, ApJ, 315, 504

[56] Lynden-Bell D., 1969, Nature, 223, 690

[57] MacLow M. M., Norman M. L., Königl A., Wardle M., 1995, ApJ, 442, 726

[58] Mathis J. S., Rumpl W., Nordsieck K. H., 1977, ApJ, 217, 425

[59] Matsumoto R., Tajima T., 1995, ApJ, 445, 767

[60] McCaughrean M. J., Stapelfeldt K. R., Close L. M., 2000, in Protostars & Planets IV, ed. V. G. Mannings, A. P. Boss, S. Russell (Tucson: Univ. Arizona Press), p. 485

[61] Menou K., 2000, Science, 288, 2022

[62] Mestel L., Spitzer L., 1956, MNRAS, 116, 503

[63] Moffatt K., 1978, Magnetic Field Generation in Electrically Conducting Fluids (Cambridge: Cambridge University Press).

[64] Morton D. C., 1974, Astrophys. J., 193, L35

[65] Nakagawa Y., Nakazawa K., Hayashi C., 1981, Icarus, 45, 517

[66] Nakano, T., Umebayashi, T. 1986, MNRAS, 218, 663

[67] Natta A., Grinin V., Mannings V., 2000, in Protostars & Planets IV, ed. V. G. Mannings, A. P. Boss, S. Russell (Tucson: Univ. Arizona Press), p. 559

[68] Nishi R., Nakano T., Umebayashi T., 1991, ApJ, 368, 181

[69] Norman, C., Heyvaerts, J. 1985, AA, 147, 247

[70] Oppenheimer M., Dalgarno A., 1974, ApJ, 192, 29

[71] Ossenkopf V., 1993, AA, 280, 617

[72] Papaloizou J. C. B.,, Terquem C., 1997, MNRAS, 287, 771

[73] Pilipp, W., Hartquist, T. W., Havnes, O., Morfill, G. E. 1987, ApJ, 314, 341

[74] Pringle J. E., 1981, Accretion Discs in Astrophysics, ARA&A, 19, 137

[75] Pudritz R. E., Norman C. A., 1983, ApJ, 274, 677

[76] Rozyczka M., Spruit H., 1993, ApJ, 417, 677

[77] Ryu D., Goodman J., 1992, ApJ, 338, 438

[78] Salmeron R., Wardle M., 2003, MNRAS, 345, 992 (SW03)

[79] Sano T., Inutsuka S. I., 2001, ApJ, 561, L179

[80] Sano T., Miyama S., 1999, ApJ, 515, 776

[81] Sano T., Stone J. M., 2002a, ApJ, 570, 314

[82] Sano T., Stone J. M., 2002b, ApJ, 577, 534

[83] Sano T., Stone J. M., 2003, ApJ, 586, 1297

[84] Sano T., Inutsuka S. I., Miyama S. M., 1998, ApJ, 506, L57

[85] Sano T., Inutsuka S. I., Turner N. J., Stone J. M., 2004, ApJ, 605, 321

[86] Sano T., Miyama S., Umebayashi J., Nakano T., 2000, ApJ, 543, 486

[87] Semenov D., Wiebe D., Henning Th., 2004, A&A, 417, 93

[88] Shakura N. I., Sunyaev R. A., 1973, A& A, 24, 337

[89] Shu F., Najita J., Galli D., Ostriker E., Lizano S., 1993, in Protostars & Planets III, ed. E. H. Levy, J. I. Lunine (Tucson: Univ. Arizona Press), p. 3

[90] Shull J. M., Van Steenberg M. E., 1985, ApJ, 298, 268

[91] Spitzer, L. 1978, Physical Processes in the Interstellar Medium (New York: Wiley)

[92] Stepinski T., 1995, RevMexAA, 1, 267

[93] Stone J. M., Balbus S. A., 1996, ApJ, 464, 364

[94] Stone J., Fleming T., 2003, ApJ, 585, 908

[95] Stone J. M., Hawley J. F., Gammie C. F., Balbus S. A., 1996, ApJ, 463, 656

[96] Stone J. M., Gammie C. F. Balbus S. A., Hawley J. F., 2000, in Protostars & Planets IV, ed. V. G. Mannings, A. P. Boss, S. Russell (Tucson: Univ. Arizona Press), p. 589

[97] Toomre A., 1964, ApJ, 139, 1217

[98] Tout C. A., Pringle J. E., 1992, MNRAS, 259, 604

[99] Tout C. A., Pringle J. E., 1996, MNRAS, 281, 219

[100] Umebayashi T., Nakano T., 1980, PASJ, 32, 405

[101] Umebayashi T., Nakano T., 1981, PASJ, 33, 617

[102] Umebayashi T., Nakano T., 1990, MNRAS, 243, 103

[103] Velikhov E. P., 1959, JETP, 36, 1398

[104] Vishniac E. T., Diamond P., 1989, ApJ, 347, 447

[105] Voit M., 1991, ApJ, 377, 158

[106] Wardle, M., Königl, A. 1993, ApJ, 410, 218

[107] Wardle M., 1997, in Proc. IAU Colloq. 163, Accretion Phenomena and Related Outflows, ed. D. Wickramasinghe, L. Ferrario, G. Bicknell (San Francisco: ASP), p. 561

[108] Wardle M., 1998, MNRAS, 298, 507

[109] Wardle M., 1999, MNRAS, 307, 849 (W99)

[110] Wardle M., 2003, preprint (astro-ph/0307086)

[111] Wardle M., Ng C., 1999, MNRAS, 303, 239

[112] Wardle M., in preparation

[113] Weidenschilling S. J., Cuzzi J. N., 1993, in Protostars & Planets III, ed. E. H. Levy, J. I. Lunine (Tucson: Univ. Arizona Press), p. 1031

[114] Weintraub D. A., Sandell G., Duncan W. D., 1989, ApJ, 340, L69

[115] Wilner D. J., Lay O. P., 2000, in Protostars & Planets IV, ed. V. G. Mannings, A. P. Boss, S. Russell (Tucson: Univ. Arizona Press), p. 509